ABSTRACT

Title of Dissertation: *IN SITU* CHARACTERIZATION OF OPTICAL ABSORPTION BY CARBONACEOUS AEROSOLS: CALIBRATION AND MEASUREMENT

Rian You, Doctor of Philosophy, 2016

Dissertation directed by: Michael R. Zachariah, Professor
Chemical Physics Program
Department of Chemical Engineering and Chemistry

Light absorption by aerosols has a great impact on climate change. A Photoacoustic spectrometer (PA) coupled with aerosol-based classification techniques represents an in situ method that can quantify the light absorption by aerosols in a real time, yet significant differences have been reported using this method versus filter based methods or the so-called difference method based upon light extinction and light scattering measurements. This dissertation focuses on developing calibration techniques for instruments used in measuring the light absorption cross section, including both particle diameter measurements by the differential mobility analyzer (DMA) and light absorption measurements by PA. Appropriate reference materials were explored for the calibration/validation of both measurements. The light absorption of carbonaceous aerosols was also investigated to provide fundamental understanding to the absorption mechanism.

The first topic of interest in this dissertation is the development of calibration nanoparticles. In this study, bionanoparticles were confirmed to be a promising reference material for particle diameter as well as ion-mobility. Experimentally, bionanoparticles demonstrated outstanding homogeneity in mobility compared to currently used calibration particles. A numerical method was developed to calculate the true distribution and to explain the broadening of measured distribution. The high stability of bionanoparticles was also confirmed. For PA measurement, three aerosol with spherical or near spherical shapes were investigated as possible candidates for a reference standard: C_{60}, copper and silver. Comparisons were made between experimental photoacoustic absorption data with Mie theory calculations. This resulted in the identification of C_{60} particles with a mobility diameter of 150 nm to 400 nm as an absorbing standard at wavelengths of 405 nm and 660 nm. Copper particles with a mobility diameter of 80 nm to 300 nm are also shown to be a promising reference candidate at wavelength of 405 nm.

The second topic of this dissertation focuses on the investigation of light absorption by carbonaceous particles using PA. Optical absorption spectra of size and mass selected laboratory generated aerosols consisting of black carbon (BC), BC with non-absorbing coating (ammonium sulfate and sodium chloride) and BC with a weakly absorbing coating (brown carbon derived from humic acid) were measured across the visible to near-IR (500 nm to 840 nm). The manner in which BC mixed with each coating material was investigated. The absorption enhancement of BC was determined to be wavelength dependent. Optical absorption spectra were also taken

for size and mass selected smoldering smoke produced from six types of commonly seen wood in a laboratory scale apparatus.

IN SITU CHARATERIZATION OF OPTICAL ABSORPTION BY ATMOSPHERICALLY RELEVANT AEROSOLS

by

Rian You

Dissertation submitted to the Faculty of the Graduate School of the
University of Maryland, College Park, in partial fulfillment
of the requirements for the degree of
Doctor of Philosophy
2016

Advisory Committee:
Professor Michael R. Zachariah, Chair
Professor John Ondov
Dr. George Mulholland
Professor Sheryl Ehrman
Professor Russell Dickerson

Dedication

I dedicate this work to the most important people in my life: Jinglei Ping, my dearest husband and to my daughter Buqing Ping. Thank you for you unconditionally love and support through all these years. I wouldn't be so happy and go this far without you standing by my side. I love you.

And to my father Jinao You and mother Shuxin Yan. Your support and love made me the person I am. Thank you!

Acknowledgements

I would like to thank many people for their help in making my work here possible and my life here enjoyable.

First and foremost, I would like to thank my advisor, Professor Michael Zachariah, for his consistence support and guidance throughout the years of my graduate study. Dr. Zachariah has patiently led me to the wonderland of aerosol research. I benefit a lot from his careful guidance, meticulous instructions and invaluable encouragements. His advice in both research and life has been one of my most valuable assets throughout my life. In Dr. Zachariah's group I enjoy research and life, and I feel very lucky to be a member of it.

I would also like to thank three people in particular. Dr. George Mulholland has consistently instructed me from theoretical perspective and dedicated to make this dissertation to be a quality work. His attitudes towards research and academic are treasures I cherish most. Dr. Christopher Zangmeister and Dr. James Radney in NIST developed the Photoacoustic system, which is the most critical element in my work on characterizing light absorption by aerosols, and I would not be able to accomplish the project without their support. Not only were they my mentors, but also they are my friends. I greatly enjoyed the days we spent in the lab, which will be the most valuable memory in my life.

I would like to express my gratitude to Professor John Ondov, Professor Sheryl Ehrman and Professor Russell Dickerson for serving on my advisory committee, taking time editing my thesis and attending my defense. I also own my gratitude to Prof. Michael Copland and Mrs. Debbie Jenkins who have been giving

me selfless help during my graduate life. Special thanks also go to my colleague Dr. Mingdong Li, who showed me how to operate Electraspray and DMA during my first year of graduate research and collaborated with me for some projects in this group.

I owned the deepest thanks to my family: my parents, who provided extensive educational opportunities, taught me invaluable lessons and even when I am at the other side of the world, their love and support is always with me; my husband Jinglei, with whom I share happiness, excitement, and every experience I have in our everyday adventures; and my darling daughter Buqing, from whom I received unlimited joy.

Table of Contents

List of Tables

List of Figures

Chapter 1: Introduction

Aerosols, referring to solid or liquid particles suspended in a gaseous medium, are ubiquitous in the atmosphere, with particle diameters in the range of (10^{-9} ~ 10^{-4}) m.[1,2] Light absorption by atmospheric aerosols has a great impact on climate change in terms of direct and semi-direct radiative effect[3-5]. While net radiative forcing caused by aerosols is negative (i.e. cooling) due to aerosol scattering, strongly light absorptive aerosols, e.g. black carbon (BC), contribute positive forcing (i.e. heating) by transforming electromagnetic into thermal energy that heats the absorbing particles and their surroundings. The local atmospheric temperature is changed due to the heating of light absorbing aerosols, which influences relative humidity, atmospheric circulation and stability, and thereby cloud formation and lifetime (semi-direct effect).[6,7] In addition, light absorption by aerosols, distinct from other forcing mechanisms like light scattering, may continue to contribute strongly to radiative forcing after deposition on snow and ice by lowering snow and ice albedo and changing snow cover duration and spring runoff timing[8-10]. Thus quantification of light absorption by atmospheric aerosols is among the central topics in the current environment research.

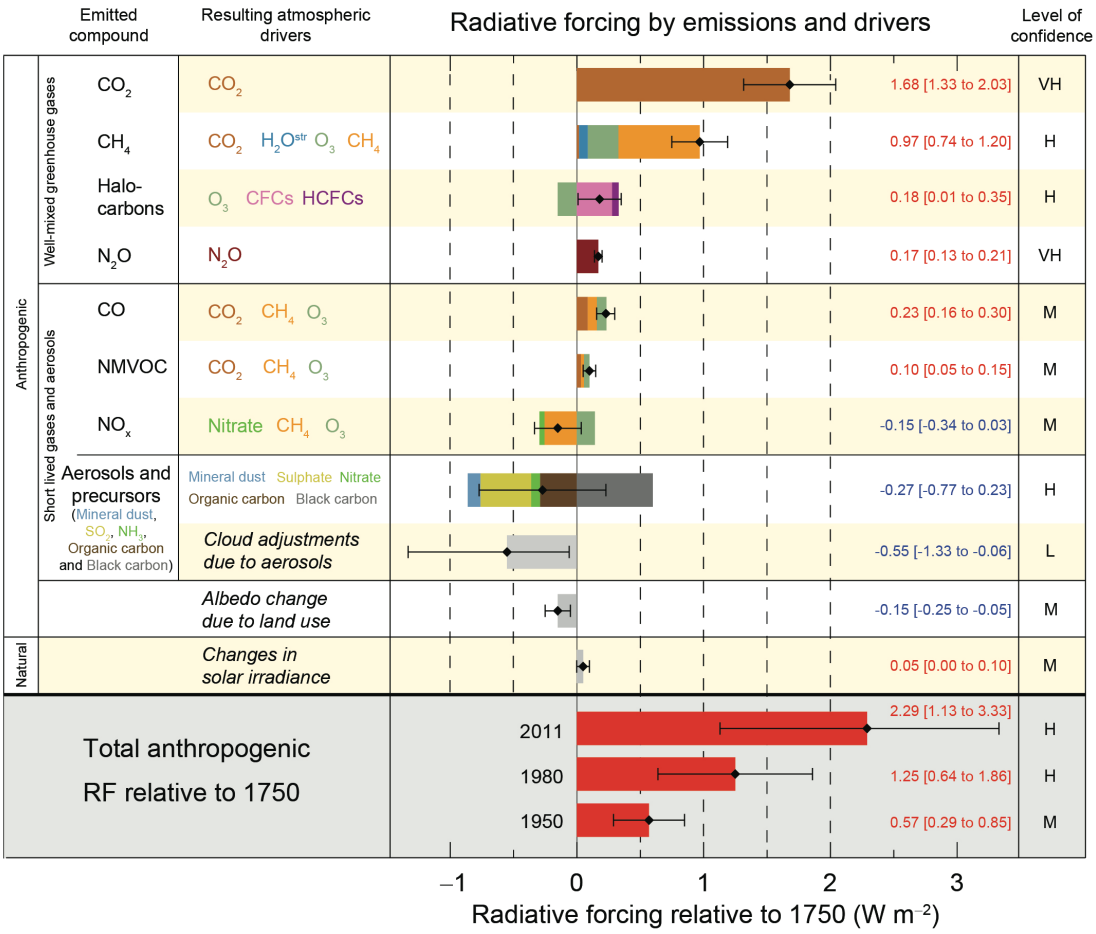

Figure 1.1 *Global-average radiative forcing (RF) estimates relative to 1750 and aggregated uncertainties for anthropogenic aerosols, carbon dioxide (CO_2), methane (CH_4), nitrous oxide (N_2O) and other important agents and mechanisms, together with the typical geographical extent (spatial scale) of the forcing and the assessed level of scientific understanding (LOSU). Overall contribution of aerosols is cooling while strongly absorptive aerosols, e.g. black carbon, contribute to positive forcing.*[11]

At present the most common method to measure light absorption by aerosols is indirect, filter-based methods including the Aethalometer[12], Particle Soot Absorption Photometer (PSAP)[13], Multi-Angle Absorption Photometer[14] and the continuous soot monitoring system[15]. The basic principle of these techniques is to

deposit aerosols on a filter by pulling air sample through it at a known flow rate. The attenuation of light across the filter with accumulated aerosols (i.e. transmittance) is then interpreted as a measure of aerosols light absorption. Despite the widespread application in field measurements, these filter-based techniques are performed on aerosols deposited on filters instead of on airborne particles in their natural state, thereby suffer from various artifacts that need to be addressed carefully. The necessary corrections of measured transmittance change to light absorption [16]include 1) the filter loading correction that compensate the non-linear response of attenuation to the increase of aerosols loading (i.e. the shadowing effect) 2) absorption enhancement correction that accounts for the enhancement of the particle absorption due to multiple scattering by the filter substrate and by the non-absorbing particles loaded on the filter. These corrections are found to be source specific[17,18] and difficult to be carried out in the field. Thereby general corrections calculated during inter-comparisons are usually applied to all PSAP or Aethalometer units, resulting in a precision somewhere in the range of 20-25 % [13,19] and 30-35 %[17,18] respectively.

Light absorption can also be determined from the so-call difference measurement, where absorption is derived from the difference between extinction and scattering. The combination of instrumentation that provides the best measure of absorption by difference is through cavity ring down spectrometer to measure extinction by aerosols (with accuracies of 2 % or better[20,21]) and an integrating Nephelometer to measure scattering, which has a reported accuracy of ~7 %[13]. Since absorption is determined from the difference of two quantities, large uncertainties are derived from the propagation of errors through the difference of the two quantities,

particularly at low absorption levels in the atmosphere. Hence this method is limited to strong absorptive aersols, high pollution events, or to laboratory studies on high concentrated aerosols.[13]

Photoacoustic spectroscopy (PA) represents an *in situ* optical technique that can characterize light absorption by airborne aerosols in a real time. It has quickly been accepted as a standard for comparisons to the filter based methods and the difference methods[18,22-25] with a reported accuracy of 5-10 %. Combination of PA with aerosol-based classification methods, including differential mobility analyzer (DMA) and aerosol particle mass analyzer (APM) that classify mobility diameter and mass of aerosols respectively, enables understanding of aerosol light absorption on the basis of other important physical properties of aerosols (i.e. particle size and mass). Based upon characterization of absorption using the combination of these instruments, this dissertation focuses on developing calibration techniques for DMA and PA by exploring appropriate reference materials for the calibration/validation of both measurements. While this combination of methods is being used, there is a lack of quantitative information on the methods. My research is directed as developing calibration methods for quantifying the performance of the instruments being used. Laboratory studies of light absorption by carbonaceous particles were also performed to provide fundamental understanding to the absorption mechanism.

In the following sections of this chapter I will first review the theoretical basis of aerosol light absorption, starting with introduction of basic concepts in particle optics, followed by a discussion of theoretical methods to calculate light absorption by aerosols, including Mie theory and T matrix methods. An overview of

instrumentations, i.e. DMA and PA, of which calibration methods were explored, is subsequently provided in detail. Other instruments involved in the characterization of light absorption by aerosols, i.e. APM and condensation particle counter (CPC) are briefly reviewed. Finally the scope of this dissertation is demonstrated.

1.1 Theory of Light Absorption by Particles

1.1.1 Basic Concepts

Aerosols remove light from incident beam (extinction) by light scattering, where the light is redirected from the original propagation direction, and by light absorption, where light is converted to thermal energy that heats the absorbing particles and their surroundings, as shown in Fig. 1.2.

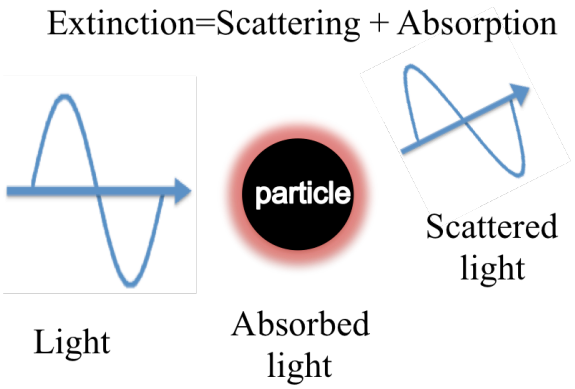

Figure 1.2 *Schematic of light interaction with a particle.*

Light absorption by an individual particle is often described by the absorption cross-section C_{Abs} (unit: m^2), linked to the geometry cross section A through an absorption efficiency Q_{Abs} via

$$Q_{Abs} = C_{Abs}/A, \tag{1.1}$$

where A is πr^2 *for* a spherical particle with radius of r.

Light absorption by an ensemble of n suspended particles in a volume V is described by absorption coefficient σ_{Abs} (unit: m^{-1}), which represents the fractional loss in light intensity due to absorption per unit propagation volume. Assuming particles are identical in the ensemble, σ_{Abs} can be simplified as the product of C_{Abs} and number density N.

$$\sigma_{Abs} = \frac{\sum_{i=1}^{n} C_{Abs,i}}{V} = NC_{Abs} \tag{1.2}$$

with $N=n/V$.

Absorption of aerosol per unit mass is described using the term "mass specific absorption cross section" (MAC), defined as

$$MAC = \frac{C_{Abs}}{m_p}, \tag{1.3}$$

where m_p is the mass of individual particle.

Mass specific scattering cross section (MSC) can be defined in a similar way as follows

$$MSC = \frac{C_{Sca}}{m_p}. \tag{1.4}$$

Thereby the single scattering albedo ϖ_0, an important input of global climate models, is defined as the fraction of light scattering over the extinction, as in

$$\varpi_0 = \frac{MSC}{MSC+MAC}. \tag{1.5}$$

The wavelength dependence of C_{Abs} can be described as the absorption Ångström exponent (AAE) and calculated as

$$AAE = -\log\left(\frac{C_{Abs,\lambda_1}}{C_{Abs,\lambda_2}}\right)/\log\left(\frac{\lambda_1}{\lambda_2}\right), \tag{1.6}$$

where λ is wavelength, for pair-wise wavelengths. As for multiple wavelengths, AAE can be fitted over the range of all wavelengths using the power-law expression in

$C_{Abs,\lambda} = k_0(\frac{\lambda}{\lambda_0})^{-AAE}$, where k_0 is a prefactor and λ_0 is an arbitrarily chosen wavelength.

In particle optics, the ratio of a characteristic particle dimension and the wavelengths, termed size parameter *x*, is scale invariant, meaning millimeter waves interact with millimeter-sized particle exactly the same way as micrometer waves with micrometer-sized particles as long as the particle shape and the complex refractive index are the same. For a spherical particle, the size parameter *x* is calculated as

$$x = \frac{2\pi r}{\lambda}. \tag{1.7}$$

The interaction of light with particles can be categorized into three regimes based upon the size parameter *x*. In Rayleigh regime, where $x \ll 1$, particles are considered small relative to the incident wavelength. Upon illumination, whole volume of the particle is involved in the interaction with incident light, yielding particle C_{Abs}, corresponding to the incoherent process that transfer electromagnetic energy into thermal energy, is proportional to the particle volume, whereas particle C_{Sca}, representing coherent addition of scattered wavelets, is proportional to the particle volume squared. On the other hand, there is geometric regime where particles size is much larger than the wavelength ($x \gg 1$). Incident light is attenuated by the particle exterior prior to fully sampling the particles volume, and thereby particle C_{Abs} is proportional to the particle surface area. In between Rayleigh regime and geometric regime, where particle size is comparable to the wavelength ($x \approx 1$), is the transition regime where particles are changing from volume absorbers to surface absorbers.

1.1.2 Light Absorption by Spherical Particles: Mie Theory

The Mie solution to Maxwell's equations, commonly referred to Lorenz-Mie theory or Lorenz-Mie-Debye theory, provides an analytical solution of Maxwell's equation for the scattering of an electromagnetic plane wave by spherical particles in terms of infinite series. Bohren and Huffman provided a computer program to calculate Mie scattering based upon models of a homogeneous sphere and a coated sphere[26], which have been widely applied in climate models. For example, aged BC particles are commonly assumed to collapse into near-spherical particles concentrically coated with other absorbing or non-absorbing compounds through atmospheric processing, while BC core after removal of coating by processes, i.e. thermal denudation, are approximated as a homogenous sphere. Based upon these assumptions, a wide variety of properties, including absorption enhancement, single scattering albedo and wavelength dependent optical properties, are studied[27-29]. Mie theory has also been extended to the calculation of scattering from spheres coated with multiple layers[30], slightly distorted spheres[31,32], anisotropic spheres[33,34], spheroids[35], coated concentric cylinders[36], and other variations[37].

As a relevant example of Mie calculation, Fig. 1.3 demonstrates how MAC, MSC and ϖ_0 vary as a function of size parameter x ($\pi D_p/\lambda$) at wavelength λ=550 nm, assuming a refractive index of m = 1.77 + i0.8 and mass density of ρ=1.8 g cm^{-3}. In this figure three ranges are evident: 1) for x <<1 (Rayleigh regime), MAC is constant meaning the particle acts like a volume absorber with C_{Abs} scaling with particle volume (~D_p^3), while MEC increases proportional to D_p^3 with C_{Sca} scaled as D_p^6 resulting in a strong single scattering albedo ϖ_0 increase with D_p; 2) at the vicinity of

x≈1 where D_p is comparable to the wavelength, MAC and MSC are maximized due to internal resonances; and 3) for x >>1 (geometric regime), MAC and MSC are inversely proportional to Dp where the particle acts like a surface absorber and scatterer that both C_{Abs} and C_{Sca} scale with D_p^2.

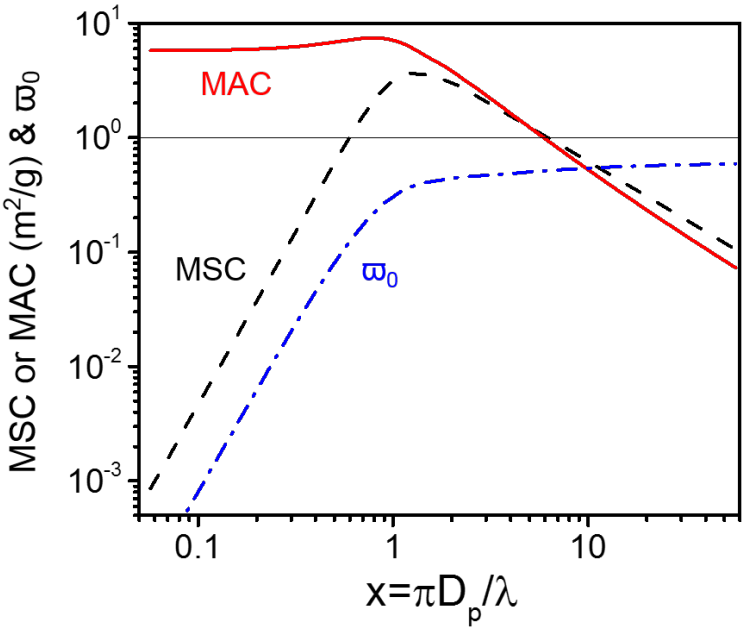

Figure 1.3 *Mie calculations of mass specific scattering cross section (MSC), mass specific absorption cross section (MAC) and single scattering albedo (ϖ_0) as a function of size parameter x for a homogeneous sphere with density of 1.8 g cm^{-3} and refractive index of 1.77 + i0.8.*

1.1.3 Light Absorption by Fractal Aggregates: Multiple Sphere T-Matrix Method

Despite the wide application in climate models, Mie solution of Maxwell's equations is available only for some simple particles shapes. Calculation of absorption and scattering from particles of arbitrary shape requires approximation or

more advanced numerical methods. For example, BC particles from combustion, an important category of tropospheric aerosols that are strongly absorptive within solar spectra, are fractal-like agglomeration of BC spheres, optical properties of which can only be approximately calculated by the traditional Mie theory. Firstly introduced by Waterman in 1965[38], the numerically exact superposition T-matrix method has evolved rapidly and is used for a variety applications including homogeneous spheroids and other symmetric particles.[39-42] Later, Mackowski[43], and Mackowski and Mishchenko[44] developed the multiple sphere scattering T-matrix algorithm (MSTM) which enables calculation of optical cross sections of multi-sphere clusters and ensembles of randomly oriented particles. The T-matrix method has been used to study scattering properties of soot aggregates with homogeneous carbonaceous soot monomers, showing that the effects of aggregate fractal morphology and size on the extinction, scattering, and absorption properties of soot aerosols to be significant[45-47].

Despite the ability to handle computation of optical properties for non-spherical morphologies, MSTM should be consistent with Mie theory with regards to a homogeneous sphere or a coated sphere. Figure 1.4 evaluates the extent of agreement between MSTM and Mie theory in calculating optical cross sections, including extinction cross section C_{Ext}, scattering cross section C_{Sca} and absorption cross section $C_{Abs.}$ The calculations are based on a homogeneous sphere model and a coated sphere model assuming a particle diameter of 250 nm. A refractive index (RI) of $1.77 + 0.8i$ was assumed for the homogeneous spheres, as well as the core of the coated spheres; shell RI of coated sphere was assumed to be 1.5 (i.e. transparent shell).

For homogeneous spheres, the calculated cross sections using MSTM agrees with those calculated with Mie within 0.1 %. The adifferences in C_{Sca} calaculated with MSTM and Mie are negligible for a 250 nm particle over λ=500 nm to 850 nm, and for a particle with varying diameter (100 nm to 400 nm) at λ=550 nm. Spectrally, C_{Ext} and C_{Abs} calculated using MSTM are increasingly higher than the Mie prediction towards the shorter wavelengths with a maximum deviation of ≈ 0.11 % in C_{Abs} at λ=500 nm. MSTM also predicts higher C_{Ext} and C_{Abs} at λ=550 nm for particles with varying diameter (100 nm to 400 nm). For coated spheres, all optical cross sections calculated by MSTM agree with Mie prediction within 0.015 % spectrally and for particles with varying core (diameter ranging from 50 nm to 200 nm).

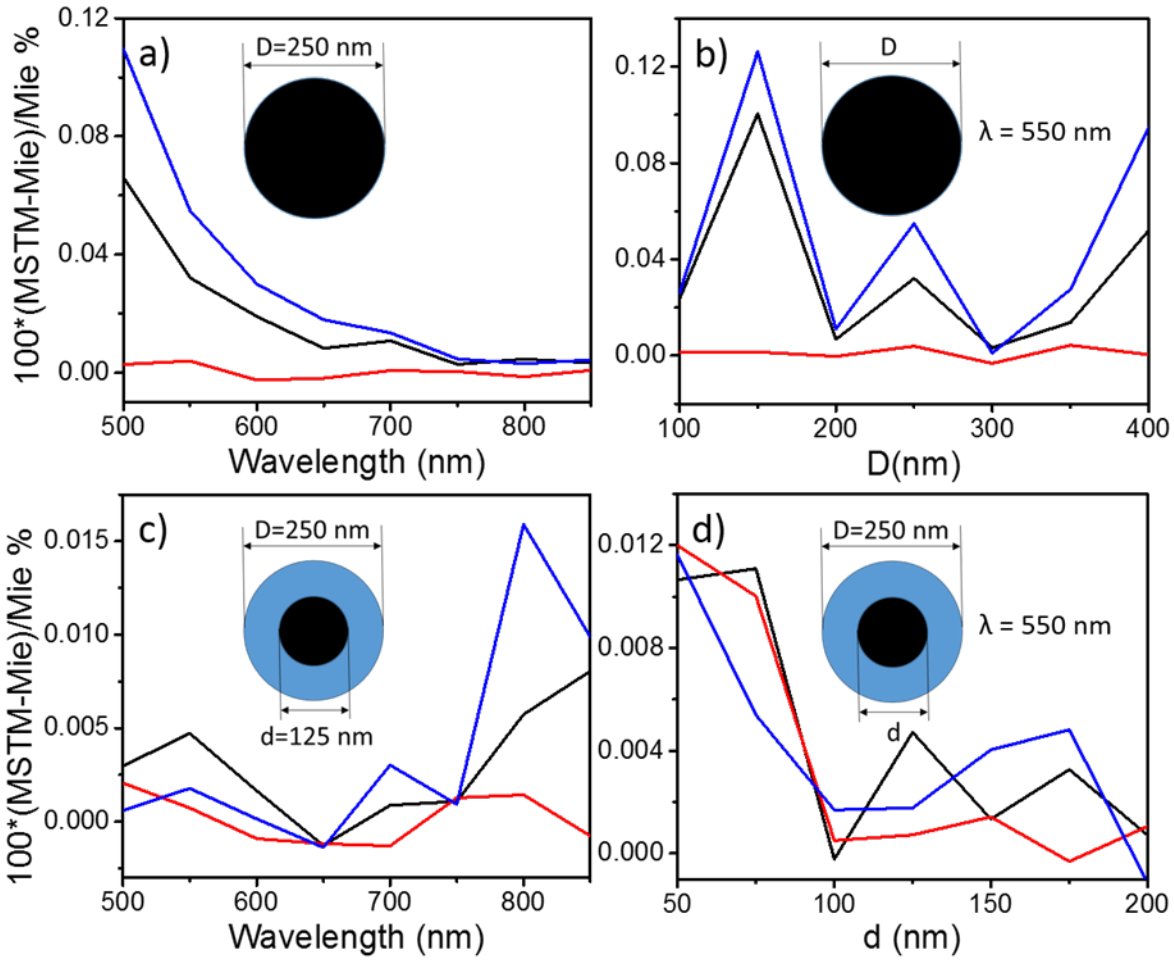

Figure 1.4 *Comparison of Mie theory vs. MSTM in calculating optical cross sections of a) 250 nm diameter homogeneous versus wavelength, b) homogeneous sphere with varying diameter at λ=550 nm, c) coated sphere with a core diameter of 125 nm and total diameter of 250 nm versus wavelength, and d) coated sphere with varying core diameter d and a fixed total diameter D of 250 nm measured at λ=550 nm. Black lines, red lines and blue lines represent C_{Ext}, C_{Scat} and C_{Abs}, respectively. Cartoons describe the material, size and morphology of particles used in calculation, in which black represents absorbing materials with RI of 1.77 + i0.8, while blue represents pure scattering material with RI of 1.5.*

1.2 Apparatus

1.2.1 Differential Mobility Analyzer

Particle size, one of the most important physical properties of aerosols, can be characterized with a variety of techniques that are generally categorized into *ex situ* technique and *in situ* techniques. *Ex situ* techniques, including electron microscopy, X-ray diffraction and atomic-force microscopy, provide straightforward visual observation of particle size or down to sub-nanometer resolution, yet are time-consuming and are unrealistic to be implemented for the characterization of size distribution. *In situ* techniques, including various ion-mobility methods, dynamic light scattering and analytical ultracentrifuge *etc.*, provide fast and accurate characterization of particle size and size distribution. Among all *in situ* techniques, the differential mobility analyzer (DMA) is the standard characterization method to obtain complete mobility size distribution of nanoparticles in aerosol phase.[48]

DMA characterizes particle size based upon electrical mobility of nanoparticles. The principle of instrument operation can be demonstrated in a schematic of a cylindrical DMA as shown in Fig. 1.5. The DMA consists of two concentric electrodes, between which an electrical field is applied. The inner electrode is maintained with a controlled negative voltage, typically ranging from 1V to 10 kV, while the outer electrode is electrically grounded. When a flow of poly-dispersed aerosol (Q_a), is introduced into the annular area between electrodes, positive-charged particles are attracted to the inner electrode maintained at a negative potential. Particle-free sheath air (Q_{sh}) is also introduced at the top of the DMA and passes down the annulus as a laminar stream without mixing with the aerosol flow.

Trajectories of aerosols are determined by the equilibrium of electrical force and drag force exerted on the particles[49]. As a result, for an applied voltage V_e, only particles with electrical mobilitygiven by

$$Z_p = \frac{(Q_{sh}+Q_e)}{2\pi L_d V_e} \ln \frac{R_{out}}{R_{in}}, \tag{1.8}$$

will flow out of the "monodisperse" outlet. The quantity L_d is the "active" length of DMA classification region, and R_{out}, R_{in} are radii of the outer and inner electrodes, respectively, as shown in Fig. 1.5. For a spherical particle, the electrical mobility is related to diameter D_p via Stokes' law as

$$D_p = \frac{neC_c(D_p)}{3\pi\eta Z_p}, \tag{1.9}$$

where n is the number of unit charges, e is elementary unit of charge (1.61×10^{-19} C), η is viscosity of the gas medium. The term, a function of D_p, is the Cunningham slip correction factor that accounts for noncontinuum effects when calculating the drag on small particles. A widely used expression for C_c is expressed as[50]

$$C_c(D_p) = 1 + \frac{2\lambda}{D_p}[A_1 + A_2 \exp(-\frac{A_3}{2\lambda/D_p})], \tag{1.10}$$

where λ is the mean free path of gas, and A_1, A_2 and A_3 are empirical constants with values of 1.142, 0.558 and 0.999[51], respectively.

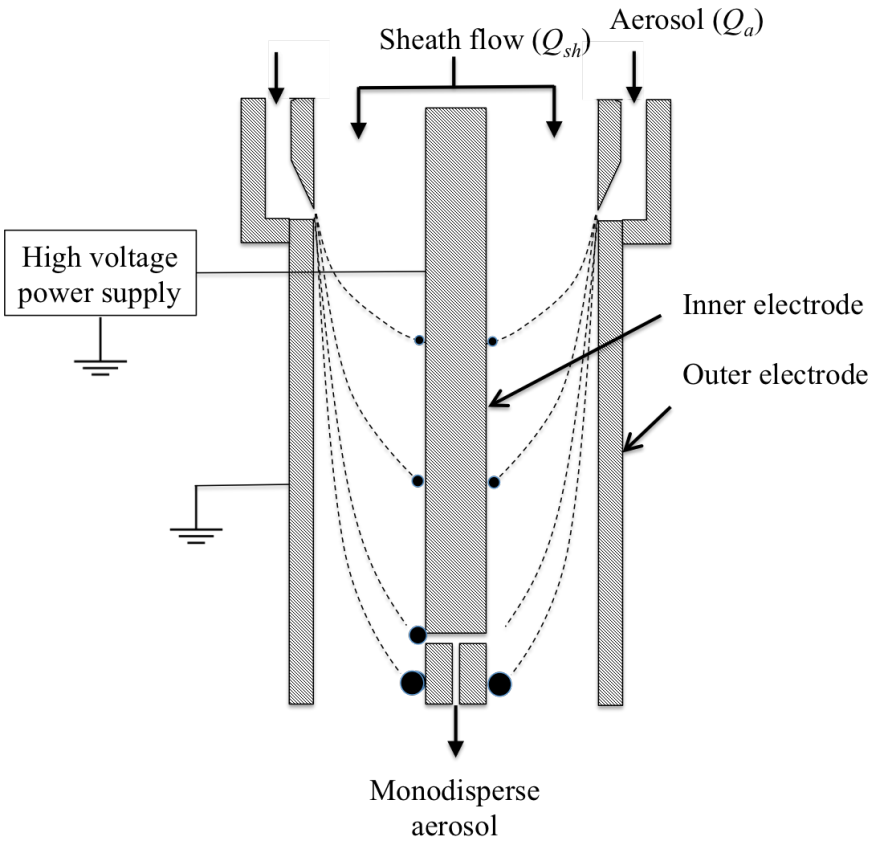

Figure 1.5 *Schematic of DMA.*

The resolution of the DMA is characterized using a transfer function, which is a measure of the transfer efficiency of aerosol particles passing through the sampling slit for a selected electrical mobility. Knutson and Whitby elegantly derived the transfer function of the DMA based upon streamline analysis, which is expressed in terms of measurable quantities, including flow rates and the electrode voltage.[49] Stolzenburg extended the Knutson-Whitby analysis to the case of diffusing particles and derived the diffusional spreading of the DMA transfer function.[52]He expressed the transfer function as a convolution of the non-diffusive transfer function with a Gaussian distribution as in

$$\Omega(\tilde{V}) = \frac{\sigma}{\sqrt{2}\beta}\left[\epsilon\left(\frac{\tilde{V}-(1+\beta)}{\sqrt{2}\sigma}\right) + \epsilon\left(\frac{\tilde{V}-(1-\beta)}{\sqrt{2}\sigma}\right) - 2\epsilon(\frac{\tilde{V}-1}{\sqrt{2}\sigma})\right], \quad (1.11)$$

where $\epsilon(x) = x\,\mathrm{erf}(x) + \frac{1}{\sqrt{\pi}}\exp(-x^2)$, β=Q_a/Q_{sh}, $\tilde{V} = V_0/V_0^*$, $V_0^* = \frac{Q_{sh}\ln(r_{out}/r_{in})}{2\pi L Z_p}$, $\sigma^2 = G\widetilde{D}$, $\widetilde{D} = \frac{2\pi LD}{Q_{sh}}$ (D is the size dependent diffusion coefficient), $G = \frac{4(1+\beta)^2}{1-\gamma}[I_\gamma(\gamma) + (2(1+\beta)\kappa)^{-2}]$, $\gamma = (r_{out}/r_{in})^2$, $\kappa = Lr_{out}/(r_{out}^2 - r_{in}^2)$. The term $I_\gamma(\gamma)$ is described as

$I_\gamma(\gamma) = \frac{1}{2}(1+\gamma)$ for plug flow, and as

$I_\gamma(\gamma) = \frac{[\frac{1}{4}(1-\gamma^2)(1-\gamma)^2 + \frac{5}{18}(1-\gamma^3)(1-\gamma)\times\ln(\gamma) + \frac{1}{12}(1-\gamma^4)\ln(\gamma)^2}{[(1-\gamma)[-\frac{1}{2}(1+\gamma)\ln(\gamma) - (1-\gamma)]^2]^{-1}}$ for inviscid flow.

The great advantage of Stolzenburg's model is its generality. One can assess the effects of diffusion on the transfer function as a function of the particle size, the flow ratio through the DMA, and the length of the DMA on the transfer function. In this dissertation, I adopted Stolzenburg's model to evaluate the transfer function of the DMA numerically.

1.2.2 Photoacoustic Spectrometer

Photoacoustic spectroscopy (PA) is a real time technique that can characterize light absorption by all phases of matter[53,54], but is especially practical and robust for quantifying light absorption by gases and aerosols as demonstrated by balloon borne detection of trace gases in the stratosphere[55] and by aircraft borne measurements of light absorption by aerosols[56]. Photoacoustic measurements of light absorption by aerosols differs from that in gases in terms of the time response of heat transfer of absorbed electromagnetic energy by particles versus gases. The ability to make such measurements for aerosols has been realized in the past two decades.[57,58].

As light illuminates aerosols, photon energy is absorbed by the aerosols concomitant with heat transfer from particles to the surrounding air. Upon receiving this heat, the surrounding air expands and creates a pressure disturbance or sound wave. The conversion of light into sound is known as the photoacoustic effect. Based upon this effect, PA uses a microphone to detect the sound wave, signal of which is conditioned by a low-noise pre-amplifier. The resonator of PA is designed with an acoustic resonance frequency to couple with the modulated laser beam and sample flow, thereby acoustic pressure is maximized at pressure nodes that reduces the influence of window noise, due to light absorption on optical windows, and of flow noise, due to pressure fluctuations of sample flow. A variety of acoustic resonators have been developed in prior studies.[59-61] Gillis *et al.* in NIST designed a PA resonator with a calculated cell constant and benchmarked its performance in applications related to climate change measurements.[62,63] A PA resonator with similar design as in Gillis model is adopted in the experiment of this dissertation.

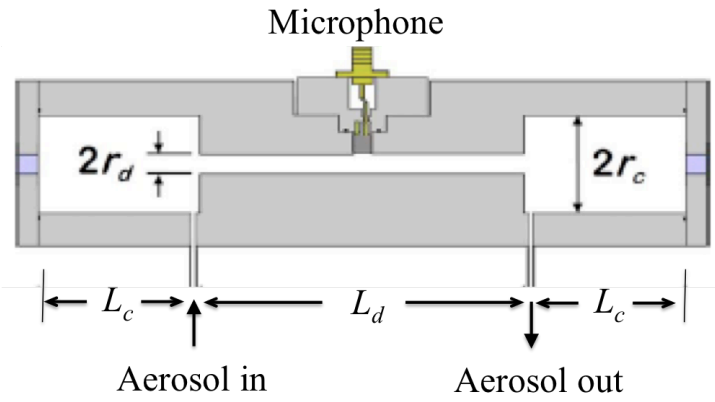

Figure 1.6 *Schematic of PA resonator used in this work with nominal dimensions L_d= 100mm, $2r_d$=6mm, L_c=50 mm, and $2r_c$=30 mm. The microphone is located in the midway between the ends of the duct.*

Light absorption coefficient σ_{Abs} can be determined from the acoustic pressure P_m, measured with the calibrated microphone, resonator quality factor Q, resonance frequency f_0, the Fourier component of laser beam power P_L at f_0, and resonator cross sectional area A_{res} as in[53]

$$\sigma_{Abs} = P_m \frac{1}{P_L} \frac{A_{res}}{\gamma - 1} \frac{\pi^2 f_0}{Q}, \tag{1.12}$$

where γ=1.4 is the ratio of isobaric and isochoric specific heats for air. The quality factor Q of the acoustic resonator is an amplification factor provided by the standing acoustic wave, representing the ratio of the energy stored in the resonator to the acoustic energy dissipated per acoustic cycle. Recent studies[58,62] implemented a two-phase lock-in amplifier (LIA) for measurement of microphone signal to account for the effect of microphone noise that can induce non-zero offset when laser power is zero. The coefficient σ_{Abs} is expressed as

$$\sigma_{Abs} = \frac{\sqrt{(x - x_0)^2 + (y - y_0)^2}}{C_c \beta_m W_{RMS} \sqrt{8}}, \tag{1.13}$$

where C_c is the cell constant describing instrument response, β_m is the microphone sensitivity, W_{RMS} is the root mean square of the laser power, and x and y are the in phase and out of phase signals from the LIA, respectively. The background signal when laser power is off is measured as x_0 and y_0. Presently $C_c\beta_m$ is 0.187 V m W^{-1} for the PA used in this dissertation, measured using a constant-amplitude sound source [63].

1.2.3 Aerosol Particle Mass Analyzer

The aerosol particle mass analyzer (APM) classifies particle based upon their mass to charge ratio.[64] Particle mass can be determined by the APM with knowledge of number of charges on the particle. In recent decades, the APM has been employed as

a direct measurement of particle masses[65,66], which is particularly useful for non-spherical single or aggregate particles, or when the particle density is unknown or varies during a certain process[67,68]. The APM has also been used, often in combination with a DMA, for evaluating various particle properties such as "effective" density[68,69], morphology through estimation of the mass-mobility exponent[65,70,71], mixing ratio of internally-mixed particles[72], volume[73] and porosity[74].

The APM separates particles by balancing the electrostatic and centrifugal forces on charged particles. The classification area is the annulus gap between two concentric cylinders that rotate at the same angular velocity ω. A voltage V is applied on the inner cylinder with the outer cylinder electrically grounded resulting in a uniform electric field between the cylinders. Flowing axially through the gap, aerosols experience radial electric and centrifugal forces, which act in opposite directions. Particles transit the APM to the downstream detector when the force balance is achieved, which can be described as

$$m_p r\omega^2 = \frac{neV}{r\ln(r_{out}/r_{in})}, \tag{1.14}$$

where m_p is the particle mass; n, e, r_{out} and r_{in} have the same definition as for the DMA. The value r represents the radius of the center of the annular classification space, i.e. $r = (r_{out} + r_{in})/2$. The underlying assumption is that electric field is uniform within the classification space since the width of the annular gap is small compared to r. Note that a unique solution for m_p/ne does not exist for a given ω and V. Hence an effective mass is measured by APM for n> +1, where is m_{eff} defined as m_p/ne. Since m_{eff} varies solely in proportion to the applied voltage and rotation speed,

properties of particles such as shape, morphology or orientations play no role in the mass classification.

Similar to the DMA, the transfer function of APM evaluates the performance of mass classification by the APM, which is determined solely by the non-dimensional quantity termed the classification performance parameter λ_c as in

$$\lambda_c = \frac{2m_p B\omega^2 L}{v_0}, \tag{1.15}$$

where L and v_0 are the length of the classification area and volumetric flow rate of aerosols, respectively. The term B is the mechanical mobility and is equal to $C_c(D_p)/3\pi\eta D_p$. The classification parameter measures the separation ability of APM, which can be interpreted as the ratio of axial and radial transversal times.

1.2.4 Condensation Particle Counter

The condensation particle counter (CPC) is an aerosol number concentration measuring device that is capable of detecting ultra fine particles (down to 20 Å in diameter) over a wide concentration (from about 100 particles/cc to 10^7 particles/cc). Unlike electrostatic methods only applicable to charged particles[75], CPC is the only technique available for detecting neutral gas-borne particles that are too small for optical methods.

The fundamentals of CPC operation consist of three processes, involving super-saturation of a working fluid, growth of particles by condensation of vapors, and detection of aerosol particles. Figure 1.7 shows a schematic of the CPC operation. Aerosols are saturated with vapor when passing through vaporized working fluid kept at an elevated temperature. The vapor subsequently becomes supersaturated and

condensates at the particles, causing growth of particle to the size detectable optically by light transmission[76,77] or by light scattering techniques. Based upon the configuration employed to super-saturate the working fluid, CPCs can be generally categorized into (adiabatic) expansion and continuous flow. In expansion type CPCs, super-saturation is achieved by adiabatically expanding the volume where saturated aerosols are trapped, and thereby particle size increases due to condensation of vapor. In continuous flow CPCs, super-saturation is realized by cooling saturated aerosols in a lower temperature condenser tube, or by blending cool aerosols with warmed air that contains saturated vapor. In the last decades, the most commonly used CPCs employs butanol as working fluid, and are capable of well defined detection limits with lower size limits below 3 nm[78]. Recent progress in CPCs includes development of water-based CPC that shows equivalent concentration measurements in field measurement.[79,80]

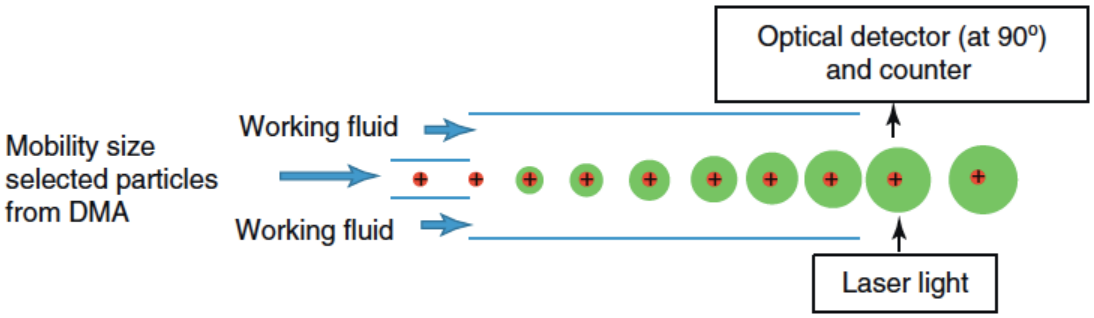

Figure 1.7 *Schematic of CPC Operation.*[81]

1.3 Scope of the Dissertation

The dissertation focuses on the characterization of light absorption by atmospherically relevant carbonaceous aerosols using a photoacoustic spectrometer combined with aerosol-based classification methods, which can be categorized into

two main areas. Firstly, calibration techniques were developed for instruments involved in the *in situ* absorption measurement, i.e. DMA for mobility size measurement and PA for light absorption measurement. These techniques are described in Chapter 2 and Chapter 3, respectively. Bionanoparticles were confirmed to be a promising reference material to determine particle diameter from ion-mobility measurement. The true distributions of bionanoparticles were evaluated numerically to explain the broadening of measured size distribution. Several monodisperse candidate particles consisting of fullerene C_{60}, copper and silver, were assessed for calibration of absorption measurements for PA as well.

In the second part, which involves Chapter 4 and Chapter 5, I demonstrated that a laboratory-generated aerosols mimicked carbonaceous particles in the atmosphere in regard to the absorption spectra . Optical absorption enhancement of BC was found to be wavelength independent, which arises from other species of aerosols mixed with BC and is affected by the manner in which BC is mixed. Optical absorption spectra were also taken for size and mass selected smoldering smoke produced from six types of commonly seen wood in a laboratory scale apparatus. Finally, Chapter 6 summaries the work of *in situ* optical absorption measurement of atmospherically relevant aerosols and presents detailed discussion of future improvements for each part of the project.

Chapter 2: Bio-Materials as Candidate Reference Materials for Mobility Analysis of Nanoparticles

2.1 Introduction

With the proliferation of nanoparticle based materials in applications as diverse as photonics to nanomedicine, and the associated concerns about exposure and toxicology, reliable metrology characterization tools and materials necessary to calibrate them are needed.[82]

One methodology that is widely used for general nanoparticle metrology is differential mobility analysis (DMA) and its variant electrospray differential mobility analysis (ES-DMA).[83] Characterization based on the DMA is a very powerful instrumental approach for measuring the mobility/size distribution of nanoparticles in the gas phase. The method relies on a characterization of the electrical mobility Z_p of aerosolized nanoparticles (NPs) by balancing the electric and drag force on the particles. The relationship between particle diameter D_p and electrical mobility Z_p is shown in Eq. 1.10.

While this ion-mobility approach offers superior resolution and accuracy, this can only be realized by an absolute calibration, using a well-calibrated source. Various non-certified RMs and standard reference materials (SRM) for nanoparticle sizing are commercially available[84], including polystyrene latex spheres (PSLs), metallic NPs (e.g. colloidal gold and silver NPs) and metal oxides (e.g. colloidal silica), in the form of particle suspensions, in which non-volatile additives, like citrate, are very often added to stabilize the particles in the solution. One difficulty in

the production of these standards is that it is not possible to synthesize a new batch of particles with an identical size distribution as a previous batch. Thus it is not possible to issue a replacement standard with the same particle mobility/size as a previous standard.

In contrast to "engineered" NPs as described above, biologically-derived materials, referred to as bio-nanoparticles henceforth, offer a precision in reproduction that cannot be matched. The size and shape of each bio-nanoparticles is highly repeatable. This can lead to an almost perfectly mono-dispersed aerosol while the "engineered" nanospheres have relatively broad distributions for sizes of 60 nm and less. Moreover, since commercially available bio-nanoparticles are usually lyophilized (available as dry powders) to keep the samples stable, their suspensions can be made at as high concentrations as required.

Currently a series of unique molecular ions (tetra-alkyl ammonium ions) is being used in the calibration of high flow DMAs capable of measuring mobility over the range (5 ~100)$\times 10^{-6}$ m^2 V^{-1} s^{-1} (diameter of 1 nm to 6 nm).[85,86] The widely used low flow nanoDMAs (TSI, Grimm etc.) are capable of measuring mobilities in the range of (0.06~20)×10-6 10^{-6} m^2 V^{-1} s^{-1} with diameters ranging from 3nm to 60 nm). The bio-nanoparticles considered in this study cover the size range appropriate for the calibration of the low flow DMAs.

In this work I explore using biologically derived materials as potential particle mobility/size standards for the DMA. The first implementation of ES-DMA to bio-nanoparticles can be traced back to 1996, when Kaufman et al. measured globular proteins ranging from 3 nm to 14 nm.[87] Subsequently researchers have presented the

application of this technique to other specific bio-nanoparticles such as polymers, viruses, bacteriophages etc.[88-91] Most of them, however, were investigated only at a modest resolution, and the actual width of the mobility size distributions remained unknown. One recent study by A. Maiβer using high flow DMA included bovine serum albumin (BSA), which is included in our study, to provide an overlap between the high flow and low flow DMA measurements.[85] Here I systematically investigated five different bio-nanoparticles: BSA, polyclonal human immunoglobulin (IgG), a glycoprotein with a high glyan heterogeneity, phage PP7, coliphage PR772 and tobacco mosaic virus (TMV) with size ranging from 6 nm up to 64 nm. The measurements of these materials were compared with high precision "engineered" nanoparticles: gold colloids (AuNPs) and polystyrene latex beads (PSL). I also calculated corresponding transfer functions and corrected for its contribution to the measured distribution in order to provide a more accurate estimate of the true width of the size spectrum for each aerosolized bio-nanoparticle. To demonstrate the stability of these bio-nanoparticles, the mobility/size was measured for a range of bio-nanoparticle suspension concentrations and buffer molarities. Day-to-day variation of mobility/size was also evaluated. I conclude from these results that bio-derived material offers significant advantages compared to most "engineered" nanoparticles. It is worth noting that size measured by DMAs could differ from device to device up to 15% even for same analyte.[92] Hence the model of equipment should be specified and round robin test is important before assigning the value for reference material, which is beyond the scope of the discussion in this chapter.

2.2 Materials and Methods

2.2.1 Electrospray Particle Generation and Differential Mobility Measurements

I measured the size distribution with an ES-neutralizer-DMA-condensation particle counter (ES-neutralizer-DMA-CPC) system described previously.[93] Suspended bio-nanoparticles were first aerosolized using a 40 μm inner diameter capillary mounted in an electrospray (TSI Inc., Shore View, MN, #3480) with the chamber pressure of 2.55×10^4 Pa (3.7 psi) and a carrier gas of 20 $cm^3\ s^{-1}$ (1.2 L min^{-1}) purified air. The aerosolized droplets were then charge-reduced in a Po-210 radiation source so that most aerosols carry -1, 0 or +1 charge. A negative voltage was applied to the central electrode of a Nano DMA (TSI Inc., #3085) such that the +1 charged particles passed through the DMA and were counted by a condensation particle counter (CPC) (TSI Inc. #3025A). The counting efficiency of the CPC is over 95% for the investigated sizes. Two modules of mass flow controller (MKS Inc., #M100B), 333.3 $cm^3\ s^{-1}$ (20,000 sccm) and 500 $cm^3\ s^{-1}$ (30,000 sccm) were used to control the sheath flow in the DMA. The uncertainty in the flows are ± 5 $cm^3\ s^{-1}$ (300 sccm) and ±10 $cm^3\ s^{-1}$ (600 sccm) respectively.

The investigated bio-nanoparticles were split into two groups based on their expected mobility size. For smaller particles, i.e. IgG, BSA and PP7, a high sheath flow rate of 500 $cm^3\ s^{-1}$ (30 L min^{-1}) was adopted to reduce the broadening of the DMA transfer function from Brownian motion. For the larger particles i.e. PR772 and TMV, a sheath flow rate of 83.33 $cm^3\ s^{-1}$ (5 L min^{-1}) was used so that the largest particle could be sampled at a voltage below the maximum value of 10,000 V for the power supply. Due to anticipated narrow size distributions of bio-nanoparticles, the

ratios of the sheath to aerosol flow were chosen to be large, about 42 for smaller particles and 33 for the larger ones. Since the resolution in a DMA scales as the ratio of the sheath to aerosol, the operating resolution of the DMA is higher than what is normal practice. To ensure this resolution the DMA was operated in a voltage stepping mode with an interval of 25 s at high sheath flow, and 40 s under low flow rate, which ensured that the residence time from DMA inlet to the CPC detector was smaller than the dwell time. The scanning interval is chosen to be 0.2 nm for the smaller bio-nanoparticles, 0.05 nm for BSA, and 1nm for the larger ones. For the purpose of equipment calibration, NIST SRM PSL of 100.7 nm, SRM1963, was used in the measurements of big bio-nanoparticles while 30nm citrate-stabilized AuNPs (Ted Pella Inc.), size-calibrated by SRM 1963, was employed in those of small biomolecules. For the size distribution measurement of citrate-stabilized AuNPs I refer the readers to Hinterwirth's paper[94] that gives comparative assessment of several characterization methods and shows ES-DMA has the highest size resolution.

The voltage associated with centroid electrical mobility was assigned by averaging the means of Gaussian fits to three replicate measurements. Electrical mobility of each bio-nanoparticle was calculated as below.

$$Z_p = \frac{Q_{sh} \ln \frac{r_{out}}{r_{in}}}{2\pi V_e L_d}, \tag{2.1}$$

where Q_{sh} is the sheath flow rate, r_{out} and r_{in} the outer and inner radii of DMA column, V_e the voltage applied on electrodes and L_d the length of DMA column. The mobility size in this paper was calculated using Eq. 1.10, in which the slip correction factor is given by

$$C_c(D_p) = 1 + K_n[A_1 + A_2 \exp(-A_3/K_n)] \quad (2.2)$$

where K_n is twice the mean free path of air divided by the particle diameter($K_n=2\lambda/D_p$) and A_1=1.142, A_2=0.558 and A_3=0.999.[51] Equation 2.2 is an empirical expression. An alternative expression [90] that has been suggested for describing the relationship between mobility and particle diameter for small particles in the size range less than 10 nm. The fundamental quantity accurately measured by the DMA is the mobility of the particle, while the determination of the mobility diameter has additional uncertainty from the use of Eq. 2.2. I present our results in terms of mobility diameter as well as mobility because of the widespread use of mobility diameter in the aerosol community.

2.2.2 ES-DMA Buffer Preparation

Twenty mM ammonium acetate buffer solutions (AmAc) were prepared by dissolving 0.77 g of ammonium acetate powder (Sigma Aldrich, St. Louis, MO, #631-61-8) in 0.5 L of de-ionized water (18 MΩ cm^{-1}, Barnstead nanopure UV system) filtered by 0.2 μm pores. Ten and two mM buffers were then obtained by diluting with filtered de-ionized water.

2.2.3 Bio-nanoparticle Suspension Preparation

I found that to obtain a well-shaped mobility spectra with minimal capillary clogging of the electrospray the optimized sample concentration should yield a CPC count ranging from 2000 particles cm^{-3} to 6000 particles cm^{-3}. The easiest approach to achieve this target was to start with highly concentrated solutions and dilute with buffer. For BSA (Sigma Aldrich, St. Louis, MO, # A9418), and human IgG (Sigma

Aldrich, St. Louis, MO, # 14506), the initial solution was prepared by suspending 1 mg in 1 mL of 20 mM AmAc. The solution was then diluted to be 100 μg mL^{-1} and denoted as 1× dilution. Phage PP7 from ATCC (Manassas, VA; accession numbers 15692-B4) and PR772 (Felix d'Herelle Reference Center for Bacterial Viruses, Universite Laval, Quebec, Canada) were prepared as described in a previous paper. [95] The initial solutions were obtained with a concentration of 2.5×10^{13} plaque forming units/cm^3 (pfu cm^{-3}) and 1.5×10^{12} pfu cm^{-3}, respectively. The phages were then dialyzed into 20mM AmAc and adjusted to $2.1x10^{11}$ pfu cm^{-3} for PP7 and 1.25×10^{10} pfu cm^{-3} for PR772 in 1× dilution. A TMV suspension (James N. Culver's Lab, UMD) with an initial concentration of 15 mg mL^{-1} was diluted to 50 μg mL^{-1} with 2 mM AmAc for 1× dilutions. Samples with five (5×) and ten (10×) times dilutions were also made to assess the effect of concentration on the mobility size. To assess the stability of bio-nanoparticle size in buffers with different molarities, 10 mM and 2 mM AmAc were used to prepare 5× solutions for IgG and BSA as well as 1× solutions for PP7 and PR772. For TMV, 1× solutions were also prepared using 10 mM and 20 mM buffers.

2.2.4 "Engineered" NPs Suspension Preparation

Size distributions of "engineered" NPs including 10 nm, 20 nm, 30 nm and 60 nm citrate-stabilized monodispersed colloidal AuNPs (Ted Pella Inc.) were measured. A suspension (1.5 mL) of 10 nm AuNPs were first centrifuged at 13.2 kRPM for 40 min to remove most of the supernatant, and then replaced with an equivalent volume of 2 mM AmAc. This process was repeated to remove the citrate stabilizer, which forms a residue on the surface of the gold particle if not removed. The same

procedure was applied to 20 nm, 30 nm and 60 nm AuNPs by changing the centrifuge time to 15 min, 3 min and 1 min, respectively. For the PSL spheres, a drop of SRM 1963 was mixed with 1mL of 2mM AmAc and diluted 6 times. The same procedure was applied to 30 nm PSLs (Thermo Scientific. 3030A) and 60 nm PSLs (NIST SRM1964) with a dilution factor of 20 for the 30 nm sample and 10 for the 60 nm sample.

2.3 Results and Discussions

2.3.1 Homogeneity of Bio-nanoparticle

Comparison of Measured Distribution with Engineered Particles Figure 2.1 shows a typical plot of number concentration reduced by the peak value, $N_r(Z_p)$, versus mobility for bio-nanoparticles, and comparison to AuNPs and PSLs spheres. The standard deviation of the mobility distribution $\sigma_{Zp,exp}$ and that of the size distribution $\sigma_{Dp,exp}$ are listed in Table **Error! Reference source not found.**1. The reduced standard deviation $\sigma_{r,Zp,exp}$ and $\sigma_{r,Dp,exp}$ are calculated as

$$\sigma_{r,Z_p,exp} = \frac{\sigma_{Z_p,exp}}{Z_p}, \sigma_{r,DZ_p,exp} = \frac{\sigma_{D_p,exp}}{D_p} \tag{2.3}$$

In all cases the bio-nanoparticles have narrower width of $N_r(Z_p)$ with reduced standard deviations that did not exceed 0.047. Remarkably the TEM images show that TMV folds after electrospray[96], but still maintains a narrow distribution with a $\sigma_{r,Zp,exp}$ of 0.021. In contrast, among the engineered particles only SRM 1963 (PSL 100.7nm) has a comparable distribution with a $\sigma_{r,Zp,exp}$ of 0.033. For size of 30 nm the

colloidal gold samples are by far the better of the "engineered" particles relative to PSLs

Table 2.1 Standard deviation of distribution of bio-nanoparticles and "engineered" NPs.

	Z_p (10^{-8} $m^2V^{-1}s^{-1}$)	$\sigma_{Zp,exp}$ (10^{-8} $m^2V^{-1}s^{-1}$)	$\sigma_{r,Zp,exp}$	D_p (nm)	$\sigma_{Dp,exp}$ (nm)	$\sigma_{r,Dp,exp}$
Bio-particles						
BSA	465.9	21.8	0.047	6.80	0.16	0.023
IgG	261.2	11.2	0.043	9.11	0.20	0.022
PP7	36.99	0.736	0.020	24.58	0.22	0.009
PR772	6.41	0.292	0.046	61.64	1.42	0.023
TMV	6.09	0.127	0.021	63.38	0.70	0.011
"Engineered" NPs						
AuNP 10nm	193.2	12.2	0.063	10.6	0.343	0.032
AuNP 20nm	52.48	3.96	0.075	20.6	0.824	0.040
AuNP 30nm	24.01	1.03	0.043	30.8	0.714	0.023
PSL 30nm	25.74	4.57	0.178	30.26	3.754	0.123
AuNP 60nm	6.439	0.611	0.095	62.0	3.319	0.054
PSL 60nm	6.255	0.479	0.077	62.8	3.003	0.048
PSL 100.7nm	2.641	0.088	0.033	101	1.769	0.018

in terms of mono-dispersity. It is also worth noting that the narrow distributions of bioparticles comprise both single molecules (e.g. IgG, and BSA) as well as whole viruses (PP7, PR772, TMV). However, despite the remarkably narrow distribution of TMV ($\sigma_{r,Zp,exp}$) and consistency of mobility measured over a long period of time as shown in the Section 2.3.2, I suggest that it be used with an understanding of its length variation in solution and folded state after electrospray.[96]

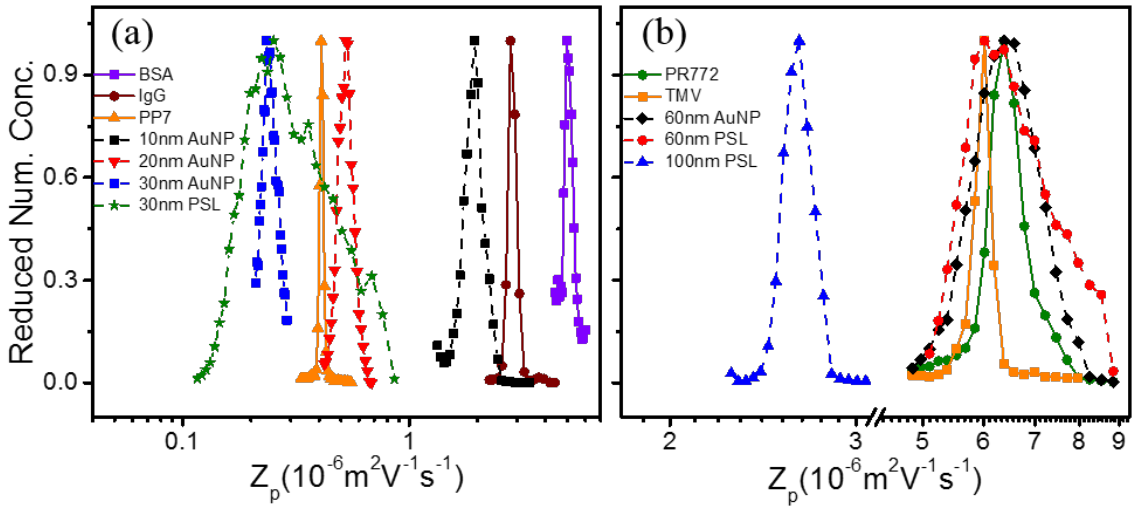

Figure 2.1 *The comparison of mobility distribution between smaller bio-nanoparticles (a) and largger bio-nanoparticles (b) with engineered nanoparticles with comparable*

Evaluation of Instrumental Resolution Limit To assess if the observed size distributions reflect the intrinsic property of the particles or the resolution limit of the DMA, I evaluated the transfer function. The transfer function of the DMA is defined as the probability of an aerosol particle with a certain size that enters at the inlet slit and exits via the sampling slit.[97] As a good approximation, the transfer function including Brownian diffusion of the aerosol reflects the instrumental resolution limit. I calculated the transfer function according to Stolzenburg's approach[52] and found that the peak value of the transfer function decreases, and the function broadens as particle mobility increases under the same experimental setup, as described in the literature.[98] For comparison with the experimental $N_r(Z_p)$ I normalize the DMA's diffusive transfer function to the peak value, and compare them with corresponding $N_r(Z_p)$ of bio-nanoparticles in Fig. 2.2. I also present the reduced standard deviations

of the

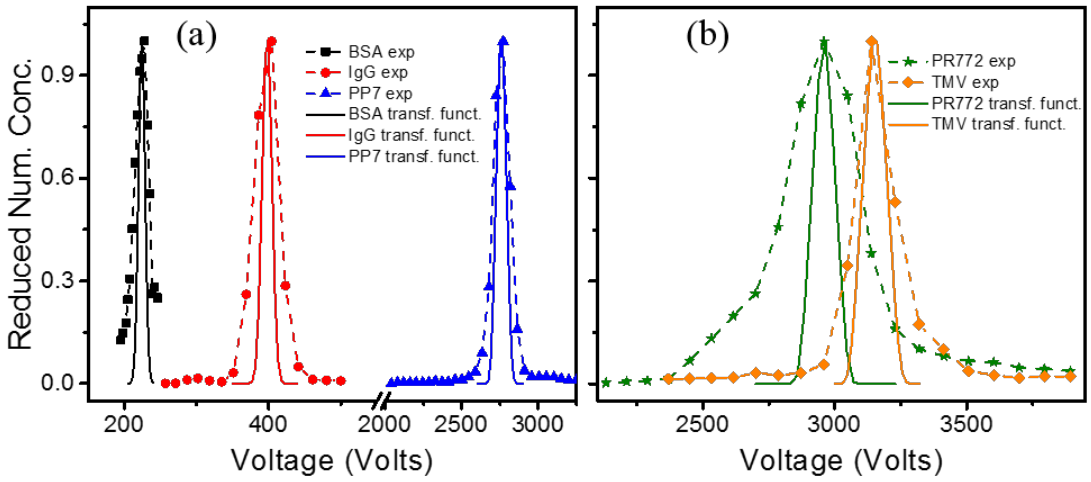

Figure 2.2 *Comparison of experimental size distribution with the corresponding diffusive transfer function normalized to the maximum value.*

transfer function in mobility, $\sigma_{r,Zp,tranf}$, and that for mobility size, $\sigma_{r,Dp,tranf}$, of all bio-nanoparticles in Table 2.2 for comparison. The distributions of the proteins, BSA and IgG, show standard deviation of $N_r(Z_p)$ that are about 2.4 times that of the respective transfer functions. The PP7 and TMV, which are both viruses, show standard deviations even closer to that of the transfer function. The PR772 virus showed a relatively wide distribution, 2.9 times larger than its transfer function. These results show that the bio-nanoparticles are mono-dispersed with the measured $N_r(Z_p)$ less than three times wider than the corresponding transfer function.

Calculation of Corrected Width of Bio-nanoparticle Distribution As Knutson and Whitby's derivation[97] in 1975 shows, the number of particles, $N(V)$, measured at the outlet of the DMA at voltage V is the integral over the product of the DMA transfer function Ω, and the mobility distribution $F(Z_p)$, as shown in Eq. 2.4 below

$$N(V) = \int_0^\infty \Omega(Z_p, V) F(Z_p) dZ_p, \quad (2.4)$$

Table 2.2 *Standard deviation of the corrected mobility distribution and that of corresponding size distribution of bio-nanoparticles.*[a]

	Z_p (10^{-8} $m^2V^{-1}s^{-1}$)	$\sigma_{r,Zp,exp}$	$\sigma_{r,Zp,tranf}$	$\sigma_{r,Zp,F(Zp)}$	D_p (nm)	$\sigma_{r,Dp,exp}$	$\sigma_{r,Dp,tranf}$	$\sigma_{r,Dp,F(Zp)}$
BSA	465.9	0.047	0.020	0.041	6.80	0.023	0.011	0.015
IgG	261.2	0.043	0.017	0.037	9.11	0.019	0.008	0.012
PP7	36.99	0.020	0.012	0.016	24.58	0.009	0.006	0.008
PR772	6.41	0.046	0.016	0.042	61.64	0.025	0.008	0.023
TMV	6.09	0.021	0.014	0.017	63.38	0.012	0.008	0.009

[a]As for smaller bioparticles, i.e. BSA, IgG and PP7, measurements were carried out with sheath flow of 30 L min^{-1} while the bigger ones, PR772 and TMV, were measured with sheath flow of 5 L min^{-1}.

In most cases the distribution of aerosols $F(Z_p)$ is broad relative to the transfer function $\Omega(Z_p, V)$. Hence the standard approximation[97] is to treat $F(Z_p)$ as a constant value for the integration of the transfer function, in which case $F(Z_p)$ is proportional to the empirical $N_r(Z_p)$ in Fig. 2.1. However, this is clearly not the case for bio-nanoparticles. Due to their very narrow distribution, such an approximation could result in an overestimation of the true width of the distribution of bio-nanoparticles.

Here I present a numerical method to evaluate the width of the bio-nanoparticle distribution $F(Z_p)$. Assuming $F(Z_p)$ to be Gaussian distributed with a standard deviation of $\sigma_{F(Zp)}$, a spectral particle count as a function of voltage can be calculated using Eq. 2.5. This numerical result is compared with $N_r(Z_p)$ and the value of $\sigma_{F(Zp)}$ that gives the best fit is considered as the width of the mobility distribution of the bio-nanoparticle. Figure 2.3 shows the numerical results of number spectra for PP7 as an example. The spectral distribution narrows as $\sigma_{F(Zp)}$ decreases. The best fit

spectral distribution to the experimental data is when $\sigma_{F(Zp)}$ is 0.66×10^{-8} m^2 V^{-1} s^{-1}. The mobility distribution $F(Z_p)$ is further converted to a size distribution $G(D_p)$, according to

$$G(D_p) = \frac{F(Z_p)}{p(D_p)}\left|\frac{dZ_p}{dD_p}\right|, \tag{2.5}$$

where $p(D_p)$ is the probability that a particle with diameter D_p carries one elementary unit of charge , and the reduced widths of distribution for bio-nanoparticles are listed in Table **Error! Reference source not found.**2. The ratio of the reduced width of the corrected distribution to the transfer function reduced width is in the range of 1.21 to 2.18 with an average value of 1.69 excluding the value for PR772.

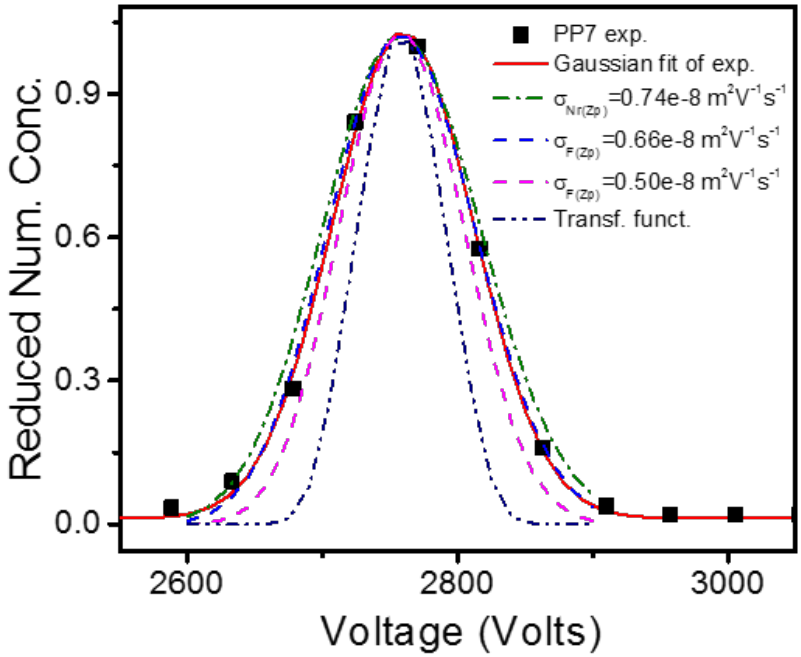

Figure 2.3 *An example of numerical result of normalized number distribution as a function of voltage for PP7 with various widths. The best fit to the experimental data is for* $\sigma_{F(Zp)} = 0.66\times10^{-8}\ m^2\ V^{-1}\ s^{-1}$. *The transfer function is also plotted for comparison.*

Notice that the width of corrected distribution $F(Z_p)$ is not as small as expected: less than 20% smaller than the width of measured distribution, the distribution proportional to the first order approximation of $F(Z_p)$, but still about two times bigger than that of transfer function. This could also be explained by the possibility of differential residual water or impurities retained on bio-nanoparticles which leads to a broader distribution. Although nonvolatile impurities attachment was ruled out by A. Maiβer's study, possibilities of differential amounts of residual solvent or a volatile adduct cannot be eliminated, and they could attribute to the broad distributions[85]. A second possibility could be the conformation of bio-nanoparticles altered when introducing to gas phase [85,99,100]. Compaction of proteins and viruses was found after electrospraying. [85,96,101] Non-ideal instrument performance of DMA could be another factor that attributes to the broad distribution (thereby reducing its resolving power). However, A. Maiβer et al. argued that the influence from instrumentation can be ruled out based on the similar observation as Kaufman's using different DMA.[85]

2.3.2 Stability of Bio-nanoparticle

When ammonium acetate buffer is used to dissolve bio-nanoparticle, ammonium cations could pair with acidic functional groups, and acetate anion could pair with basic functional groups in the protein.[102] As a result the concentration of ions in the buffer could be a potential factor that affects the size of bio-nanoparticle. All results in Table 2.3, 2.4 and 2.5 are shown with mobility and diameter of bio-nanoparticles as well as the standard deviation of the multiple measurements. Results in Table 2.3 suggest that the molar concentration of buffer has at most only a minimal effect on

the resulting absolute mobility size. The effect of dilution, which should primarily affect the salt coating thickness on the particles after electrospray as seen in Table 2.4, shows a negligible effect.

Table 2.3 *Mobility and mobility size of bio-nanoparticles with various molarity of ammonium acetate.*

	20 mM AmAc		10 mM AmAc		2 mM AmAc	
	Z_p (10^{-8} $m^2V^{-1}s^{-1}$)	D_p (nm)	Z_p (10^{-8} $m^2V^{-1}s^{-1}$)	D_p (nm)	Z_p (10^{-8} $m^2V^{-1}s^{-1}$)	D_p (nm)
BSA	464.19±1.98	6.81±0.02	457.48±1.34	6.86±0.01	436.07±1.01	7.03±0.01
IgG	260.65±0.71	9.11±0.01	260.52±0.62	9.11±0.01	251.18±0.31	9.28±0.01
PP7	36.99±0.03	24.58±0.01	37.18±0.02	24.51±0.01	36.75±0.03	24.66±0.01
PR772	6.42±0.01	61.65±0.01	6.44±0.01	61.55±0.02	6.40±0.01	61.74±0.05
TMV	6.10±0.01	63.36±0.03	6.10±0.02	63.36±0.11	6.11±0.01	63.30±0.06

Table 2.4 *Mobility size of bio-nanoparticles depending on thef dilution factor.*

	1 x		5 x		10 x	
	Z_p (10^{-8} $m^2V^{-1}s^{-1}$)	D_p (nm)	Z_p (10^{-8} $m^2V^{-1}s^{-1}$)	D_p (nm)	Z_p (10^{-8} $m^2V^{-1}s^{-1}$)	D_p (nm)
BSA	466.84±0.97	6.79±0.01	464.19±1.98	6.81±0.02	467.89±2.03	6.86±0.02
IgG	258.09±0.89	9.15±0.02	260.52±0.62	9.11±0.01	261.13±0.40	9.10±0.01
PP7	36.99±0.03	24.58±0.01	37.00±0.06	24.57±0.02	37.04±0.03	24.56±0.01
PR772	6.42±0.01	61.65±0.01	6.41±0.01	61.66±0.03	6.43±0.01	61.57±0.02
TMV	6.11±0.01	63.30±0.06	6.13±0.01	63.21±0.01	6.13±0.01	63.19±0.02

Finally, I investigated long term stability, which was assessed at one day, one week, and four weeks after the sample preparation. All samples were stored at 4°C. As shown in Table 2.5, no significant day to day variation was observed in the mobility sizes, indicating that temporal degradation of the investigated bio-nanoparticles are

negligible for at least 4 weeks. However, previous study of PR772 shows evidence of disintegration of the capsids after 11 weeks[91], which indicates PR772 is not a good candidate reference material for a long term use.

Table 2.5 *Day to day variation of mobility size of bio-nanoparticles.*

	First Day		One week after		Four weeks after	
	Z_p (10^{-8} $m^2V^{-1}s^{-1}$)	D_p (nm)	Z_p (10^{-8} $m^2V^{-1}s^{-1}$)	D_p (nm)	Z_p (10^{-8} $m^2V^{-1}s^{-1}$)	D_p (nm)
BSA	467.52±1.00	6.78±0.01	466.84±0.97	6.79±0.01	468.91±0.21	6.77±0.02
IgG	259.12±0.37	9.13±0.01	258.09±0.89	9.15±0.02	257.38±0.20	9.16±0.01
PP7	37.28±0.02	24.46±0.01	36.99±0.03	24.58±0.01	37.23±0.04	24.50±0.01
PR772	6.41±0.01	61.69±0.04	6.42±0.01	61.65±0.01	6.40±0.01	61.74±0.15
TMV	6.04±0.05	63.71±0.06	6.11±0.01	63.30±0.06	6.10±0.01	63.34±0.02

I noticed that our result for BSA is about 12 % lower than the measurement from A. Maiβer et al. and, hence, resulted into a larger inferred mobility size. A larger value was also obtained by Kaddis et al. and Bacher et al.. Also I obtained a narrower distribution for BSA with FWHM (full width at half maximum) of 11.0 % compared to that of 17.6 % from Maiβer. Though Maiβer et al. inferred that the use of commercial nanoDMA (TSI), same as I used here, caused the "anomalously large" mobility size[85], they calibrated their DMA in a different way than I used: Maiβer et al. calibrated their DMA with [tetra-dodecyl ammonium]$^+$ ions, for which the mobility was measured by Ude and F. de la Mora[7], while I used NIST traceable 100 nm size standard SRM1963. In addition, a different batch of BSA was studied here which could be a potential cause of the difference. It remains unresolved whether the discrepancy in mobility arises from the different instrumental performance, the calibration method, variation of samples or other factors.

2.4 Conclusion

In summary, I have measured the size distributions of several proteins and viruses: BSA, IgG, PP7, PR772 and TMV using ES-DMA and compared them with those of colloidal gold and PSL. The width of the size distribution of the bio-nanoparticles is a factor of at least two times smaller than that of the 30 nm and 60 nm PSL spheres and a factor of about two times smaller than the gold nanoparticles. Transfer functions are calculated to show the instrument limits. The experimental results show the empirical spectra of bio-nanoparticles are less than 2.4 times wider than corresponding transfer functions where the worst case is PR772 with a ratio of 2.9 due to a possibility of temporal disintegration. By separating the contribution of diffusive transfer function I also calculated the corrected distribution of the bio-nanoparticles, width of which is 20% less than the empirical distribution. The fact that these corrected distributions are still wider than the transfer functions could result from multiple conformations of bio-nanoparticles due to capillary forces during the droplet evaporation process and from the presence of residual water or other volatile impurities. The non-ideal behavior of the DMA is likely not a significant factor. The TEM images of folded TMV after electrospray support that structure of the bio-nanoparticles could be different as aerosol relative to being in a liquid phase. Stability testing shows the mobility size of the bio-nanoparticles varies little as the buffer molarity or the buffer concentration changes. No significant change of mobility size is observed in the measurements for up to four weeks' time. Thus the bio-nanoparticles could be a promising reference material for mobility size measurement.

Chapter 3: Exploring Aerosol Standards for Optical Absorption Measurement Using a Photoacoustic Spectrometer

3.1 Introduction

Photoacoustic spectroscopy (PA) represents a sensitive optical technique that measures the absorption coefficient *in situ*. Besides application in trace-gas spectroscopy,[62,103,104] PA has also been applied to monitor black carbon content of atmospheric aerosols.[28,105] Compared to routine filter-based techniques, PA measures absorption of aerosols suspended in a flow of carrier gas that is close to their natural state, thus fast gaining acceptance in the aerosol community.[106-108]

The absorption coefficient is the primary quantity measured with a PA instrument. A brief description of this technique is as follows. A stream of aerosols is drawn into an acoustic resonator where they are illuminated by a laser beam. Photon energy is absorbed by particles and converted to thermal energy that heats the bath gas creating a local pressure increase that propagates as a sound wave. Modulation of the light intensity at the resonance acoustic frequency amplifies the propagated sound wave that can be detected by a calibrated microphone. The absolute response of acoustic resonator has been shown to be quantitative with a calculable cell constant.[62] However, to ensure robust PAS measurement, a calibrated source is necessary to calibrate/check the measured absorption.

The calibration of PAS has been performed using high concentrations of absorbing gas, including nitrogen dioxide[107], ozone[108] and oxygen A-band[62]. A gas

calibration accuracy of 1% to 2% was reported by Lack *et. al* using ozone as the calibration source[108]. In contrast to when applied to gaseous absorber, PA when applied to aerosol involves an additional mechanism that the bathgas is heated by an absorber different in phase than the surrounding medium. Since the mechanism of light absorption, internal heating, and subsequent heat transfer to the surrounding, one could in principle never be sure that the observations made by an aerosol calibration relative to a gas phase calibrant. An ideal aerosol standard should be easy to generate, have a reproducible morphology, and with a known optical constant. A spherical shape is preferable since it facilitates selection of size and mass, as well as comparison with theory. One documented aerosol standard is spray dried nigrosine employed by Lack et al., who reported a combined relative uncertainty in absorption coefficient < 5%[108].

In this chapter, I explore online synthesis of nanospheres of fullerene C_{60}, copper and silver. As a novel carbon allotrope, C_{60} has a potential to serve as an absorbing standard for black carbon. Copper and silver were chosen because of well-characterized optical properties of bulk[109-111] and because of controllable structure that can be conveniently synthesized[112,113]. The absorption cross section for size and mass selected particles were measured using PAS at λ = 405 nm and λ = 660 nm, and compared to Mie calculations based on a homogenous sphere model, using refractive indices from literature. Finally, I make recommendations on the PAS calibration standards based on these results.

3.2 Materials & Methods

A schematic of the experimental setup is shown in Fig. 3.1, which consists of aerosol generation and conditioning, classification by mobility size (D_p) and particle mass (m_p) using a differential mobility analyzer (DMA) and an aerosol mass analyzer (APM) respectively, optical absorption measurement of aerosols using a photoacoustic spectrometer (PAS), and finally counting of particle number density employing a condensation particle counter (CPC).

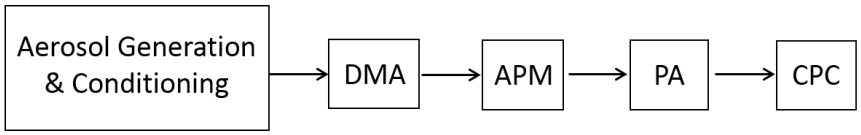

Figure 3.1 *Experimental schematic used for the characterization of aerosol size, mass and optical absorption properties. Abbreviations: differential mobility analyzer (DMA), aerosol particle mass analyzer (APM), photoacoustic spectrometer (PAS) and condensation particle counter (CPC).*

3.2.1 Nanoparticle Generation and Classification

The challenge of particle synthesis is to obtain relatively big nanospheres yet at sufficiently high number concentration to achieve optical signals with reasonable signal to noise ratio. Nanocrystalline C_{60} particles with D_p up to 100 nm can be generated by spay drying a solution of mixed fullerene extract in toluene.[114-116] Gurav et al. reported generation of fullerene nanoparticles via vapor condensation in a continuous flow system starting from C_{60} power[117], which is relatively more convenient in terms of sample preparation. Here I adopted a similar method used by Gurav but with a reduced carrier gas flow rate to enable growth of bigger particles.

Fullerene C_{60} nanoparticles were generated by subliming bulk C_{60} powder (99.9%, MER) at 650 ^{0}C in a tube furnace, with a residence time ≈ 13 s in the heated zone, at a flow rate of 0.9 L min^{-1} of nitrogen. Down-stream supersaturation results in nucleation to form C60 particles. The generated C60 particles has a size distribution located at 239 nm, see SI. To ensure removal of possible volatile impurities, the temperature of the furnaces took one hour to ramp up to the set point and was maintained at the set point for half an hour prior to optical measurements.

Production of copper nanospheres followed the same procedure as in the study of Kim et al. [113] by spray pyrolysis of copper acetate precursor with an ethanol co-solvent. The precursor concentrated at 0.02 mol L^{-1} was prepared by dissolving copper acetate (reagent graded, Sigma Aldrich) in a co-solvent containing 10% volume fraction of ethanol and 90% volume fraction of deionized water, followed by vigorously stirring for 3 hours using a magnetic bar. This copper precursor was atomized with a collision-type atomizer (TSI 3076, 30 psig) using nitrogen gas. The nebulized solution droplets, suspended in nitrogen carrier gas, were sampled with a flowrate of 0.5 L min^{-1} passing through a tube furnace maintained at 650 ^{0}C, where solvent evaporates and precursor particles are decomposed to copper. Trace amounts of hydrogen which come from thermal-decomposition of ethanol helps to generate the zero valent metal[113]. The copper particles are found to have negligible oxygen as determined by X-ray photoelectron spectroscopy analysis. Subsequently aerosols were passed through an active carbon desiccation dryer (TSI 3062), a SiO_2 desiccation dryer (TSI 3062) and a Nafion drying tube (PermaPure MD-700-48F-3) with the counter flow relative humidity (RH) held at <5% to remove any remaining

solvent residue. The same procedures were repeated using a forming gas (5% volume fraction of hydrogen and 95% volume fraction of nitrogen) where the hydrogen could ensure reduction of metal oxides.

A two-furnace system, as described in prior study[112], was adopted here for the production of spherical silver nanoparticles with an aggregation chamber added after the first furnace to increase the number concentration of larger particles. As received granular silver (99.999%, Sigma Aldrich) [118] were heated at 1070 ^{0}C in a ceramic boat inside a tube furnace, enabling evaporation, homogeneous nucleation and condensation to grow silver aggregates. Silver spheres were then created by sintering the aggregates in a second furnace at 600 ^{0}C. A 5L buffer bottle was placed prior to the second furnace to facilitate the growth of silver aggregate which broadens the size distribution of the generated silver spheres and increases the number density for particles with large size (60nm ~ 120nm). Nitrogen was used as carrier gas to prevent oxidation with a flowrate e 3 L min^{-1} which was empirically found to generate the highest silver sphere yield in the size range of 60 nm ~ 120 nm.

Before PA measurement, the particles were subject to size classification (60 nm to 120 nm for silver, 60 to 300 nm for copper and 150 nm to 400 nm for C_{60}) by a differential mobility analyzer (DMA, TSI 3082) using 5L min^{-1} sheath flow and 0.5 L min^{-1} aerosol flow. Since DMA functions by balancing electrostatic and drag forces, which scales with the viscosity and mean free path of the carrier gas, thus actual size would be different from nominal size if carrier gas is not air by default. To compensate this size shift due to carrier gas, I correlated the measured D_p with nominal D_p using NIST-traced size standard polystyrene latex beads of three sizes (60

nm, 100 nm and 150 nm nominally). The actual D_p was consequently extrapolated based upon the D_p read out from the software, see SI. This results in a 2% shift to smaller sizes in nitrogen, and 15% larger for forming gas, than the standard software readout. The particles were then mass- selected using an APM (Kanomax 3061) as described previously [119]. The operational characteristics of the APM are nominally independent of carrier gas.

3.2.2 Optical Absorption Measurement

The PA spectrometer here utilized a resonant acoustic cell that is similar to prior studies [58,62,120]. Optical absorption of aerosols was measured at wavelengths of 405 nm and 660 nm using external-cavity diode lasers which emit up to 160mW and 70mW respectively, monitored by a NIST-traceable calibrated power meter. Prior to the PA cell, the laser beam was intensity modulated using a mechanical chopper in order to couple with the selected resonance frequency of the cell. The aerosol stream passes through the PA cell at a flow rate of 0.5 L min^{-1} with a residence time of 10 s. A calibrated microphone, located at the resonator antinode, detects the acoustic waves converted from the optical energy that is absorbed by the aerosols. A lock-in amplifier (LIA, Stanford Research Systems, model SR830) was employed for phase-sensitive detection allowing for the absorption coefficient α_{Abs} to be calculated from Eq. 1.13. Along with number density N determined from CPC, absorption cross section C_{Abs} can be calculated as

$$C_{Abs} = \frac{\alpha_{Abs}}{N}. \tag{3.1}$$

Utilizing Allance variance test I quantified the detection limit of current PA spectrometer to be 9.6×10^{-8} W m^{-1} for an averaging time of 5 min with a uniform interval of 1 s [58].

For a resonant acoustic cavity, the measured α_{Abs} is proportional to the resonance frequency f_0 which is ~1639 Hz in ambient air at 296 K [62] for the current PA cell, corresponding to the lowest-order mode. Incident laser beam was intensity modulated at a frequency f_m to match the selected f_0 of the acoustic resonator. However, f_0 scales with the speed of sound in the gas, which is a function of gas composition. Such shift in f_0 can alter the amplitude of α_{Abs} if f_m is not adjusted accordingly. Therefore, resonator response at multiple frequencies (f) in the vicinity of f_0 was measured prior to changing working gas in PA cell. Values of f_0 was determined by fitting the resonance response function based upon

$$u + iv = \frac{ifA}{(f_0 + g)^2 - f^2} + B + C(f - \bar{f}) \tag{3.2}$$

with adjusted parameters including resonance frequency f_0, the half width g, the complex amplitude A, and the complex background parameters B and C that account for the tails of other modes, frequency dependence of the transducers, cross talk, etc. The terms u and v represent the real and imaginary component of the acoustic response. Thus modulated frequency f_m of the laser beam was changed accordingly to match f_0 by varying the rotation speed of the mechanical chopper.

3.2.3 TEM Characterization

For electron microscopy characterization, size selected aerosols were electrostatically precipitated onto a TEM grid (200-mesh copper grids coated with

carbon film) using an aerosol sampler (TSI 3089) at -9.5 kV collection voltage, and a sampling flow rate of 0.5 L min^{-1}. The TEM images were collected with a JEOL 2100 at an acceleration voltage of 200 kV, while SEM images were collected with FEI dual beam FIB/SEM at an acceleration voltage of 10 kV.

3.3 Results and Discussion

3.3.1Charaterization of Nanoparticles

Figure 3.2 shows TEM images for size-selected nanospheres of C_{60} (150 nm, Fig. 3.2a), copper (60 nm, Fig. 3.2b) and silver (60 nm, Fig. 3.2d). Both copper and silver nanospheres are dense and near-spherical. Unlike the silver which required a second sintering furnace, the C_{60} generated compact aggregates from a single furnace system. (Fig. 3.2c). A closer look at C_{60} particles reveals crystalline domains with d-spacings corresponding to various face centered cubic lattice planes [121]. The morphology can also be examined by the mass-mobility scaling component D_{fm}, defined as

$$m_p = m_{p,0}\left(\frac{D_m}{D_{m,0}}\right)^{D_{fm}}, \tag{3.3}$$

whose value approaching 3 reveals nearly spherical shape, while significantly smaller than 3 indicates a fractal structure [65,122]. The term $m_{p,0}$ corresponds to the particle mass for an arbitrarily chosen mobility diameter $D_{m,0}$. As shown in Table 3.1, C_{60} particles has D_{fm} slightly smaller than 3 while both silver and copper particles have D_{fm} close to 3, which are consistent with the TEM images. The effective density ρ_{eff}, defined as

$$\rho_{eff} = \frac{6m_p}{\pi D_p^3}, \tag{3.4}$$

was measured as (1.33 ± 0.11) g cm^{-3} for C_{60} particles, implying about 20% void

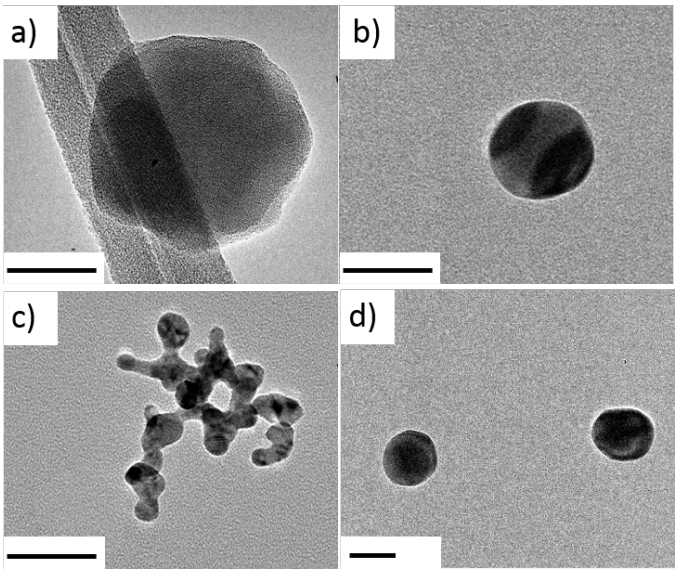

Figure 3.2 *TEM images of a) 150 nm C_{60} spheres, b) 60 nm copper spheres, c) 60 nm silver aggregates collected at the exit of first furnace and d) 60 nm silver spheres collected at the exit of second furnace. The scale bars correspond to 50 nm.*

Table 3.1 *List of mass-mobility scaling component (D_{fm}), effective density (ρ_{eff}) and densities relative to bulk (θ) assuming bulk density (ρ_{bulk}) from literature. Propagated uncertainties are shown along with the mean values.*

	D_{fm}	ρ_{eff} (g cm^{-3})	ρ_{bulk} (g cm^{-3}) [123]	θ
C_{60}	2.79 ± 0.05	1.33 ± 0.11	1.65	0.81
Cu	3.03 ± 0.01	8.08 ± 0.21	8.92	0.91
Ag	2.97 ± 0.03	10.21 ± 0.17	10.49	0.97

space assuming bulk density of (1.65± 0.05) g cm^{-3}.[124] Results are presented using mean value with 2σ uncertainties here and hereinafter. In contrast, ρ_{eff} was measured as (10.21 ± 0.17) g cm^{-3} for silver and (8.08 ± 0.21) g cm^{-3} for copper, respectively.

The densities relative to bulk ($\theta = \rho_{eff}/\rho_{bulk}$) are close to 1 for both metal particles indicating a densely packed morphology.

3.3.2 Validation of PA Absorption

To check if the investigated particle systems are suitable as a calibration source for PAS, it is crucial to quantify how well the optical absorption measured by PAS agrees with documented values. Based upon the characterization stated above, a homogeneous sphere model would be a good approximation for the aerosols generated in this study. The strategy here is to calculate the absorption cross section C_{Abs} using a homogeneous sphere Mie routine [26] by applying documented refractive indices (RI) (or dielectric constants) of bulk for the given material and wavelength. For C_{60} particles, RI was adopted from thin film measurement by Dresselhaus [125]. For metal particles, the refractive indices from Palik [110] and McPeak [111] were chosen as bulk standards due to their widespread use in the plasmonic community. Values are listed in Table 3.2.

Table 3.2 *Refractive index from literature applied in absorption calculation.*

λ (nm)	C_{60}	Cu		Ag	
	Dresselhaus[125]	Palik[110]	McPeak [111]	Palik	McPeak
405 nm	2.4 + *i*0.37	1.18 + *i*2.21	1.108 + *i*2.168	0.173 + *i*2.01	0.045 + *i*2.182
660 nm	1.99 + *i*0.03	0.214 + *i*3.8	0.102 + *i*3.88	--	--

Absorption of C_{60} Figure 3.3 shows the measured C_{Abs} at λ=405 nm and 660 nm for C_{60} nanoparticles that were size and mass selected for D_p ranging from 150nm to 400 nm with corresponding m_p from (2.20 ±0.01) fg and (38.55 ± 0.10) fg reported as

mean and standard deviation of multiple measurements. At both wavelengths, the measured C_{Abs} increases as a function of D_p and the C_{Abs} measured at λ=405 nm is larger than that measured at λ=660 nm over all selected sizes. This agrees with previous findings that absorption of C_{60} is maximized in the ultraviolet.[126] For λ=660 nm, the increase of C_{Abs} as a function of D_p reaches a plateau at around D_p=300 nm, which suggests a transition from a regime where the total volume of the particle interacts with the incident light to a regime at higher D_p where light is significantly attenuated by the particle (volume to surface absorption transition).

Also shown in Fig. 3.3 is the calculated C_{Abs} based upon the homogenous sphere Mie model[26] at λ=405 nm and 660 nm, respectively. Using RI from Dresselhaus[125], the theoretical prediction agrees well with the measured C_{Abs} at λ=405 nm, with more deviation at λ=660 nm, particularly at the larger D_p where the Mie calculation is up to 30% low. I believe this discrepancy can be attributed to the open structures on the surface of the synthesized C_{60} that allows more of the radiant penetrating the sphere, and therefore more absorption in measurement compared to the calculation for particles with same D_p. To address this the RI was recalculated using Maxwell-Garnett mixing rule based upon our measured packing density (see Table 3.1) to account for the void fraction in C_{60} particles, yielding (2.306±0.075) + i(0.351±0.032) and (1.876±0.047) + i(0.047±0.005) for λ=405 nm and λ=660 nm, respectively. The difference in particle morphology compared to the film structure in the literature may contribute to the deviation of imaginary part of RI at 405 nm. This approach leads to no change in the 405 nm case, but elevates the computed cross section to be in much better agreement with the experiment.

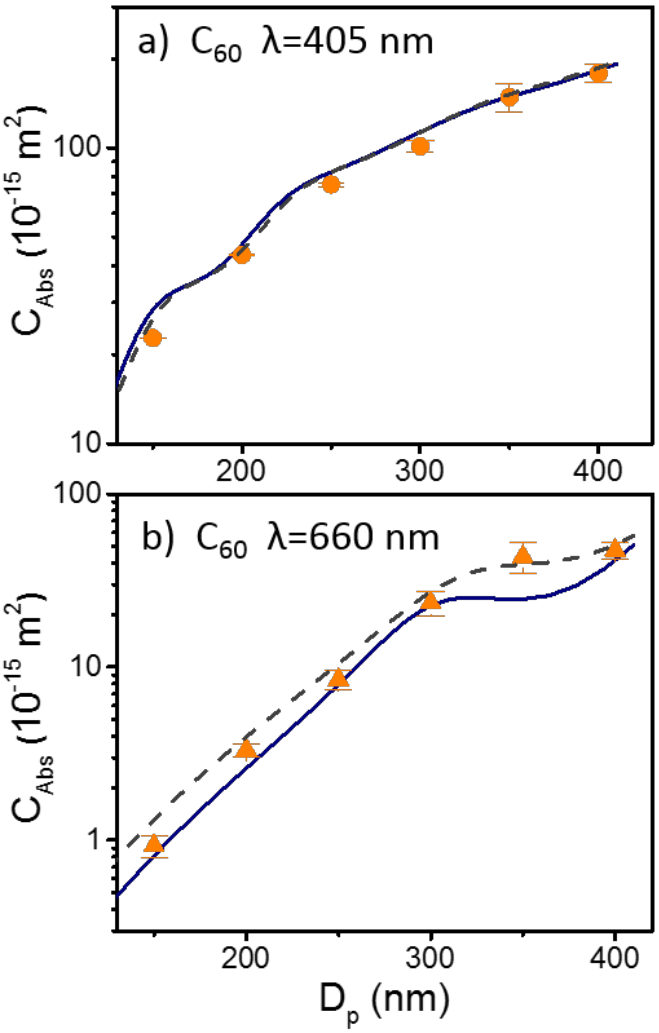

Figure 3.3 *Absorption cross section C_{Abs} as a function of particle mobility size D_p for C_{60} at a) λ=405 nm and at b) λ=660 nm. Results are reported as experimental mean and 2σ uncertainty propagated across all measurements. Navy solid lines represent Mie calculation using refractive index from Dresselhaus [125], while gray dashed lines correspond to Mie calculation using refractive index retrieved using Maxwell-Garnett mixing rule based upon measured packing density (See Table 3.1).*

Absorption of Metal Particles The metal particles (Cu and Ag) as I have shown above are approximately spherical, and thus I expect good agreement with Mie

calculation. However, the outcome is complicated due to various factors that I will discuss below.

Figure 3.4 shows the measured C_{Abs} for Cu particles as a function of selected D_p from 60 nm to 300 nm, corresponding to a selected mass of (0.81±0.02) fg to (100.86±0.82) fg, and exhibits an increasing trend both at λ=405 nm and λ=660 nm. A volume to surface absorption transition is evident in the semi-logarithm plot (Fig. 3.4a, Fig. 3.4b) where C_{Abs} scales linearly with size in the regions where $D_p < \sim 100$ nm and where $D_p > \sim 100$ nm, while the slope is larger in the former than in the latter. Mie calculations using two documented RIs shows negligible difference between each other at λ=405 nm, while the RI from Palik yields a C_{Abs} two times higher than the RI from McPeak at 660 nm.

One concern is that while the particles are nominally spherical, there is deviation from sphericity. I find that generating particles at lower temperature 450 ^{0}C yields copper particles that are rougher and less spherical. This change of morphology gives rise to a 20% increase in C_{Abs} at both wavelengths, see Appendix A. Another issue to consider is that copper is a plasmonic metals with an absorption maximum located at around 700nm.[127] Standard thin film methods, e.g. elliptical polarization [111], reflectance or/and transmission measurements [128], retrieved RI that is highly sensitive to the surface roughness and grain size of these thin films[111]. Prior studies with films of various quality have demonstrated a broad range of retrieved imaginary part of RIs for Cu and Ag in the visible wavelengths[110,111,129]. This morphology impact should become pronounced at wavelengths close to the plasmon

resonance peak, consistent with our observation that significant discrepancy is seen at 660 nm, but good agreement at 405 nm away from the resonance peak.

The discrepancy is even more pronounced for silver, which is also a well-known plasmonic metal exhibiting a sharp and strong absorption peak around 390 nm.[130,131] The PAS measurements for silver were taken only at 405 nm, due to the lower laser power at 660 nm together with the smaller cross section. Unfortunately, 405 nm is near the resonance. The measured C_{Abs} decreases slowly as D_p approaches to 80 nm and scales with D_p linearly afterwards, while Mie calculations demonstrate significant differences from the PA measurement by peaking around 80 nm. I repeated the experiment by generating Ag particles in nitrogen mixed with 5% volume fraction of hydrogen, which acts as a reducing agent, but the measured C_{Abs} differs from calculation in a similar way as that of particle synthesized in nitrogen, see Fig. 3.4c.

I believe that the results for both metals clearly indicate that measurements made near the resonance, will lead to significant error, both because this range is where absorption is highly size-sensitive and because morphology or asymmetry effects on absorption is magnified near the resonance condition. It is concluded that when considering metals as calibration source for PAS absorption measurement, great care must be taken in wavelength choice to avoid the regime where plasmon resonance is expected.

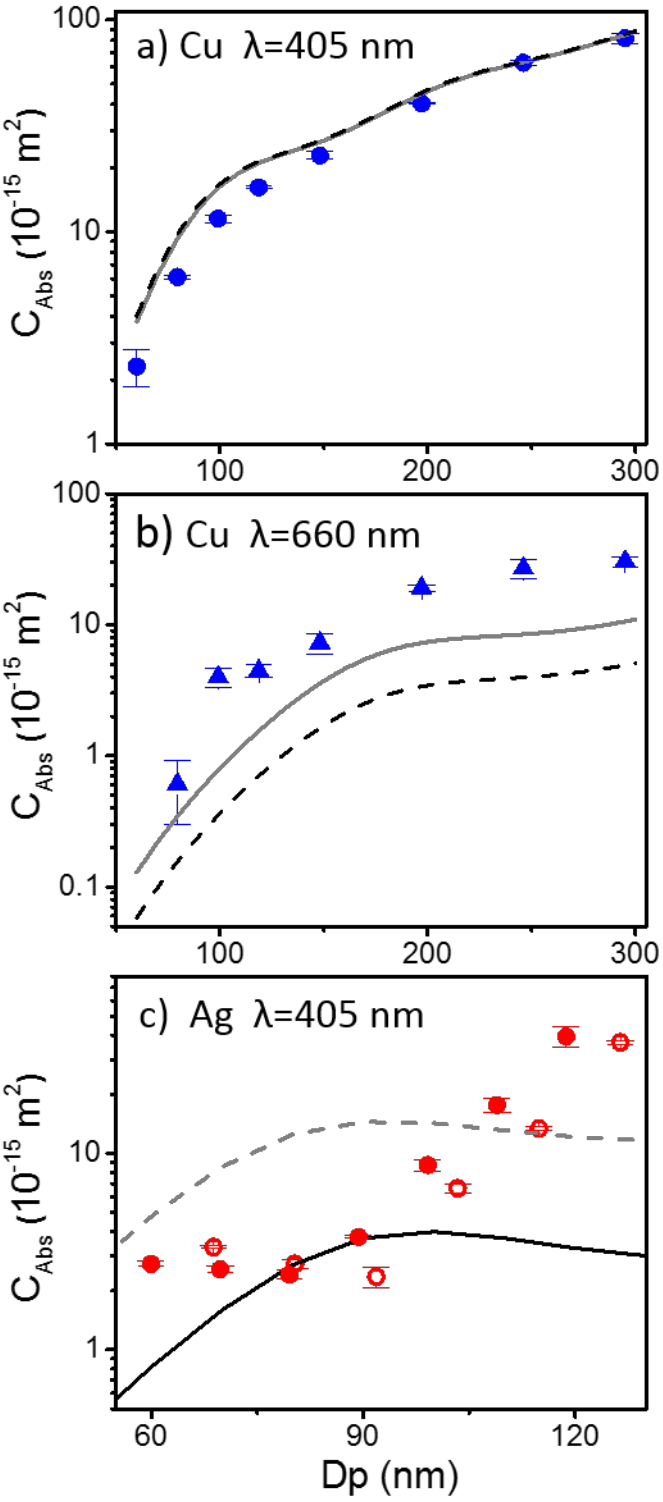

Figure 3.4 *Absorption cross section C_{Abs} as a function of particle mobility size D_p for a) copper nanospheres at λ=405 nm and b) λ=660 nm, and c) silver nanospheres at*

λ=405 nm. Solid symbols correspond to measurements using nitrogen as carrier gas, while open symbols are the measurement using forming gas (5% volume fraction of hydrogen and 95% volume fraction of nitrogen). Results are reported as experimental mean and 2σ uncertainty propagated across all measurements. Mie calculations are also shown using refractive index from Palik [110] (solid gray lines) and McPeak [111] (dashed black lines), respectively.

3.4 Conclusion

In conclusion various aerosols candidates were explored for the purpose of calibrating optical measurement for photoacoustic spectrometer (PA). It has been demonstrated that compact nanospheres of silver, copper and fullerene C_{60} can be generated via aerosol routes with equivalent density close to bulk. Particle size studied here ranges from 60 nm to 300 nm with corresponding mass spanning two orders of magnitude. To demonstrate the feasibility of investigated particles as PA calibration standards, Mie calculations based upon homogeneous sphere model were used to validate the PA measurements. In the case of C_{60}, measured absorption cross section C_{Abs} agrees well with Mie calculation at λ=405 nm and at λ=660 nm. In the case of metal particles, measured C_{Abs} is close to the calculated value for copper at λ=405 nm, but differs greatly for copper at λ=660 nm and for silver at λ=405 nm. It is proposed that the uncertainty in the refractive index in the vicinity of of the plasmonic resonance together with sensitivity of of slight deviations from a homogeneous sphere contribute to the large difference between PA measurement and Mie calculation. Readers are therefore advised to select aerosol standards for PA

measurement taking into account the wavelength where the plasmonic resonance would occur.

Chaper 4: Measured Wavelength-Dependent Absorption Enhancement of Internally Mixed Black Carbon with Absorbing and Non-absorbing Materials

4.1 Introduction

Black carbon (BC) is produced from the incomplete combustion of biomass and fossil fuels, and consists of layered graphitic carbon monomers 20 nm to 40 nm in diameter[132] that are aggregated into more complex structures that strongly absorb light across the visible spectrum.[133] It has been estimated that BC is the second largest contributor to global warming after CO_2.[134] BC aggregates are often internally and/or externally mixed with other species (sulfate, nitrates, carbonaceous organics, etc.).[135-143] The resulting particle morphology, referred to here as the mixing state, can have BC surface bound, or partially- or fully-embedded (engulfed) with BC either centrally (concentric) or off-centrally (eccentric) located within the particle.[139,144]

Changes to the per particle absorption strength (i.e. absorption cross section) and spectral shape when other atmospheric components coat, embed in or mix with BC have drawn significant attention[27,145-147] as absorption is typically enhanced beyond the bare particle case. Consistent with previous investigations,[17,20,22] I define the wavelength dependent absorption enhancement factor ($E_{Abs,\lambda}$) as the ratio of the absorption cross section (C_{Abs}) of the embedded particle ($C_{Abs,embed\ BC,\lambda}$) to that of the bare BC particle ($C_{Abs,BC,\lambda}$)

$$E_{Abs,\lambda} = \frac{C_{Abs,embed\ BC,\lambda}}{C_{Abs,BC,\lambda}}, \tag{4.1}$$

where C_{Abs} is defined as

$$C_{Abs} = \frac{\alpha_{Abs}}{N}, \quad (4.2)$$

and N is the number concentration of particles. The quantity α_{Abs} represents the absorption coefficient and is the fractional loss in light intensity due to absorption per unit propagation distance.

Considering the size of particles and the thickness of embedding material relevant in the atmosphere (i.e. comparable to or smaller than the wavelength of light), absorption enhancement arises from the gradual step-wise refractive index change between the medium (air), embedding material and the absorbing material (BC in most cases); i.e. the embedding material facilitates improved refractive index matching between the medium and absorbing material thereby behaving similar to an antireflective coating.[148] The observed enhancement is strongly dependent upon the size and absorption strength of the absorbing material, embedding thickness and embedding material. Previous investigations have referred to this refractive index matching as lensing whereby the embedding material focuses light towards the absorbing core.[27,149,150] I note that while lensing may be an appropriate descriptor in the geometric optics regime (particles much larger than the wavelength of light) it is not appropriate to use at these sizes.

For an absorbing core comprosed of 10 nm aggregates embedded in a 1 μm non-absorbing shell the $E_{Abs,\lambda}$ can be greater than 10. However, for atmospherically relevant particles, the $E_{Abs,\lambda}$ is more modest and ranges between 1.5 and 1.9 for particles with shell diameters that are less than 1.6 times larger than the core diameter.[145] Ambient measurements show that the $E_{Abs,\lambda}$ of BC can be up to 2.4.[28,142,151-155] The discrepancy between field measurements and theoretical

calculations of internally mixed, embedded particles can be computationally reduced with the consideration of an eccentrically-located single BC core in an internally mixed embedded particle or by the application of discrete dipole approximation method (DDA) or multiple sphere T-matrix method (MSTM) to account for the complex aggregate morphology and the interaction between spherules.[156-158] Moreover, it has been shown computationally that the mixing state of BC has a great impact on the absorption enhancement factor.[159] In contrast to the ambient field-based observations, laboratory measurements tend to coincide more closely to $E_{Abs,\lambda}$ predicted by the concentric sphere model.[28,160-162] Previous laboratory studies have concentrated on BC embedded in materials generated from the ozonolysis products from α-pinene,[163] glycerol and oleic acid,[161] and dioctyl sebacate,[28] and can produce a BC core embedded in an organic shell (core-shell model). These investigations observed that the current theory based upon core-shell model can adequately capture the measurement, but are limited in relevance to particles observed in many field studies.[164] Further, in ambient studies the embedding material must be physically removed to measure the absorption by the BC core. Removal of the embedding material is typically done by volatilization, although the efficacy of removal remains questionable.[154,165] To our knowledge, however, no laboratory study has been reported on the absorption enhancement of heterogeneous BC particles with different mixing states in a controlled manner.

In addition to $E_{Abs,\lambda}$, spectral shape can be affected by particle mixing state. The absorption spectral dependence is commonly described by the absorption Ångström exponent (*AAE*):

$$C_{Abs,\lambda} = C_{Abs,0}\left(\frac{\lambda}{\lambda_0}\right)^{-AAE}, \quad (4.3)$$

where $C_{Abs,\lambda}$ is the absorption cross section at wavelength λ. The terms $C_{Abs,0}$, and λ_0 have been included as the values for a reference wavelength; presently, λ_0 = 550 nm for comparison to prior work. The *AAE* for BC is typically quoted as being near unity and assumes a wavelength independent refractive index for particles < 40 nm in diameter.[166] Recent modeling has shown that BC cores embedded within a non-absorbing matrix (50 nm embedding in a 300 nm BC core) can increase the *AAE* from an initial value of 1.3 up to 1.6.[27] BC can also be mixed or embedded with weakly absorbing carbonaceous materials derived from combustion of biomass and biofuels, termed brown carbon (BrC). BrC is typically quoted as having *AAE* values ranging from 1.5 to ≈ 7.0.[153,160,167-174] Additional experimental studies are required to fully understand the impact of BC embedded within BrC.

Direct *in-situ* absorption measurements can be made using a photoacoustic spectrometer. Ideally, absorption measurements at many points spanning the visible portion of the spectral window would be collected to elucidate the wavelength dependence of embedded BC. In practice, four or fewer wavelengths are typically used as a sufficiently intense source (e.g. laser) is necessary to generate a measurable acoustic signal; further, the use of multiple sources may require the use of multiple acoustic resonators and data acquisition systems. It is possible to equip a photoacoustic spectrometer with a broad-band source such as an optical parametrical oscillator,[175] a Hg arc lamp[176] or supercontinuum laser[58,177] to acquire step-scanned absorption spectra. In the present study 7 points were used to comprise a spectrum,

although only two wavelengths are required to fit Eq. 4.3, which is approach used extensively in prior studies.[178-181]

The discrepancy between ambient field-based measurements and computational-based predictions of absorption for spherical systems of BC in different mixing states requires measurements of well-characterized laboratory-based aerosol. This investigation describes absorption measurements of BC mixed with non-absorbing materials (ammonium sulfate and sodium chloride) and a weakly absorbing BrC surrogate, humic acid (HA); all of which are atmospherically relevant species. The mass mixing ratio (χ_{BC}) defined as the ratio of BC mass to the mass of the total mixture, was chosen as 0.13, similar to particles collected in the terrestrial atmosphere.[144] The absorption spectra were measured using a photoacoustic spectrometer coupled to a supercontinuum light source with a tunable wavelength and bandwidth filter. The measured data as a function of embedding material and mixing state were compared to E_{Abs} calculated using the T-matrix method.

4.2 Materials & Methods

The experimental setup is very much like the one used in Chapter 3, schematic of which is shown in Fig. 3.1. Aerosols were generated and conditioned before being passed to a differential mobility analyzer (DMA) and an aerosol particle mass analyzer (APM) to select the mobility diameter (D_p) and mass (m_p), respectively. Optical absorption was measured by a photoacoustic spectrometer (PA) that utilizes a supercontinuum laser as its light source. A condensation particle counter (CPC) was situated downstream to measure aerosol number density. Using both mobility and mass selection facilitates isolation and selection of particles bearing a +1 charge. Care

was used to ensure that only +1 particles were selected by measuring particle extinction as function of m_p as previously described in Radney and Zangmeister (2016).[182]

4.2.1 Aerosol Generation and Morphology Characterization

BC was generated from Cab-O-Jet 200 (Cabot Corp., 20.03 weight percent solids), a material generated from the combustion of organic fuel stock.[183] This material was chosen for its water solubility and its spectroscopic and morphological similarities to aged BC (See discussions in Results section). Cab-O-Jet in solution consists of dispersed aggregates with monomers ≈ 30 nm in diameter as evidenced by transmission electron microscopy (TEM) images (see Fig. B1). Atomization of a Cab-O-Jet solution produces water droplets containing multiple monomers. Upon drying, the monomers combine and collapse into a structure that appears similar to collapsed BC observed in the terrestrial atmosphere.[184,185]

A BrC surrogate (AAE > 4) consisting of humic acids (HA) was prepared from Ful-Humix (Faust BioAg Inc., 50 weight percent humic acids) by dissolving 500 mg in 15 mL of DI H_2O. The solution was centrifuged for 30 min, the supernatant was decanted and collected, and centrifuged for an additional 30 min. The supernatant was again collected, combined and subsequently filtered to remove any residual solids. The filtered solution was then air dried. The density of the HA was measured in bulk (mass per unit volume) and calculated as the average effective density from the mass-mobility scaling relationship (See discussion in Sec. 4.3 and Appendix B.4). From the residual dried solid material, a stock solution of 5 mg mL^{-1} was prepared for absorption measurements. The non-absorbing materials, ammonium

sulfate (AS, Sigma Aldrich) and sodium chloride (NaCl, Sigma Aldrich) were used as received and stock solutions of 5 mg mL^{-1} were prepared.

To mimic BC containing aerosol measured in Mexico City aerosol plumes,[144] internally mixed particles were produced by co-atomization of a single aqueous solution containing both BC and either AS, NaCl or HA at a 0.13 BC mass fraction (χ_{BC}) in a liquid jet cross flow atomizer (TSI 3076, 30 psig); BC volume fractions were 0.12, 0.15 and 0.11 for the AS/BC, NaCl/BC and HA/BC particles, respectively. At this pressure, ≈ 2.2 L min^{-1} of flow is generated by the atomizer of which ≈ 0.5 L min^{-1} was sampled and the remainder directed to a laboratory exhaust. Both Cab-O-Jet (BC) and HA required extensive drying due to their hygroscopic nature and an extra effort was made to remove particle-bound water in order to avoid additional absorption enhancement[58] or potential photoacoustic response dampening[186-189] from water adsorption. After atomization, aerosols were passed through two SiO_2 desiccation dryers (TSI 3062) and a Nafion drying tube (PermaPure MD-700-48F-3) with the counter flow relative humidity (RH) held at < 5 %. After drying, particles were size selected by a DMA (TSI 3082) using 5 L min^{-1} sheath flow and 0.5 L min^{-1} aerosol flow. The particles were then mass-selected using an APM as described previously.[58]

For TEM measurements, particles were collected using an electrostatic aerosol precipitator (TSI 3089) on TEM grids (200-mesh copper grids embedded with lacey carbon film) at -9.3 kV collection voltage. The morphology and mixing states of the BC particles were imaged using a JEOL 2100 TEM at an accelerating voltage of 200 kV.

4.2.2 Optical Measurements

Aerosol optical absorption spectra were measured using a PA spectrometer as described in Radney and Zangmeister (2015),[58] which can operate across a range spanning from visible to near IR (λ = 550 nm to 840 nm) using a supercontinuum laser (NKT Photonics SuperK Extreme EXR-15) and tunable wavelength and bandpass filter (NKT Photonics SuperK Varia). The particles were illuminated by an intensity modulated laser (via a mechanical chopper) at the resonant frequency of the acoustic cavity (≈ 1640 Hz at 296 K in ambient air).[63] Absorbed optical energy is thermally re-emitted generating a standing pressure wave (i.e. sound wave) at the modulation frequency that was measured by a calibrated microphone located at the resonator antinode, as described previously.[58] A lock-in amplifier (Stanford Research Systems, SR830) was employed for phase-sensitive detection allowing for the absorption coefficients to be calculated from Eq. 1.13.

4.2.3 Modeling BC Optical Properties

The optical properties of bare BC and BC mixed with other components were modeled using the multiple-sphere superposition T-matrix method.[190] BC aggregates were constructed using a diffusion-limited aggregation algorithm[191] as described in Appendix B. Calculated absorption of BC mixed with other species (i.e. AS, NaCl & BrC) assumed BC possessed a similar morphology to bare BC, except that the number of monomers was scaled relative to the mass ratio (0.13 mass ratio). Two cases were investigated, fully- and partially-embedded where either: 1) a single host sphere was used with the diameter identical to the D_p selected by the DMA, with the BC aggregate's center of mass overlapping that of the host sphere, or 2) half of the

monomers in the BC aggregate were moved radially to the outside of the sphere and remained attached, respectively.

4.3 Results

4.3.1 Characterization of Bare BC

Bare BC aerosol had a compact, spherical morphology comprised of 30 nm monomers. TEM images revealed monomers with discontinuous onion-like fringes, consistent with flame-generated soot and indistinguishable from TEM images of aged soot in the atmosphere,[132] see Fig. 4.1a. The measured mass-mobility scaling exponent D_{fm} was 2.83 ± 0.01 consistent with the nearly spherical shape observed in TEM images. The effective density ρ_{eff}, defined as Eq. 3.4, was measured as (0.78 ± 0.05) g cm^{-3} over a D_p range between 100 nm and 300 nm. Figure 4.1b shows the measured C_{Abs} at λ = 600 nm, 700 nm and 800 nm of bare BC as a function of particle mass spanning from 0.47 fg to 10.48 fg; D_p = 100 nm to 300 nm in 50 nm increments. The linearity at each wavelength indicates that the C_{Abs} scales with particle mass (i.e. Rayleigh regime) across the spectral region used in this investigation up to the pure 10.48 fg BC particle. For comparison, the average internally mixed AS/BC and NaCl/BC particles (see below) contained ≈ 1.4 fg and 1.7 fg of BC, respectively. Due to the wide mass range over which C_{Abs} is linear for pure BC particles, I expect the BC portion of the internally mixed particles to behave similarly.

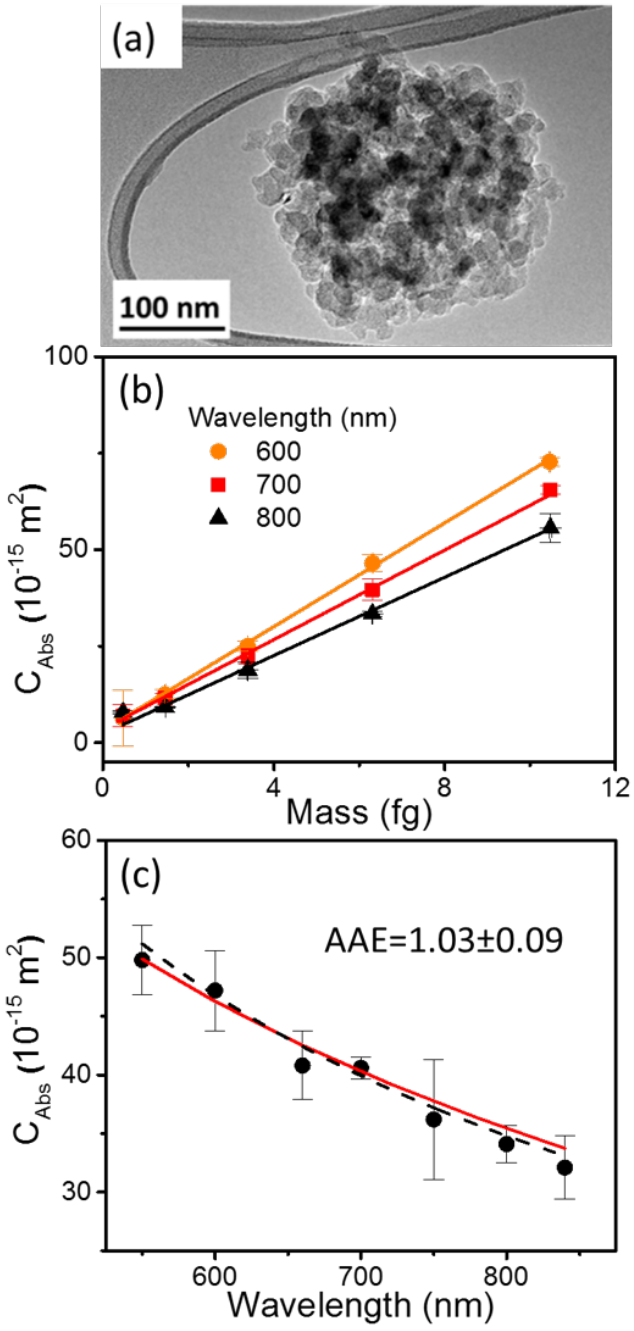

Figure 4.1 *a) TEM image of bare 250 nm BC particles used in study. b) BC absorption cross section (C_{Abs}) as a function of particle mass at λ = 600 nm, 700 nm and 800 nm. c) Absorption spectrum (C_{Abs}) of 250 nm BC from λ = 550 nm to 840 nm. Dashed black line represents AAE fit of the experimental data over full range. Solid red line represents calculated absorption spectrum utilizing T-matrix method*

described in text. Measured results are reported as experimental mean and 2σ uncertainty propagated across all measurements.

A better resolved absorption spectrum ($\Delta\lambda$ = 50 nm) for BC particles with a 250 nm mobility diameter corresponding to a BC mass of 6.3 fg is shown in Fig. 4.1c. Here the data has been plotted as C_{Abs} versus wavelength, instead of C_{Abs} versus mass as in Fig. 4.1b, as absorption depends only upon mass for all measured wavelengths (i.e. linearity of traces in Fig. 4.1b).[192] The *MAC* (defined as C_{Abs}/m_p) at 550 nm is (7.89 ± 0.25) m^2 g^{-1} and the *AAE* is 1.03 ± 0.09 over the measured wavelength range, similar to the average *MAC* and *AAE* for BC reported in prior studies (all reported uncertainties are 2σ).[149,193]

The RI at 660 nm of bare BC was calculated as (1.77 ± 0.02) + i(0.80 ± 0.02), see discussion in Appendix B.3. A broad range of RIs for atmospheric BC are documented in the literature.[194-196] The RI of the bare BC measured in this study is at the upper end of the previously published RI values for atmospheric BC, but similar to other investigations for particles with compact morphology.[149,195] To validate the BC parameters used in subsequent calculations, the absorption spectrum of bare BC was calculated using the T-matrix method[158] using a refractive index of m = 1.77 + i0.80 and an aggregate structure calculated using DLCA with k_0 = 1.2, D_f = 2.83, N_m = 218 and using the calculated BC RI (See Appendix B.3). The BC RI was assumed to be wavelength independent as discussed in Bond and Bergstrom (2006).[149] Using these assumptions, the T-matrix is able to agree well with the measured C_{Abs} and *AAE*, see solid red line in Fig. 4.1c.

4.3.2 Characterization of Embedded BC Mixing State

The absorption spectrum of BC embedded in three atmospherically relevant materials was measured for two non-absorbing materials (AS and NaCl) and a surrogate for brown carbon, HA (i.e. Ångström exponent ≥ 4).[27] BC particles can be embedded with AS and/or other aerosol at a BC mass fraction (χ_{BC}) ≈ 0.1.[144] Particle mixing state and optical properties are influenced by the interaction between BC and the embedding material,[144] drying rate[151] and history.[197]

In the present investigation, TEM images show structural differences for AS/BC, NaCl/BC and HA/BC, as seen in Fig. 4.2, for 250 nm mobility diameter particles. AS/BC and HA/BC formed spherical particles with BC aggregates fully embedded within an AS or HA shell (Fig. 4.2a and 4.2c, respectively). NaCl/BC particles have a cubic NaCl shell with BC aggregates protruding from the particle interior to its periphery (Fig. 4.2b). Further evidence of the particle mixing state was determined by utilizing the electron beam from the TEM to melt and desorb the embedding material and reveal the particle interior, showing the presence of BC aggregates (see Fig. B5 in Appendix B for images showing time series of embedding material melting). For NaCl/BC, aggregates were observed both internal and external to the embedding material.

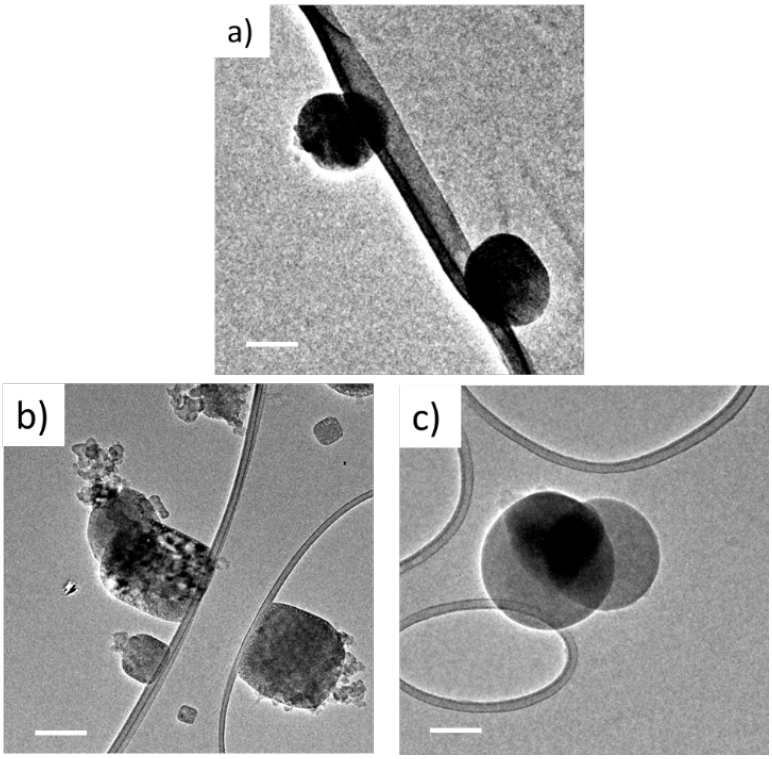

Figure 4.2 *TEM images of 250 nm a) AS/BC, b) NaCl/BC, c) HA/BC. The scale bar corresponds to 100 nm.*

4.3.3 Absorption of BC Embedded in Non-absorbing Materials

Below I focus on how mixing state influences on particle absorption. I first concentrate on the optical properties of BC mixed with non-absorbing materials. Figure 4.3a shows the measured C_{Abs} spectra spanning between λ = 550 nm and 840 nm for particles that were size and mass selected at D_p = 250 nm and m_p = (13.50 ± 0.06) fg and (11.48 ± 0.06) fg for AS and NaCl, respectively with χ_{BC} = 0.13. The absorption cross section is higher for the BC fully embedded in AS versus the BC partially embedded NaCl. The spectra of the embedded particles have higher *AAE*s than bare BC; 1.43 ± 0.05 for AS/BC and 1.34 ± 0.06 for NaCl/BC versus 1.03 ± 0.09 for bare BC. The absorption enhancement of embedded BC (E_{Abs}) is based on Eq. 4.1

with C_{Abs} of the BC core calculated from the particle mass, BC mass fraction and *MAC* of 250 nm particles:

$$E_{Abs,\lambda} = \frac{C_{Abs,embed\ BC,\lambda}}{m_p\ \chi_{BC}\ MAC_{BC,\lambda}}, \tag{4.4}$$

At the shortest wavelengths, E_{Abs} is within 2σ for both the AS/BC and NaCl/BC systems. Towards the long-wave side of the spectrum, E_{Abs} values for both systems differ as NaCl/BC has remained nearly constant and AS/BC has decreased.

Wavelength dependent E_{Abs} have been calculated previously for embedded BC using spherical particle Mie theory,[27] but to our knowledge the AS/BC data represent the first measured spectra showing a wavelength dependent E_{Abs} for embedded BC; the NaCl/BC E_{Abs} is wavelength independent across the measured spectral range. I used the T-matrix method to investigate if the method is able to capture the measured spectral dependence for each embedding material. Calculations were run for fully-embedded and half-embedded BC. The simulated enhancement spectra are shown in Fig. 4.3a for each case where the lower (dashed) and upper (solid) bounds represent the half-embedded and the fully-embedded cases, respectively. The region in between these two values represents mixing states migrating from half-embedded to fully-embedded BC, and assumes the BC aggregate's center of mass overlaps that of the host sphere. Moving BC aggregates off center still within the host sphere results in less than a 3% decrease in absorption cross section, consistent with previous calculations.[26] The corresponding simulated and measured *AAE*s are shown in Table 4.1.

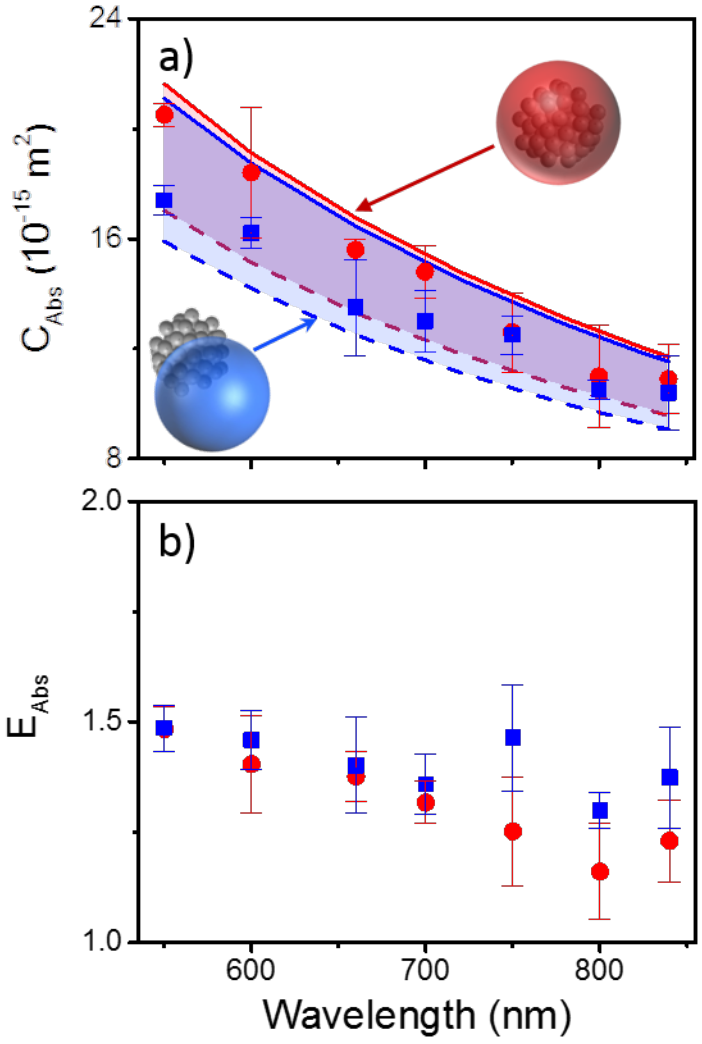

Figure 4.3 *a) Measured absorption cross section (C_{Abs}) spectra of AS/BC (red circles) and NaCl/BC (blue squares) for 250 nm mass selected particles (χ_{BC} = 0.13) from λ = 550 nm to 840 nm. Lines represent fully embedded (solid) and half embedded (dashed) BC for each system; the shaded regions represent mixing states in between these two extremes. b) E_{Abs} for AS/BC (red circles) and NaCl/BC (blue squares). Measured results are reported as experimental mean and 2σ uncertainty propagated across all measurements.*

Table 4.1 *Measured and modeled AAEs for half- and fully-embedded AS/BC and NaCl/BC. Propagated uncertainties are shown along with the fit AAEs.*

	Measured *AAE*	Calculated *AAE*	
		half-embedded	fully-embedded
AS/BC	1.43 ± 0.05	1.36	1.45
NaCl/BC	1.34 ± 0.06	1.32	1.41

4.3.4 Absorption of BC with Absorbing Material

A weakly absorbing BrC surrogate material was isolated from humic acid extracts as described in the Materials & Methods. Upon atomization and drying, pure HA forms spherical particles with an average effective density of (1.5 ± 0.1) g cm^{-3}, as determined from the mass-mobility scaling relationship (D_{fm} = 3.10 ± 0.04). The RI of HA was determined to be (1.58 ± 0.01) + i(0.02 ± 0.01) at λ = 660 nm. For T-matrix calculations, I assumed the real component of RI was invariant with wavelength and the imaginary part of the RI is well described by the absorption spectrum of the material in aqueous solution (see Appendix B3 for HA refractive index determination and aqueous absorption spectrum). The absorption spectrum of HA aerosol is shown in Fig. 4.4a, and exhibits an *AAE* of 5.31 ± 0.14. The *MAC* of HA aerosol was (0.85 ± 0.06) m^2 g^{-1} at 550 nm, nearly an order of magnitude lower than that of BC at the same wavelength, and is comparable to strongly absorbing BrC in prior work.[198]

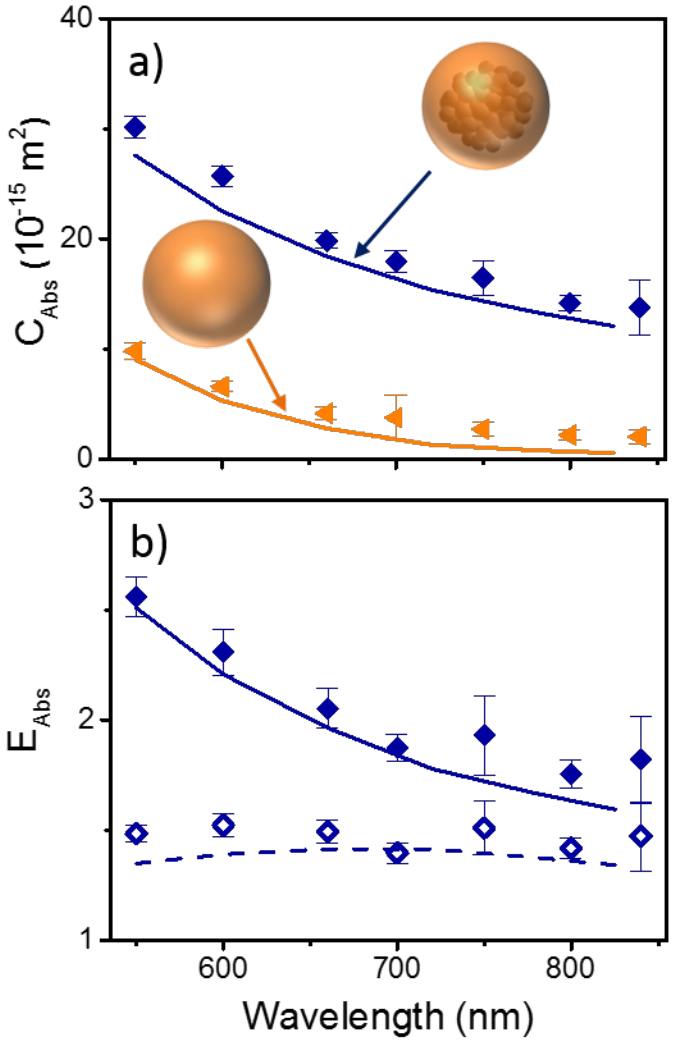

Figure 4.4 *a) Measured absorption cross section (C_{Abs}) spectra of pure HA (gold triangles) and HA/BC (blue diamonds) with χ_{BC} = 0.13 for 250 nm size-mass selected particles from λ = 550 nm to 840 nm. Lines represent calculated C_{Abs} for each system. b) E_{Abs} for HA/BC including HA absorption (solid blue diamonds) and only including enhancement from HA after subtraction HA absorption (open blue diamonds); see Eq. 4.5 in discussion and text. Lines represent calculated E_{Abs} using fully internal mixing model for both definitions. Measured results are reported as experimental mean and 2σ uncertainty propagated across all measurements.*

At a $\chi_{BC} = 0.13$, C_{Abs} increases by a factor of 2 to 3 relative to the pure HA at the same mobility diameter. The *AAE* of BC embedded in HA is 1.91 ± 0.05, lower than that of pure HA but higher than that of BC embedded in AS or NaCl. For modeling I adopted a single sphere model for the pure HA and a fully-embedded model for HA/BC particles, consistent with TEM images of BC embedded in HA. The T-matrix calculated C_{Abs} spectrum agrees well with the experimental results in each case, as shown by the solid lines in Fig. 4.4a.

The $E_{Abs,\lambda}$ of BC embedded in HA was calculated using two methods. Using Eq. 4.1, $E_{Abs,\lambda}$ includes the impact of HA absorption and enhancement of BC absorption. For the second method, the inherent relative contributions to absorption from HA is removed by redefining $E_{Abs,\lambda}$ as

$$E_{Abs-HA,\lambda} = \frac{C_{Abs,embed\ BC,\lambda}}{(1-\chi_{BC})\, m_p\, MAC_{HA,\lambda} + \chi_{BC}\, m_p\, MAC_{BC,\lambda}}, \quad (4.5)$$

where $MAC_{HA,\lambda}$ represents the *MAC* of the pure HA. Note that $E_{Abs\text{-}HA,\lambda}$ when applied to BC embedded in HA, describes the E_{Abs} arising only from BC absorption enhancement and reduces to Eq. 4.4 when applied to the non-absorbing material. Both results are shown in Fig. 4.4b. The $E_{Abs,\lambda}$ shows an increase up to a factor of 3 at the shortest measured wavelengths and is 1.6 in the near-IR. Removing HA absorption from $E_{Abs,\lambda}$ shows that much of the enhancement at short wavelengths is a result of HA absorption as seen by the relatively constant $E_{Abs\text{-}HA,\lambda}$ in Fig. 4.4b. This trend was first predicted in prior calculations using spherical particle Mie theory, where the data are similar in shape and magnitude to 300 nm absorbing core with a weakly absorbing 100 nm thick embedding.[27]

4.4 Discussion

In this investigation the mass mixing ratio and mobility diameter of internally mixed BC and NaCl, AS or HA particles were held constant at χ_{BC} = 0.13 and 250 nm, respectively. The primary variables that differ between the embedding materials are density, refractive index and how each material interacts with BC under the conditions of aerosol generation to form particles (mixing state). Below I highlight how each variable impacts $E_{Abs,\lambda}$ using the simplest case of spherical particles. Due to density differences between the embedding materials, the χ_{BC} corresponds to a 133 nm, 127 nm and 120 nm BC core embedded in NaCl, AS and HA, respectively. Using a core-shell model in conjunction with Mie theory to calculate $E_{Abs,\lambda}$ for each of the non-absorbing core/shell diameters results in an $E_{Abs,\lambda}$ that is 4% ± 1% higher for NaCl/BC than AS/BC over the 550 nm and 850 nm wavelength range studied here (see Fig. B6 in Appendix B). The refractive index of the coating material also affects the calculated $E_{Abs,\lambda}$. This is best shown by keeping the BC core diameter constant (127 nm) and varying the coating refractive index, where $E_{abs,\lambda}$ increases an additional 0.5% to 1% for NaCl/BC over AS/BC. Thus, for equivalent 250 nm particles using an idealized spherical core-shell model, the $E_{Abs,\lambda}$ for NaCl/BC is calculated to be 5% to 6% higher than AS/BC. TEM images show that for NaCl/BC BC is partially embedded in NaCl, whereas BC is fully embedded by AS. Despite these differences, the measured $E_{Abs,\lambda}$ are equivalent at the shortest measured wavelength region and is up to 15% higher in the near-IR for NaCl/BC, suggesting that using simple core-shell spherical models do not adequately capture $E_{Abs,\lambda}$ for embedded particles.

The spectral shape and wavelength dependence of C_{Abs} can also be described by the measured *AAE* when compared to pure BC. The *AAE* for NaCl/BC and AS/BC are within the 2σ measurement uncertainty, see Table 4.1, indicating that for BC mixed with non-absorbing materials the *AAE* is near 1.4 and independent of particle mixing state. For HA/BC the *AAE* is nearly 2. Prior modelling studies of BC embedded in absorbing and non-absorbing materials have classified the *AAE* into two regimes to help better describe measured ambient aerosol, where BC embedded with non-absorbing materials have an $AAE < 1.6$, whereas only BC embedded with an absorbing materials have $AAE > 1.6$.[27] Although this study covers a small parameter space of the possible aerosol combination of BC core diameters, core-shell ratios and BrC imaginary RI values, the presented data support this classification.

Chapter 5: Real Time Absorption Spectra of Smoke from Smoldering Combustion

5.1 Introduction

Biomass burning (BB) represents a major source of greenhouse gases and is estimated to contribute more than 35 percent of emission of global carbonaceous aerosols by mass.[199] The major particulate matter (PM) emissions from biomass burning, containing black carbon (BC), the strongest light absorber in the visible (400 nm ~ 700 nm), and primary organic carbon (i.e. brown carbon, BrC), a weak absorber of light but with a strong spectral absorption dependence, play an important role in the climate forcing[200]. Biomass burning aerosols are often considered climate neutral (-0.2 to +0.2 W m^{-2}). However recent simulations shows the contribution of biomass burning aerosols, when taking brown carbon into account, results in a net positive forcing.[201] The strong spectral dependence of absorption by brown carbon could introduce large uncertainties into radiative forcing calculation.[202]

Field measurements of optical properties of PM can be conveniently conducted during natural fires[203,204] and prescribed fires[205,206] with a controlled fire activity. However, since fuel composition in the field is complex, optical measurements cannot be correlated with specific fuel type. Laboratory-simulated fires were conducted extensively to quantify and characterize optical properties of biomass burning aerosols from a variety of fuel species, which correlate optical characterization with biomass burning emissions[207-209], combustion efficiency[210] or physical and chemical composition[211-213]. For characterization of light absorption, most measurements are carried out based on the transmission of accumulated

particles deposited on filters[209], such as with an Aethalometer[12], particle soot absorption photometer (PSAP)[13] or continuous soot monitoring system,[214] etc. In the past decades, photoacoustic spectroscopy (PA) is being accepted as a complementary method to the filter based measurement[62,203,210] with the advantage of characterizing absorption *in situ.* In both cases, optical characterization is performed with limited spectral coverage using one or multiple wavelengths due to limited laser source[208,209,213,215].

Light absorption by aerosols is often described by absorption coefficient α_{abs}., corresponding to the fractional loss in light intensity from absorption per unit propagation distance. As a useful parameter in climate models to predict radiative forcing, the mass-specific absorption cross section (MAC) can be derived from a variety of interrelated formulations

$$MAC = \frac{\alpha_{abs}}{N m_p} = \frac{C_{Abs}}{m_p} = \frac{\alpha_{abs}}{\rho}, \quad (5.1)$$

where N, m_p, C_{Abs} and M are the number density of aerosol particles, the average particle mass, the absorption cross section ($C_{Abs} = \alpha_{\mathrm{Abs}}/N$,) and the mass density of aerosol particles ($\rho = N*m_p$), respectively.

In this paper we investigate smoldering smoke particles from six types of wood that are commonly found in North America. Absorption spectra were measured between 500 nm and 840 nm, using a photoacoustic spectrometer (PA) equipped to a supercontinuum laser with a tunable wavelength and bandwidth filter. Using oak as a test case, we demonstrate here the real time measurement of Mass specific absorption (MAC) for size-selected particles by coupling PA with aerosol based classification technique, *i.e.* differential mobility analyzer (DMA) and aerosol particle mass

analyzer (APM). We also show that the smoke particles are essentially volume absorbers of light, which is confirmed by core-shell Mie calculation.

5.2 Materials & Methods

An experiment setup as in Fig. 3.1 is adopted in this study. Figure 5.1a also shows a schematic of apparatus to generate and condition smoldering smoke, including a burning chamber, a 20L buffer bottle to enable growth of particles and a set of dryers to reduce the humidity. The delivery of smoke to DMA at downstream is driven by the negative pressure generated by an ejection pump.

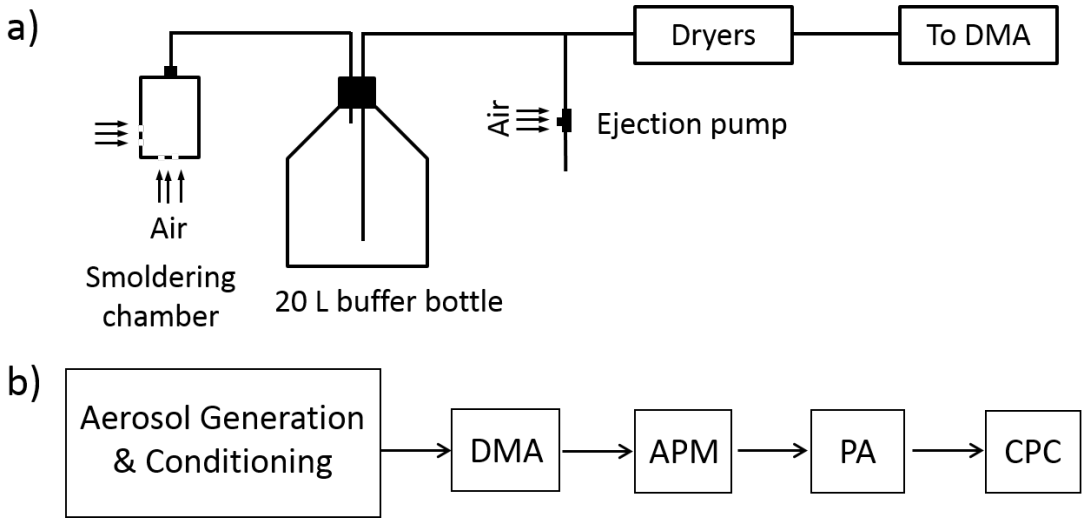

Figure 5.1 *a) schematic of Aerosol Generation & Conditioning section; b) schematic of experimental setup.*

5.2.1 Sample Generation

Six wood types (3 hardwoods and 3 softwoods) were investigated including oak, hickory and mesquite (hardwoods) and cedar, cypress and pine (softwoods). The hickory, mesquite, cedar and cypress were sourced from commercially available

wood chips, while oak chips and pine twigs were collected from the grounds of the National Institute of Standards and Technology (NIST), Gaithersburg Campus. Hille showed that only wood with a moisture content less than 14% is totally consumed during forest fires.[216] To increase consumption efficiency of fuel, wood moisture content was reduced by pre-treating all samples at 100 ^{0}C overnight prior to burning. Wood pieces were allowed to smolder in a home-made combustor in a laboratory fume hood. For each run, ≈ 100 g of fuel was used. The combustor consisted of an aluminum can 20 cm tall and 15 cm in diameter with seven 0.5 cm diameter air holes (three on side wall and four at bottom center) to supply air. An exit port in the lid was fashioned by drilling a hole to accommodate a 1.27 cm (1/2 in) NPT flange. This flange was then attached to 1/2 inch tubing serves as exit port of smoke particles. Upon ignition, the lid was left off for ≈ 1 to 2 min to allow the flame to propagate along the surface of the wood pieces. Afterwards, the can was sealed with a lid to quench the flaming combustion. Smoke was then drawn through the exit port of the lid and delivered to the rest of the system using a slight negative pressure provided by an ejection pump. In order to alleviate fluctuations in particle number density, a 20L glass carboy served as a buffer volume with a nominal particle residence time of 5 minutes.

Smoke was sampled from the main stream with a flowrate of 0.5 L min^{-1}. A conditioning system including a diffusion dryer (TSI 3062)[118] with silica desiccant, a diffusion dryer (TSI 3062) with activated carbon to remove emitted gases, and a Nafion drying tube (PermaPure MD-700-48F-3, with counter flow relative humidity (RH) held at < 5%), was used to remove residual water vapor from the flow stream

prior to size/mass selection and optical measurements. We note that this amount of conditioning may seem excessive, but was necessary to maintain all downstream measurements at constant RH over the course of a single burn; silica desiccant was changed prior to every burn.

5.2.2 Size and Mass Classification

Smoke particles were size-selected at a given mobility diameter (D_m) using a DMA (TSI 3082) that was operated with an aerosol flow of 0.5 L min^{-1} and a sheath flow of 2.5 L min^{-1}. The APM was operated in two modes in sequence: scanning mode with APM directly connected to CPC to determine mass of +1 charged particles, and fixed mass mode with APM followed by PA to select the +1 charged particles for absorption measurement. Care was taken to ensure that only +1 particles were selected by measuring particle extinction as a function of m_p as previously described by Radney and Zangmeister.[217] This combination of DMA-APM also enables determination of the effective density (ρ_{eff})

$$\rho_{eff} = \frac{6m_p}{\pi D_m^3}, \tag{5.2}$$

where D_m is the mobility diameter selected by DMA and m_p is the average mass of +1 charged particle determined from the mass distribution measured by APM and. For spherical particles, D_m is equivalent to particle physical diameter.

5.2.3 Absorption Measurement

The absorption coefficients of size- and mass-selected smoke particles were measured using a PA with a supercontinuum laser (NKT photonics SuperK Extreme EXR-15)

that outputs wavelengths spanning 475 nm to 2.5 μm. Wavelength selection of the laser beam was performed using a tunable wavelength and bandwidth filter (NKT Photonics SuperK Varia). Wavelengths spanning λ = 500 nm to 840 nm in 50 nm increments were used for measurements and bandwidths for each center wavelength were chosen in order to obtain a minimum of 25 mW of transmitted power. Intensity of the laser beam was modulated using a mechanical chopper (ThorLabs MC-2000 with MC1F30 blade) driven by a function generator (Standford Research Systems DS345). Frequency was nominally 1640 Hz at 296 K in ambient air[62]. The reader is directed to Radney and Zangmeister (2015)[58] for a detailed description on the determination of α_{Abs} using the supercontinuum PA. The MAC values were then calculated using Eq. 5.1 with knowledge of α_{Abs}, m_p from APM selection, and N from CPC measurement. The wavelength dependence of smoke particles is often characterized using absorption Ångström exponent (AAE) as in

$$AAE = -\left(\frac{\log\left(C_{Abs,\lambda_1}/C_{Abs,\lambda_2}\right)}{\log\left(\lambda_1/\lambda_2\right)}\right). \tag{5.3}$$

For dual- and triple- wavelengths measurements, one and three pairwise AAE values can be calculated, respectively, to describe the absorption spectrum[28,171,215]. To elucidate the wavelength dependence of smoke particles, light absorption was performed across the visible portion of the spectral window with enhanced resolution (8 wavelengths used presently), and thereby, the AAE can be instead be fit using

$$\mathrm{MAC}_\lambda = k_0 \left(\frac{\lambda}{500\ \mathrm{nm}}\right)^{-\mathrm{AAE}}, \tag{5.4}$$

where k_0 is a prefactor, and the MAC value, equivalent to C_{Abs}, is normalized to λ = 500 nm, similar to weighting to λ_2 in Eq. 5.3.

5.2.4 TEM Characterization

Smoke particles were collected on TEM grids (200-mesh copper grids coated with lacey carbon film) with an electrostatic aerosol precipitator (TSI 3089) at -9.3 kV collection voltage, and an aerosol flow of 0.5 L min^{-1}. Images were collected using a JEOL 2100 TEM at an accelerating voltage of 200 kV.

5.3 Results & Discussion

5.3.1 Smoldering Stability

Prior to the collection of absorption spectra, smoldering stability, absorption size dependence and TEM images of emitted particles were characterized for smoldering oak. Smoldering was able to be sustained for 30 min or longer, over which time both particle concentration and *MAC* at λ = 500 nm were collected as a function of time (see Figure 2, for 750 nm, 311 femtogram (fg) smoldering oak particles). Particle concentrations were $\approx 10^{10}$ particles m^{-3}. At the early stages of each experiment, after sealing the combustor, a short period of flaming combustion persisted and *MAC* values as high 0.25 m^2 g^{-1} were measured, likely due to BC within the emitted particles.[206] After a few minutes, the flaming subsided and smoldering persisted as evidenced spectrally by the nearly order of magnitude reduction in *MAC*. These observations are consistent with Holder, *et al* (2016).[206] who quantified the BC concentration during burning and observed a correlation between BC and *MAC* during the transition between flaming to smoldering. At times spontaneous flaming would occur due to rearrangement on the material in the smoldering chamber. This could be explained by an increase in the *MAC* due to generated soot coagulate with

organic particles, and a decrease in particle concentration due to consumption of organic particles (see spike in measured *MAC* at 6 and 25 minutes in Figure 2).

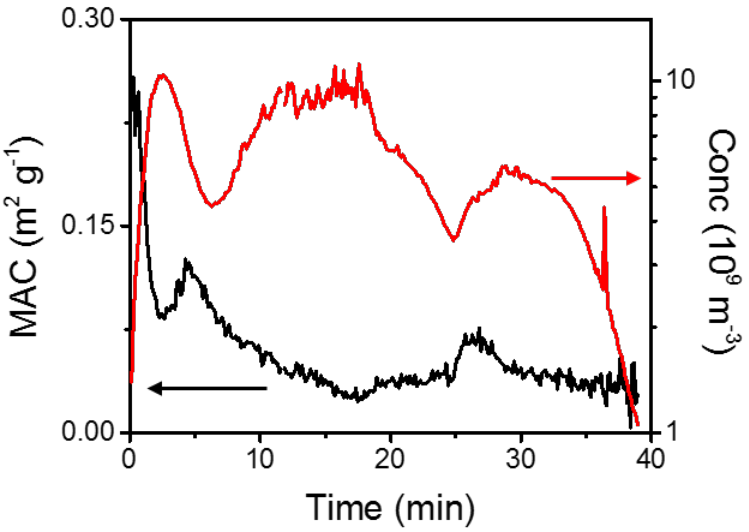

Figure 5.2 *Time evolution of MAC (black) for 750 nm smoke particles from burning of oak wood, corresponding to mass of 269.9 fg, measured at wavelength of 500 nm along with the corresponding number concentration (red).*

5.3.2 Particle Characterization

Figure 3a shows measured MAC at λ = 660 nm for smoldering oak particles with selected diameters ranging from 500 nm to 900 nm. The population of MAC is observed to be essentially invariant with D_p. The median of MAC is ~ (0.008 ± 0.002) $m^2\ g^{-1}$ for all sizes, which is about three orders of magnitude lower than the MAC of BC (~ 7.5 $m^2\ g^{-1}$)[149,218]. The constant MAC over sizes indicates the particles are basically optical volume absorber (in Rayleigh regime) despite the dimension of particles comparable to the wavelength. The mean is higher than the median, indicating selected particles were mostly weakly absorptive but with some outliers, consistent with the observation in Figure 2.

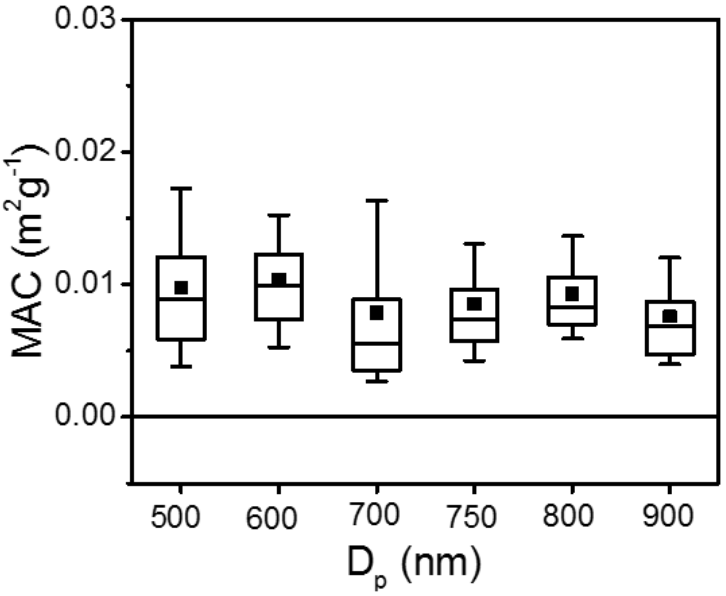

Figure 5.3 *MAC of oak smoke as a function of particle size measured at λ = 660 nm. The box and whisker plot shows experimental data where the box represents the range of 25% and 75% percentile, the dash in the box is the median and the solid square is the mean.What does the whisker correspond to – the range of the data? How long does the scan take? What is variability in the result as a function of time – is that what the error bars represent?*

Aerosol formation during biomass burning is described as a condensation process, which produces solid or liquid particles. [149]Figure 4 shows a TEM image of oak smoke collected during the smoldering phase where the *MAC* is constant. No aggregated particles, indicative of BC[132,219], were observed. Instead, the grid is nearly universally coated with individual liquid-like droplets and membranes, similar to previous observations of cellulose smoldering and consequent condensation of volatilized organics.[220]

The measured density ranges from (1.35 ± 0.01) g cm^{-3} for Cypress, to (1.51 ± 0.03) g cm^{-3} for Mesquite, as listed in Table I. It is observed that density of smoke particles is higher for hard wood than that for soft wood.

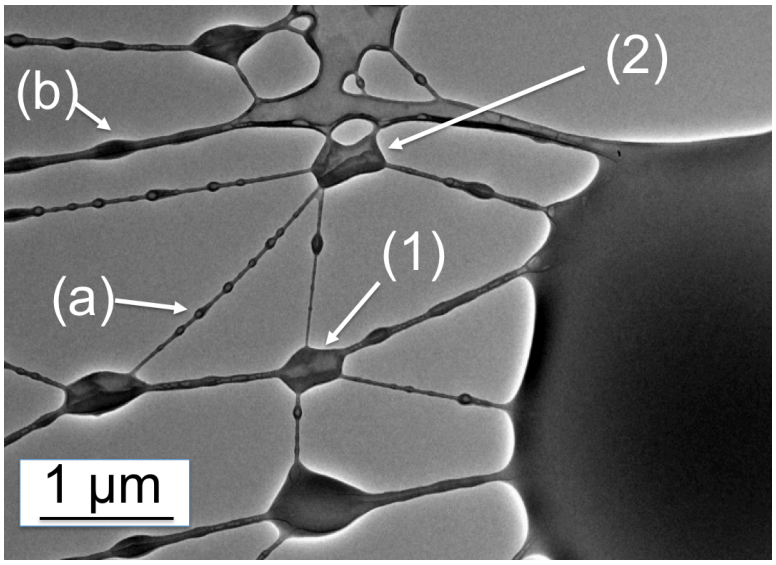

Figure 5.4 *TEM images of particles collected from smoldering oak. Liquid-like material forms droplets on thin (a) and thick (b) meshes. Liquid membranes are formed on the junctions of carbon fibers (1) and the holes on the carbon film (2).I do not understand this image. The images I have seen of smolder smoke are circular.*

5.3.3 Smoldering Wood Absorption Spectra

Figure 5 shows the MAC spectra of D_m = 750 nm smoke particles from smoldering six types of wood collected over a whole cycle of smoldering. Medians of MAC are also listed in Table I. Overall, the MACs of smoke particles are at least two orders of magnitude lower than that of BC (~ 7.5 $m^2 g^{-1}$)[149,218] with the greatest measured MAC at ~0.14 m^2 g^{-1} for Hickory at λ=500 nm. The strongest absorber is Mesquite and hickory which have MACs about 4 times greater than that of the weakest absorbers,

oak and cedar. No distinct correlation of absorption between hard wood (Oak, Hickory and Mesquite) and soft wood (Cedar, Cypress and Pine) is observed.

Despite the low MAC compared to that of BC, the smoke exhibits significantly increasing absorption towards the shorter wavelengths. The AAE was fit over λ = 500 nm to 840 nm and are listed in Table I. As shown, all AAE values are above 3.68 and are significantly higher than the quoted AAE of 1 for BC [149]. This large AAE is consistent with the reported wavelength dependence of BrC [168,221]. The mean of MAC is higher than the median in all wavelengths, suggesting majority of particles possessing low MAC were collected during smoldering phase, while there were periods, e.g. intermittent flares, when particles with high MAC were emitted.

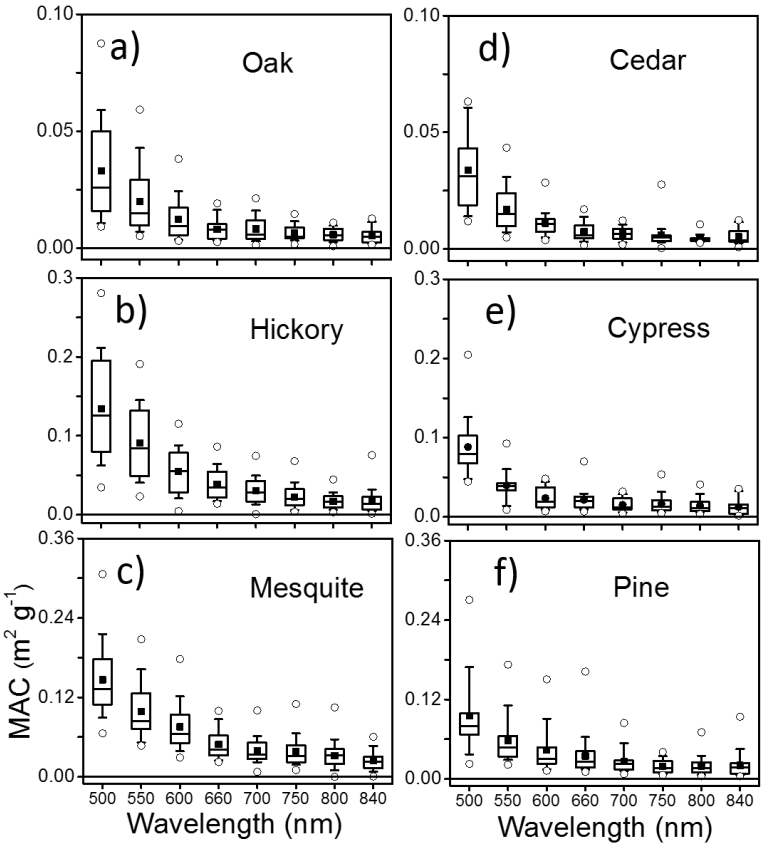

Figure 5.5 *MAC spectra of smoke particles from smoldering six types of wood. The box and whisker plot show the mean (■), median (-), 25% and 75% percentile (box), 10th and 90th percentile (whisker) and outliers (○).*

Table 5.1 *Density, AAE and median MAC (λ=500 nm) of 750 nm smoke particles for 6 wood samples. Soft wood is highlighted with gray.*

	Density (g/cm^3)	AAE (from median, 500 ~ 840 nm)	Median MAC (m^2/g) at λ=500 nm
Cedar	1.36±0.03	5.31±0.53	0.031
Cypress	1.35±0.01	5.58±0.72	0.079
Pine	1.35±0.02	3.79±0.37	0.080
Oak	1.41±0.04	4.13±0.43	0.026
Hickory	1.44±0.05	4.46±0.08	0.126
Mesquite	1.51±0.03	3.68±0.25	0.133

5.4 Summary

In conclusion, absorption spectra of laboratory produced smoldering smokes from six types of wood were investigated. Absorption data were measured *in situ* between 500 nm and 840 nm using a photoacoustic spectrometer and step-scanning a supercontinuum laser source coupled to a tunable wavelength and bandwidth filter. Smoldering smoke particles were mobility and mass-selected prior to optical characterization allowing data to be reported as mass-specific absorption cross sections (*MAC*). The measured *MAC* at 500 nm was time dependent, ranging from 0.25 m^2g^{-1} and gradually dropped to 0.03 m^2g^{-1} within 12 min of smoldering initiation. All six materials studied had a median *MAC* ranging between 0.026 $m^2\ g^{-1}$ to 0.133 $m^2\ g^{-1}$ at a wavelength of 500 nm and absorption Ångström exponents (*AAE*)

ranged between 3.68±0.25 (Mesquite) to 5.58±0.72 (Cypress), consistent with reported AAEs for BrC in general. It was shown both experimentally and computationally that smoldering smoke particles as big as 750 nm in diameter behave as volume absorbers due to weakly absorption of light.

Chapter 6: Conclusion and Future Work

In summary, the work discussed in this dissertation is devoted to laboratory studies of optical absorption by atmospherically relevant aerosols. Such information is important to to predicting the radiative forcing of aerosols in the terrestrial atmosphere that impacts climate change. Here a photoacoustic spectrometer is used to quantify the absorption coefficient of particles *in situ*. Aerosol-based classification technique, i.e. DMA and APM, are implemented to enable absorption measurements based upon pre-size/mass- selected particles. Such size dependent data is essential for testing and developing models for the optical properties of black and brown carbon particles. Basically the work involves two main parts: development of calibration methods for instrumentation (Chapter 2 & 3) and characterization of absorption by laboratory-generated aerosols that are relevant to particles in atmosphere (Chapter 4 & 5).

For calibration of DMA, bio-nanoparticles were proposed as a candidate reference material for determining the mobility of nanoparticles over the range of $(6\times10^{-8}$ - $5\times10^{-6})$ $m^2V^{-1}s^{-1}$ in Chapter 2. Using an electrospray differential mobility, I measured the empirical distribution of several bio-nanoparticles, all of which show monomodal distribution that are more than two times narrower than the currently used calibration particles for electrical mobility larger than 6×10^{-8} $m^2V^{-1}s^{-1}$ (diameter less than 60 nm). I also presented a numerical method to calculate corrected distribution of bio-nanoparticles by separating the contribution of the diffusive transfer function. Despite that the corrected distribution is about 20% narrower than the empirical distribution, the reduced width of this corrected distribution is about a

factor of 2 larger than the diffusive transfer function, which could result from the nonuniform conformation of bio-nanoparticles and from the presence of volatile impurities or solvent adducts. I also found the mobilities of these investigated bio-nanoparticles are stable over a range of buffer concentration and molarity, with no evidence of temporal degradation over several weeks.

In Chapter 3, I explored three aerosol standard candidates for PA measurement, including fullerene C_{60}, copper and silver. Comparisons were made between experimental photoacoustic absorption data with Mie theory calculations at wavelength of 405 nm or/and 660 nm. I identified the feasibility of C_{60} particles with a mobility diameter of 150 nm to 400 nm as an absorbing standard at wavelengths of 405 nm and 660 nm. Copper particles with a mobility diameter of 80 nm to 300 nm are also shown to be a promising reference candidate at wavelength of 405 nm. I proposed recommendation to select metallic aerosol standards for PA measurement taking into account the wavelength where the plasmonic resonance would occur, based upon the investigation of the deviation of experiment from theory for absorption of copper at 660 nm and that of silver at both 405 nm and 660 nm.

With well-calibrated instruments, I investigated light absorption by atmospherically relevant aerosols. In Chapter 4 I measured optical absorption spectra of laboratory-generated aerosols consisting of black carbon (BC) internally mixed with non-absorbing materials (ammonium sulfate, AS, and sodium chloride, NaCl), and BC with a weakly absorbing brown carbon surrogate derived from humic acid (HA) across the visible to near-IR (550 nm to 840 nm). Using MSTM method, I predicted the manner in which BC mixed with each material that was confirmed by

TEM images. The absorption enhancement of BC was found to decrease from 1.5 at λ = 550 nm with increasing wavelength for AS/BC, while NaCl/BC enhancement was essentially wavelength independent. For HA/BC, the enhancement ranged from 2 to 3 and was strongly wavelength dependent. Theoretically removal of the HA absorption contribution to enhancement revealed that the enhancement was ≈ 1.5 and independent of wavelength.

Biomass burning (BB) is a large contributor to carbonaceous aerosols in the terrestrial atmosphere. High in mass concentration, but weakly absorbing across the visible portion of the spectrum, much of the BB is formed from smoldering smokes. In Chapter 5 I investigated absorption spectra of laboratory-produced smoldering smokes from six types of wood over wavelength of 500 nm to 840 nm. Using Oak as a test case, I demonstrated the measured MAC at λ=500 nm was time dependent, ranging from 0.25 m^2g^{-1} and gradually dropped to 0.03 m^2 g^{-1} within 12 min of smoldering initiation. It was found that all six materials studied had a median *MAC* ranging between (0.026 to 0.133) m^2 g^{-1} at a wavelength of 500 nm and absorption Ångström exponents (*AAE*) ranged from 3.7 to 5.6. It was shown both experimentally and computationally that weakly absorbing smoldering smoke particles behave as volume absorbers for particles despite of large particle diameter selected at 750 nm that is comparable to the wavelength.

One future extension of this work would involve comparison with ground-based measurement as well as satellite measurement that contributes to better quantify the role of aerosols in climate change. Mass specific absorption cross section (MAC) measured in this dissertation is a critical input of global climate model to

calculate radiative forcing of aerosols. It would be beneficial to build a MAC inventory for the major species of atmospheric aerosols that helps to isolate the absorption contributions of each aerosol species from field measurement. Combined with global aerosol emission inventory, radiative forcing of major aerosols species can be evaluated in the full solar spectrum with aid of the broadband supercontinuum laser. From the computation perspective, discrete-dipole approximation method (DDA)[222] can be introduced to calculate optical properties of non-spherical particles and compared with MSTM method. In investigation of optical absorption enhancement of NaCl/BC, for example, since NaCl exists as crystalline cubics, the spherical assumption in MSTM would cause error in estimation of absorption cross section. Future calculation could use DDA to calculate optical properties of particles with arbitrary shape and multiple components, and to estimate the influence of spherical assumption used in other methods. On the other hand, there exists no unique morphology of soot particles for a given set of fractal parameters, i.e. fractal dimension D_f and prefractor f_0. Thereby, future work could involve investigation of statistics of light absorption by particles with morphology described by the same D_f and f_0.

Appendices

A. Supplemental Information for Chapter 3

A.1 Size Distribution of Fullerene C_{60} Nanoparticles

Fullerene C_{60} nanoparticles were generated by sublimating C_{60} powder in a flow of nitrogen with heating temperature of 650 °C. The size distribution of generated C_{60} nanoparticles is shown in Fig. A1 peaking at around 239 nm.

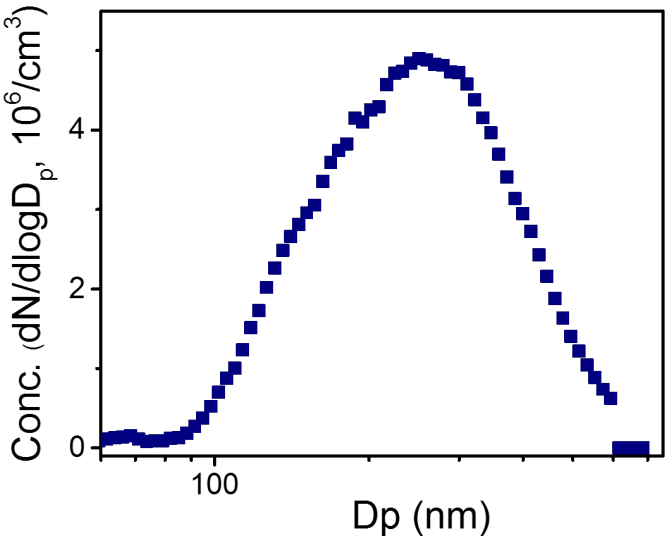

Figure A1 *Size distribution of C_{60} nanospheres.*

A.2 Mass-mobility Scaling Relationship

The aggregate morphology of a particle with a mobility diameter D_m can be described via

$$m_p = m_{p,0}\left(\frac{D_m}{D_{m,0}}\right)^{D_{fm}}, \tag{A1}$$

where D_{fm} is mass-mobility scaling component, $m_{p,0}$ is the particle mass for an arbitrarily chosen mobility diameter $D_{m,0}$. The mass mobility scaling relationship for as generated nanospheres of silver, copper and fullerene C_{60} is shown in Fig. A2.

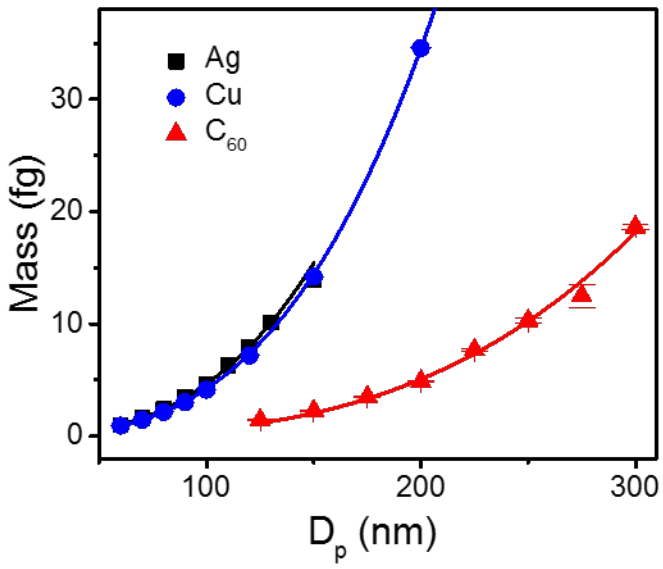

Figure A2 *Mass mobility scaling relationship of silver, copper and C_{60} nanospheres.*

A.3 SEM images of Copper Nanospheres at Different Synthesis Temperature

To investigate morphology effect of particles on the absorption measurement, copper particles were synthesized at different temperature in order to yield nanospheres with various morphology. The SEM images are shown in Fig. A3. Rough surfaces as well as voids are evident on particles synthesized at 380 ^{0}C. As temperature increases, particles become more spherical and dense.

A.4 Effect of 405 nm Laser Power

Measured PA signal is known to be proportional to the peak-to-peak laser intensity. In this study 660 nm laser outputs power half of the laser power emitted by 405 nm, which could be potential contributor to the discrepancy between PA measurements and Mie calculation at λ=660 nm. Here I studied the effect of laser power on PA absorption by measuring C_{Abs} of copper nanoparticles at 405 nm with laser

performing at the comparable signal level as at 660 nm. I first calibrated the laser

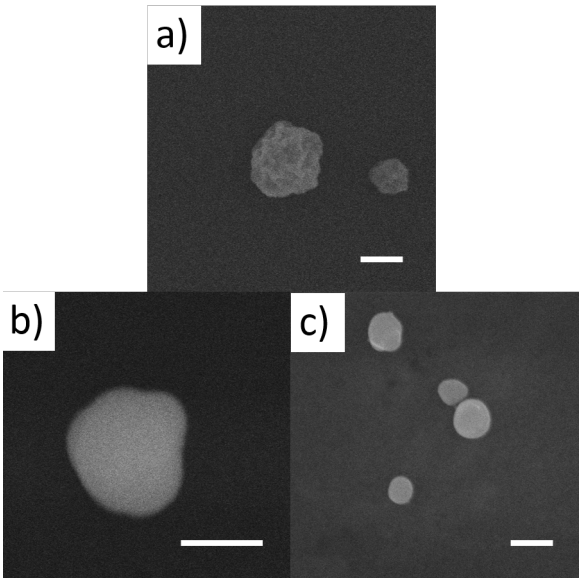

Figure A3 *SEM images of copper nanosphere synthesized at a) 380 ^{0}C, b) 500 ^{0}C and c) 650 ^{0}C.*

power as a function of the operating voltage of the 405 nm laser which shows a linear relationship in the regime of 0.45V to 0.95V, see Fig. A4. PA measurements were then carried out for multiple D_m of copper particles (60 nm to 200 nm) using laser voltage ranging from 0.45 V to 0.95 V with an interval of 0.1 V. Particles of most sizes exhibit a measured C_{Abs} constantly being 60 % ~ 90% of C_{Abs} calculated using Mie theory over all voltages, while particles of 60 nm in diameter absorbs only 30% ~ 50 % of Mie prediction, as shown in Fig. A5. Finally, I found 405 nm laser yields comparable signal level as 660 nm laser when operating at 45 % ~55 % of the full power.

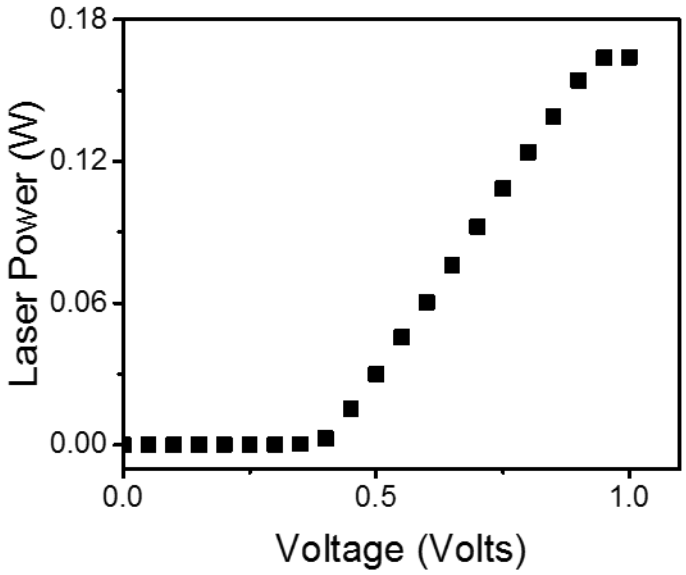

Figure A4 *Calibration of output laser power with operating voltage of PA 405 nm laser.*

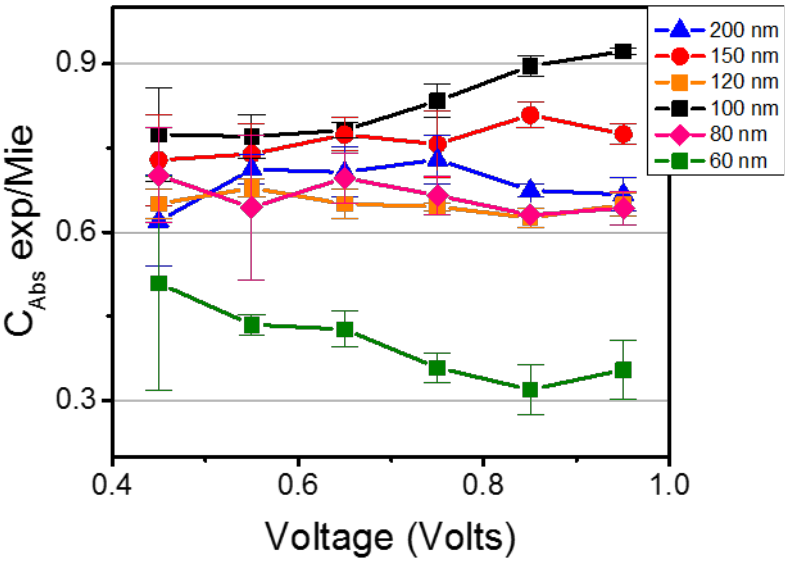

Figure A5 *Comparison of measured C_{Abs} with Mie calculation for multiple size of copper nanoparticles at λ=405 nm using different operating voltage of PA laser.*

A.5 Effect of Particle Morphology

As shown in TEM images, some of the metal particles are slightly prolate, deviating from perfect sphere, which indicates there exists intrinsic errors using homogeneous sphere model in the Mie calculation. Whether these spheroids contribute to the experiment and calculation discrepancy at λ=660 nm depends on how much the optical absorption was affected by the prolate eccentricity. Discrete dipole approximation (DDA) is known as a powerful technique for computing scattering and absorption by target of arbitrary geometry. I calculated C_{Abs} of copper using DDA by constructing spheroids with aspect ratio (ratio of semi-major axis to semi-minor axis) up to 1.5. Comparison with C_{Abs} of spheres with equivalent diameter indicates C_{Abs} rises for both wavelength as the particle become more prolate. However, the effect is small, e.g. up to 16% and 8% rise in absorption at λ=405 nm and λ=660 nm, respectively.

Experimentally, I measured C_{Abs} of copper particles synthesized at various heating temperature (*HTemp*, 450 ^{0}C, 650 ^{0}C and 750 ^{0}C). The basic assumption is that particles are less dense and less spherical with decreasing *Htemp* which allows us to examine the impact of non-sphericity. From SEM images, it is not easy to differentiate the particles synthesized at *Htemp*=650 ^{0}C and 750 ^{0}C, which are dense and spherical, while nonspherical particles with rough surface are prevalent in the SEM images for *Htemp*=450 ^{0}C. PA measurement shows increasing C_{Abs} for lower heating temperature, but only up to 20% rising for both wavelength, which is consistent with the calculation above, see Fig. A6.

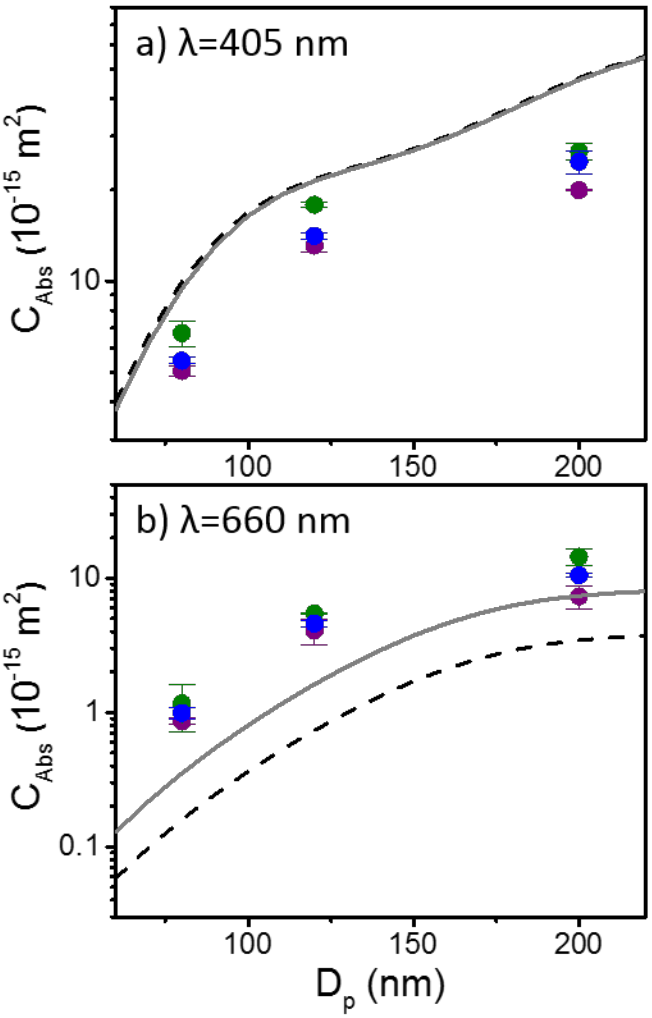

Figure A6 *Absorption cross section C_{Abs} of copper nanoparticle a) at λ=405 nm and b) λ=660 nm. Green, blue and purple dots correspond to particle synthesized at temperature of 450 ^{o}C, 650 ^{o}C and 750 ^{o}C, respectively. Results are reported as experimental mean and 2σ uncertainty propagated across all measurements. Mie calculations are also shown using refractive index from Palik* [110] *(solid gray lines) and McPeak* [111] *(dashed black lines), respectively.*

A.6 Calibration of Measured D_p with PSLs

NIST-traced size standard polystyrene latex beads with three nominal sizes (60 nm, 100 nm, 150nm) were used to calibrate the measured D_p in nitrogen and in forming gas, as shown in Fig. A7. The actual D_p was then extrapolated from this linear relationship based upon the nominal D_p selected on the DMA panel.

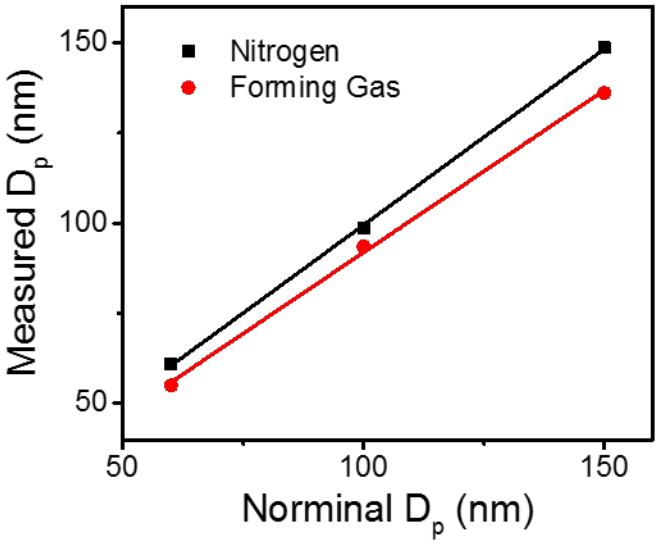

Figure A7 *Measured D_p of NIST-traced size standard polystyrene latex beads as a function of nominal D_p.*

B. Supplemental Information for Chapter 4

B.1 Drop Cast TEM Images

The as received BC suspension was diluted with DI H_2O and drop cast on TEM grids. After drying overnight at room temperature, the BC was imaged using TEM and shown in Fig. B1. Agglomerates of ≈ 30 nm monomers with discontinuous onion-like fringes are observed, similar to the monomers in Fig. 4.1a.

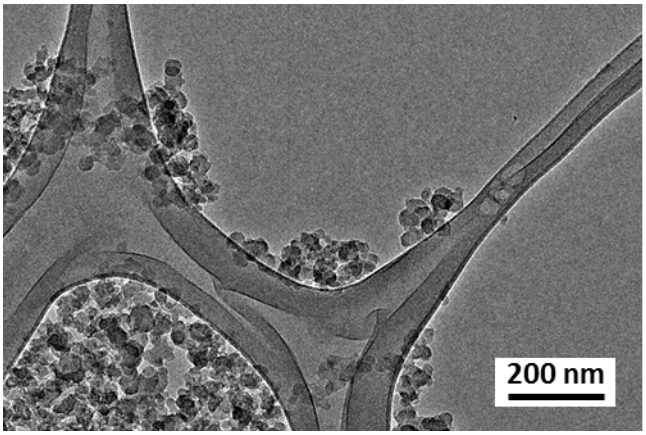

Figure B1 *TEM images of drop cast BC suspension.*

B.2 Measurement of Aerosol Extinction

The extinction cross sections (C_{Ext}) of bare BC particles were measured using a cavity ringdown spectrometer (CRD) at λ = 660 nm to retrieve the refractive index (RI) of BC in conjunction with the absorption cross section (C_{Abs}) from the photo-acoustic spectrometer (PA) measurements. The schematic of experimental setup is shown in Fig. B2.

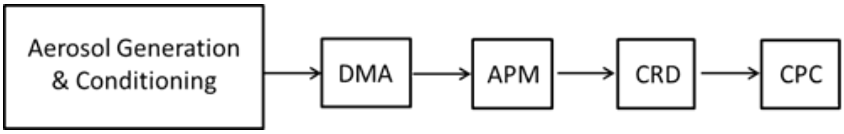

Figure B2 *Experimental schematic used for determination of optical extinction.*

The optical cavity used here was fashioned after a similar one used for gas-phase absorption measurements[223] with some variation to accommodate aerosols. Particles flow into the cavity at 0.5 L min^{-1} with an additional 1.0 L min^{-1} being flushed around the windows to prevent particle deposition. A λ = 660 nm continuous wave diode laser is used to pump a high finesse optical cavity to saturation. Then the light is quickly terminated (tens of nanoseconds) using an acousto-optic modulator, and the intra-cavity light intensity decays exponentially in time as a result of absorption and scattering (the sum of which is extinction) from gas- and aerosol-phase species and window losses. Aerosol extinction coefficients (α_{ext}) are determined by taking the difference in ringdown times between aerosol-laden and clean (HEPA-filtered) cavity conditions, τ and τ_0, respectively:

$$\alpha_{Ext} = \frac{L}{cd}\left(\frac{1}{\tau} - \frac{1}{\tau_0}\right), \tag{B1}$$

where L is the total length of the cavity, d is the length of the cavity occupied by aerosol and c is the speed of light; aerosol-free ringdown times were nominally 22 μs. To evaluate the precision and stability of the system performance, an Allan variance test was performed prior to the measurement which yielded an 1s detection limit of 4.9×10^{-7} m^{-1}.

B.3 Determination of Refractive Index

The BC refractive index (RI) was calculated from extinction and absorption cross section measurements made at λ = 660 nm on mass-selected 150 nm to 400 nm mobility diameter particles, assuming monodisperse distribution for all size-selected particles, Distinct peaks corresponding to different charge states were observed in the mass distribution of selected particle size as observed in Radney, et at. (2013).[224] Following the discussion of Radney and Zangmeister (2016),[182] mass-selection by the APM for these nearly-spherical particles (See section on mass-mobility scaling exponent) ensured that only particles with q = +1 were measured. Further, measurements were performed where C_{ext} possessed a stable slope. The refractive indices were calculated using a weighted sum method[225] including both C_{ext} and C_{abs}, as it has been shown that the combination of extinction and absorption data greatly improves the retrieval of RI compared to the extinction-only retrievals.[226] The measured extinction and absorption cross-sections ($C_{ext,measured}$ and $C_{abs,measured}$, respectively) are used to minimize the merit function (χ^2), with the refractive index (m = n + ik) treated as the fitted parameter for the calculation of $C_{ext,calculated}$ (n, k) and $C_{abs,calculated}$ (n, k) from Mie theory. Mathematically:

$$\chi^2(n,k) = \frac{1}{N_{ext}}\sum_{i=1}^{N_{ext}}\frac{\left(C_{ext,measured}-C_{ext,calculated}(n,k)\right)_i^2}{\varepsilon_i^2} + \frac{1}{N_{abs}}\sum_{j=1}^{N_{abs}}\frac{\left(C_{abs,measured}-C_{abs,calculated}(n,k)\right)_j^2}{\varepsilon_j^2}, \quad \text{(B2)}$$

where N is the number of mobility diameters measured, and ε_i is the standard deviation of multiple measurements for size i. The optical cross sections are

calculated using the homogenous spheres routine described in Appendix A of Bohren and Huffman (1983).[227] The algorithm scans through possible values of indices with interval of 0.001 for both n and k until converging to the merit function's absolute minimum χ^2_{min}. This value is taken as the average RI of the BC aggregate and air, from which the RI of BC bulk is retrieved using Bruggeman mixing rule[227] for an assumed packing density calculated from the effective density.[228] The uncertainty of the retrieved RI was approximated from the vicinity of χ^2_{min} for RI satisfying

$$\chi^2 - \chi^2_{min} \leq \chi^2_{crit}, \quad \text{(B3)}$$

at a 95% confidence level where χ^2_{crit}=19.6751 for the eleven degrees of freedom. The error of RI is given as the standard deviation of all n and k that satisfying this relationship. For BC and air, the RI was determined to be (1.32 ± 0.01) + i(0.31 ± 0.01). Applying the Bruggeman mixing rule yields a BC RI of (1.77 ± 0.02) + i(0.80 ± 0.01) and was assumed to be wavelength independent.[149]

Unlike BC, the RI of BrC is expected to vary with wavelength. To account for the wavelength dependence of BrC the RI was first determined at λ = 660 nm as described above. Over the wavelengths of interest, I assumed that the real part of the RI was wavelength independent. For the imaginary component of the RI, the absorption spectrum of an aqueous solution across the wavelength region of interest was measured (see Fig. B3), as the solution, in principle, captures the absorption from the bulk material, as demonstrated in Radney and Zangmeister (2015).[58] The absorption coefficient $\alpha_{abs,bulk}$ can be related to the imaginary component (k) and the wavelength λ through[227]

$$\alpha_{abs,bulk} = \frac{4\pi\kappa}{\lambda}, \tag{B4}$$

Thus, it follows that

$$\frac{A_{\lambda 1}}{A_{\lambda 2}} = \frac{\alpha_{\lambda 1}}{\alpha_{\lambda 2}} = \frac{k_1\lambda_2}{k_2\lambda_1}, \tag{B5}$$

where A_λ is the measured absorption measured at wavelength λ.

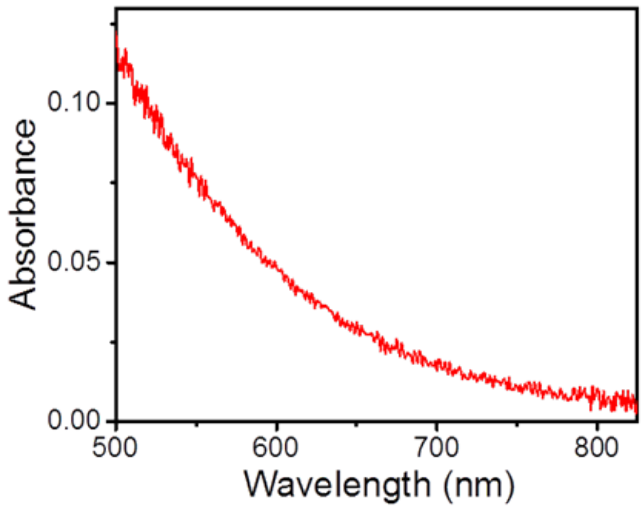

***Figure B**3 Measured absorption spectrum of BrC (from UV-vis spectrophotometer).*

B.4 Mass-mobility Scaling Relationship

A surrogate for aggregate fractal dimension, the mass-mobility scaling exponent (D_{fm}),[10,11] relates particle mass (m_p) to the electrical mobility diameter (D_p) through

$$m_p = m_{p,0}\left(\frac{D_m}{D_{m,0}}\right)^{Dfm}, \tag{B6}$$

where $m_{p,0}$ corresponds to the particle mass for an arbitrarily chosen mobility diameter $D_{m,0}$.[229,230] Figure B4 shows the mass-mobility scaling relationship for BC and HA with $D_{m,0}$ =150 nm; the corresponding $m_{p,0}$ and D_{fm} are (1.50 ± 0.01) fg and (2.83 ± 0.01), and (2.50 ± 0.10) fg and (3.10 ± 0.4), respectively.

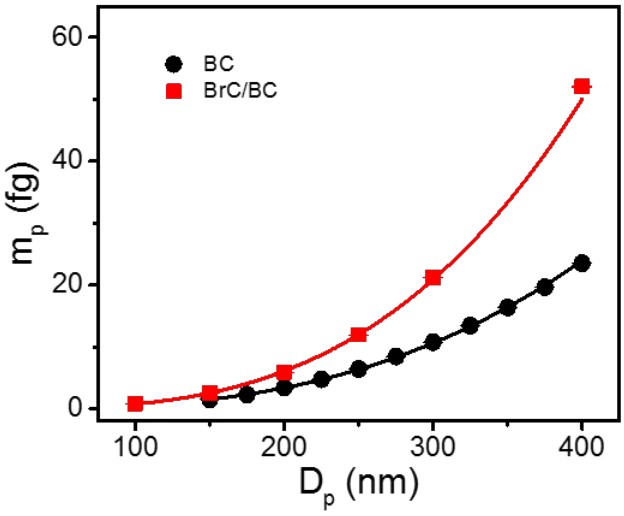

Figure B4 *Plot of mass-mobility scaling relationship for pure BC and HA.*

B.5 Modeling BC Optical Properties

The BC particle morphology constrained by

$$N_m = k_0 \left(\frac{2R_g}{D_m}\right)^{D_f}, \tag{B7}$$

where R_g is the gyration radius of the aggregate, D_m is the diameter of monomer, and N_m represents the number of monomers, respectively. Although not physically equivalent,[231,232] the fractal dimension, D_f, of BC was chosen to be the same value as the measured mass-mobility scaling exponent.[229,230] Previous studies have retrieved aggregate morphological parameters by coupling TEM projected with image analysis;[233,234] a similar procedure was used in this investigation. To determine N_m for a 250 nm BC aggregate, I relate N_m to the projected number of monomers N_{proj} in the TEM image of a typical BC aggregate (Fig. 4.1a) via the empirical formula[235]

$$N_m/N_{proj} = 0.46e^{0.68D_f}, \tag{B8}$$

where N_{proj} was determined from the ratio of the aggregate projected area to the average monomer area. Hence, the estimated N_m for the aggregate in the inset of Fig. 4.1a is 218 given an average D_m of 30 nm. Furthermore, Brasil et al. (1999)[233] suggested a ratio of 3 between the longest projected dimension L_{max}^{2D} to the radius of gyration R_g^{3D}. Therefore, the structural prefactor k_0 can be calculated by rewriting Eq. 6 as

$$k_0 = \frac{N_m}{\left(2L_{max}^{2D}/3D_m\right)^{D_f}}. \quad \text{(B9)}$$

Table B1 *Model parameters for BC core and shell materials.*

	BC	AS	NaCl	BrC
ρ (g cm^{-3})	1.8	1.77	2.17	1.48[a)]
RI	1.77+i0.80[b)]	1.53[236]	1.54[237]	1.58+i0.02 at 660 nm**

a) From DMA-APM measurement (as for bare BC in Sec. 4.3.1)

b) Retrieved from Cavity Ring-Down + PA. See discussion in text.

B.6 Comparison of BC MAC from Fig. 4.1b and Fig. 4.1c

The MAC was calculated from the slope of C_{Abs} vs. m_p as shown in Fig. 4.1b and compared to the MAC calculated from a single point measurement in Fig. 4.1c. At each wavelength, the single point MAC was within 10 % of the linear fit to MAC as shown in Table B2.

Table B2 *MAC of BC as calculated from slope of* C_{abs} *vs.* m_p *in Fig. 4.1b and from a single point* C_{abs}/m_p *in Fig. 4.1c for a* D_p *= 250 nm particle.*

Wavelength (nm)	MAC ($m^2 g^{-1}$)		% Difference
	Fig. 4.1b*	Fig. 4.1c	
600	6.90 ± 0.04	7.47 ± 0.30	8.3
700	6.10 ± 0.06	6.43 ± 0.09	5.4
800	5.39 ± 0.06	5.41 ± 0.13	0.4

* Linear fit for $m_p \leq 10.48$ fg

B.7 TEM Images of Particle Melting

To reveal BC core in the mixing particles, I intentionally melt the particles by exposing them to the focused electron beam in the TEM. Upon exposure, the exterior of AS/BC particle bubbles and evaporates gradually, leaving only BC aggregates (Fig. B5a, B5b, and B5c). Similarly, for NaCl/BC particles, NaCl cubes turn transparent and collapse, revealing BC core (Fig. B5d, B5e, B5f).

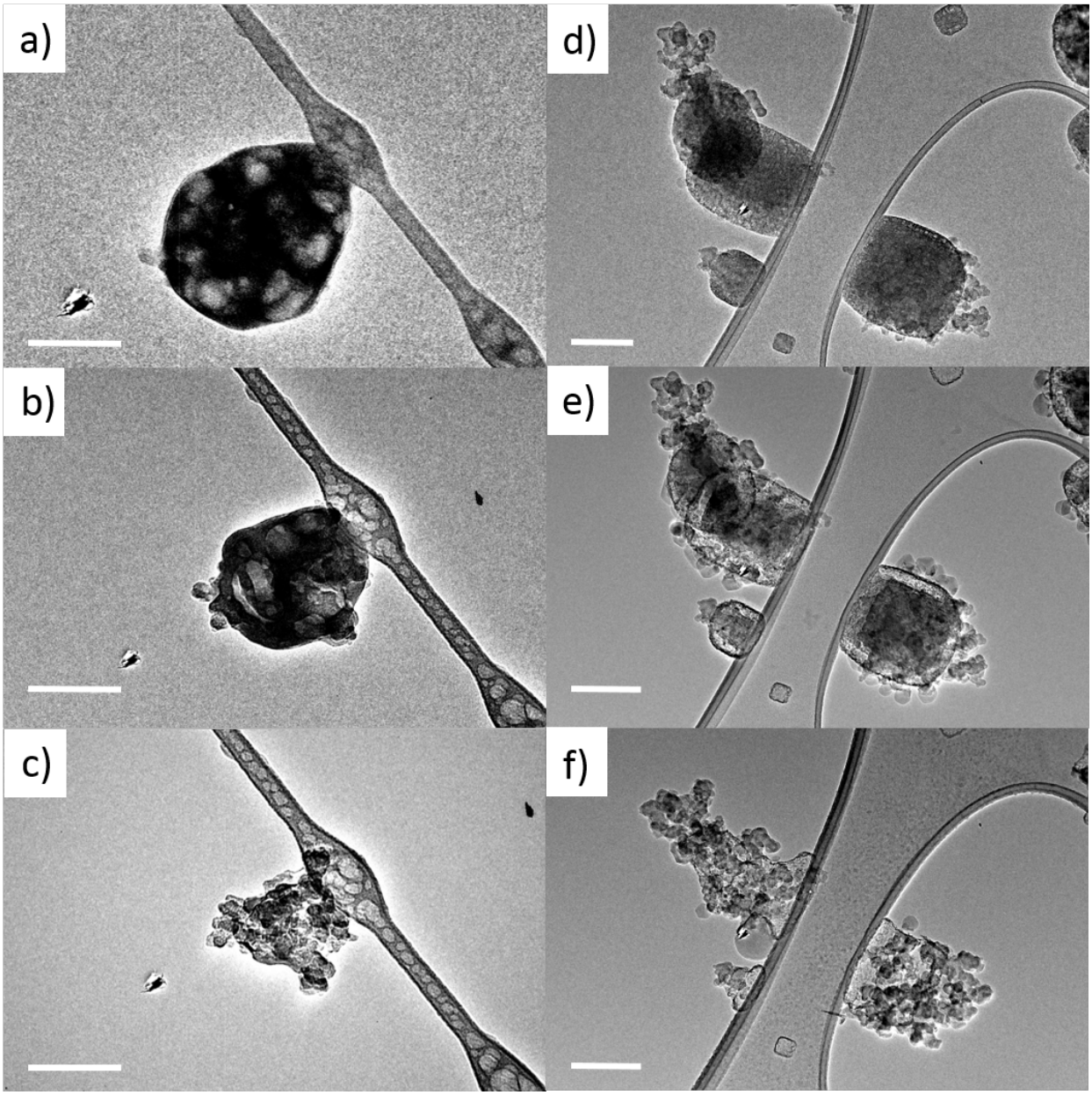

Figure B5 *TEM images showing evolution of mixed particles upon exposure to electron beam for AS/BC (a, b and c) and NaCl/BC (d, e and f). Scale bar corresponds to 100 nm in all images.*

B.8 Influence Core/Shell Size and Refractive Index on Absorption Enhancement

Figure B6 demonstrates how core/shell size (Fig. B6a) and RI (Fig. B6b) affect the absorption enhancement $E_{Abs,\lambda}$ using a core shell Mie theory. For a 250 nm particle, core diameters of 127 nm and 120 nm, corresponding to the BC core in AS/BC and NaCl/BC particles, respectively, were assumed and the RI of the shell was taken to be 1.53 (i.e. AS). The calculated $E_{Abs,\lambda}$ was found to be (3 to 6) % higher the particles with the smaller core, see Fig. B6a. On the other hand, for a 250 nm particle with a BC core at fixed diameter of 127 nm, varying RI of shell from 1.53 to 1.54 only elevates E_{Abs} for < 1%, as shown in Fig. B6b.

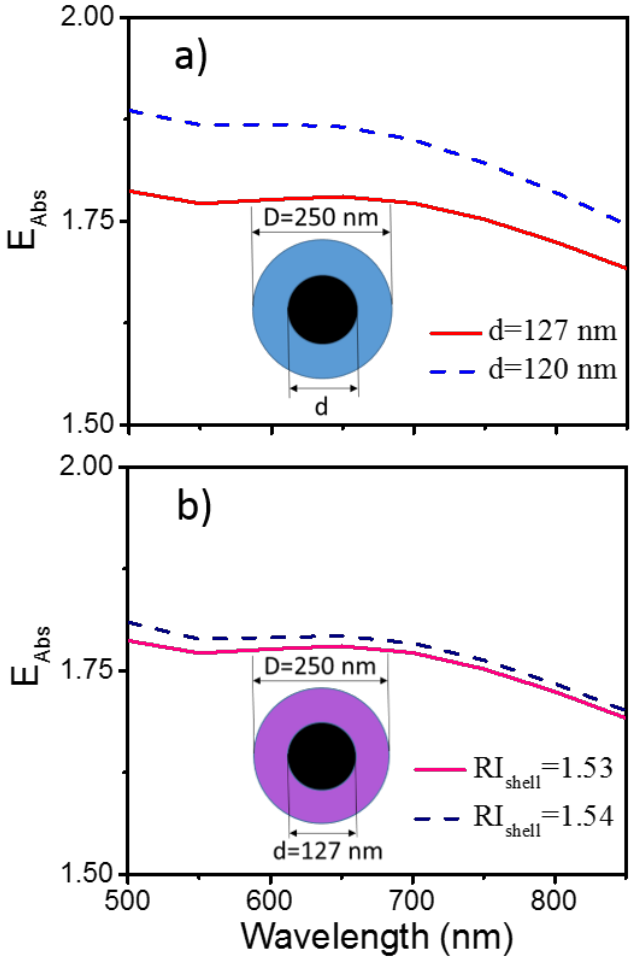

Figure B6 *Core-shell Mie calculation of E_{Abs} for a) 250 nm particle with 127 nm (solid red) vs. 120 nm (blue dashed) BC core with a shell refractive index of 1.53, and b) 250 nm particle with a 127 nm BC core with shell refractive indices of 1.53 (solid magenta) vs. 1.54 (blue dashed).*

Bibliography

(1) J. H. Seinfeld, S. N. P., *Atmospheric Chemistry and Physics*. Wiley: New York, NY, 1998.
(2) Hinds, W. C., *Aerosol Technology: Properties, Behavior, and Measurement of airborne particles*. 2nd ed.; John Wiley & Sons, Inc.: New York, NY, 1999.
(3) Stier, P.; Seinfeld, J. H.; Kinne, S.; Boucher, O., Aerosol absorption and radiative forcing. *Atmos Chem Phys* **2007,** *7* (19), 5237-5261.
(4) S. Solomon, D. Q., M. Manning, Z. Chen, M. Marquis, K. B. Averyt, et. al. *Climate Change 2007: the physical science basis, contribution of working group I to the fourth assessment report of the intergovernmental panel on climate change*; IPCC Secretariat: Geneva, Switzerland, 2007.
(5) Satheesh, S. K.; Moorthy, K. K., Radiative effects of natural aerosols: A review. *Atmos Environ* **2005,** *39* (11), 2089-2110.
(6) Ackerman, A. S.; Toon, O. B.; Stevens, D. E.; Heymsfield, A. J.; Ramanathan, V.; Welton, E. J., Reduction of tropical cloudiness by soot. *Science* **2000,** *288* (5468), 1042-1047.
(7) Koren, I.; Martins, J. V.; Remer, L. A.; Afargan, H., Smoke invigoration versus inhibition of clouds over the Amazon. *Science* **2008,** *321* (5891), 946-949.
(8) Hansen, J.; Nazarenko, L., Soot climate forcing via snow and ice albedos. *Proc Natl Acad Sci U S A* **2004,** *101* (2), 423-8.
(9) Jacobson, M. Z., Climate response of fossil fuel and biofuel soot, accounting for soot's feedback to snow and sea ice albedo and emissivity. *J Geophys Res-Atmos* **2004,** *109* (D21).
(10) Flanner, M. G.; Zender, C. S.; Randerson, J. T.; Rasch, P. J., Present-day climate forcing and response from black carbon in snow. *J Geophys Res-Atmos* **2007,** *112* (D11).
(11) *IPCC, 2013: Summary for Policymakers*; Contribution of Working Group I to the Fifth Assessment Report of the Intergovernmental Panel on Climate Change: Cambridge, United Kingdom and New York, NY, USA, 2013.
(12) Hansen, A. D. A.; Rosen, H.; Novakov, T., The Aethalometer - an Instrument for the Real-Time Measurement of Optical-Absorption by Aerosol-Particles. *Sci Total Environ* **1984,** *36* (Jun), 191-196.
(13) Bond, T. C.; Anderson, T. L.; Campbell, D., Calibration and intercomparison of filter-based measurements of visible light absorption by aerosols. *Aerosol Sci Tech* **1999,** *30* (6), 582-600.
(14) Petzold, A., Schloesser, H., Sheridan, P.J., Arnott, W.P., Ogren, J.A., Virkkula, A., Evaluation of multiangle absorption photometry for measuring aerosol light absorption. *Aerosol Sci. Technol.* **2005,** *39*, 40-51.
(15) Kondo, Y., Sahu, L., Kuwata, M., Miyazaki, Y., Takegawa, N., Moteki, N., et al., Stabilization of the Mass Absorption Cross Section of Black Carbon for Filter-Based Absorption Photometry by the Use of a Heated Inlet. *Aerosol Sci. Technol. 43* (8), 741–756.
(16) Moosmuller, H.; Chakrabarty, R. K.; Arnott, W. P., Aerosol light absorption and its measurement: A review. *J Quant Spectrosc Ra* **2009,** *110* (11), 844-878.

(17) Weingartner, E.; Saathoff, H.; Schnaiter, M.; Streit, N.; Bitnar, B.; Baltensperger, U., Absorption of light by soot particles: determination of the absorption coefficient by means of aethalometers. *J Aerosol Sci* **2003,** *34* (10), 1445-1463.
(18) Schmid, O., Artaxo, P., Arnott, W. P., Chand, D., Gatti, D., Frank, G. P., Hoffer, A., Schnaiter, M., and Andreae, M. O. , Spectral Light Absorption by Ambient Aerosols Influenced by Biomass Burning in the Amazon Basin-1. Comparison and Field Calibration of Absorption Measurement Techniques. *Atmos. Chem. Physics Discuss.* **2005,** *5*, 9355–9404.
(19) Magi, B. I., Hobbs, P. V., Schmid, B., and Redemann, J., Vertical Profiles of Light Scattering, Light Absorption, and Single Scattering Albedo During the Dry Biomass Burning Season in Southern Africa and Comparisons of In Situ Remote Sensing Measurements of Aerosol Optical Depths. *J. Geophys. Res.* **2003** *108*, 40-41.
(20) Smith, J. D.; Atkinson, D. B., A portable pulsed cavity ring-down transmissometer for measurement of the optical extinction of the atmospheric aerosol. *Analyst* **2001,** *126* (8), 1216-1220.
(21) Strawa, A. W.; Castaneda, R.; Owano, T.; Baer, D. S.; Paldus, B. A., The measurement of aerosol optical properties using continuous wave cavity ring-down techniques. *J Atmos Ocean Tech* **2003,** *20* (4), 454-465.
(22) Arnott, W. P.; Moosmuller, H.; Rogers, C. F.; Jin, T. F.; Bruch, R., Photoacoustic spectrometer for measuring light absorption by aerosol: instrument description. *Atmos Environ* **1999,** *33* (17), 2845-2852.
(23) Arnott, W. P.; Moosmuller, H.; Sheridan, P. J.; Ogren, J. A.; Raspet, R.; Slaton, W. V.; Hand, J. L.; Kreidenweis, S. M.; Collett, J. L., Photoacoustic and filter-based ambient aerosol light absorption measurements: Instrument comparisons and the role of relative humidity. *J Geophys Res-Atmos* **2003,** *108* (D1).
(24) Schnaiter, M.; Schmid, O.; Petzold, A.; Fritzsche, L.; Klein, K. F.; Andreae, M. O.; Helas, G.; Thielmann, A.; Gimmler, M.; Mohler, O.; Linke, C.; Schurath, U., Measurement of wavelength-resolved light absorption by aerosols utilizing a UV-VIS extinction cell. *Aerosol Sci Tech* **2005,** *39* (3), 249-260.
(25) Sheridan, P. J.; Arnott, W. P.; Ogren, J. A.; Andrews, E.; Atkinson, D. B.; Covert, D. S.; Moosmuller, H.; Petzold, A.; Schmid, B.; Strawa, A. W.; Varma, R.; Virkkula, A., The Reno Aerosol Optics Study: An evaluation of aerosol absorption measurement methods. *Aerosol Sci Tech* **2005,** *39* (1), 1-16.
(26) Bohren, C. F. a. H., D. R., *Absorption and scattering of light by small particles*. Wiley, New York: 1983.
(27) Lack, D. A.; Cappa, C. D., Impact of brown and clear carbon on light absorption enhancement, single scatter albedo and absorption wavelength dependence of black carbon. *Atmos Chem Phys* **2010,** *10* (9), 4207-4220.
(28) Cappa, C. D.; Onasch, T. B.; Massoli, P.; Worsnop, D. R.; Bates, T. S.; Cross, E. S.; Davidovits, P.; Hakala, J.; Hayden, K. L.; Jobson, B. T.; Kolesar, K. R.; Lack, D. A.; Lerner, B. M.; Li, S. M.; Mellon, D.; Nuaaman, I.; Olfert, J. S.; Petaja, T.; Quinn, P. K.; Song, C.; Subramanian, R.; Williams, E. J.; Zaveri, R. A., Radiative Absorption Enhancements Due to the Mixing State of Atmospheric Black Carbon. *Science* **2012,** *337* (6098), 1078-1081.

(29) Schwarz, J. P.; Spackman, J. R.; Fahey, D. W.; Gao, R. S.; Lohmann, U.; Stier, P.; Watts, L. A.; Thomson, D. S.; Lack, D. A.; Pfister, L.; Mahoney, M. J.; Baumgardner, D.; Wilson, J. C.; Reeves, J. M., Coatings and their enhancement of black carbon light absorption in the tropical atmosphere. *J Geophys Res-Atmos* **2008,** *113* (D3).
(30) Kai, L.; Massoli, P., Scattering of Electromagnetic-Plane Waves by Radially Inhomogeneous Spheres - a Finely Stratified Sphere Model. *Appl Optics* **1994,** *33* (3), 501-511.
(31) Martin, R. J., Mie Scattering Formulae for Non-spherical Particles. *Journal of Modern Optics* **1993,** *40*, 2467-2494.
(32) Martin, R. J., Scattering Matrices for Slightly Non-spherical Particles. *Journal of Modern Optics* **1995,** *42*, 157-169.
(33) Geng, Y. L.; Wu, X. B.; Li, L. W.; Guan, B. R., Mie scattering by a uniaxial anisotropic sphere. *Phys Rev E* **2004,** *70* (5).
(34) Qiu, C. W.; Luk'yanchuk, B., Peculiarities in light scattering by spherical particles with radial anisotropy. *J Opt Soc Am A* **2008,** *25* (7), 1623-1628.
(35) Asano, S.; Yamamoto, G., Light-Scattering by a Spheroidal Particle. *Appl Optics* **1975,** *14* (1), 29-49.
(36) Kerker, M.; Matijevic, E., Scattering of Electromagnetic Waves from Concentric Infinite Cylinders. *J Opt Soc Am* **1961,** *51* (5), 506-&.
(37) Wriedt, T., A review of elastic light scattering theories. *Part Part Syst Char* **1998,** *15* (2), 67-74.
(38) Waterman, P. C., Matrix formulation of electromagnetic scattering. *Proc IEEE* **1965,** *53*, 805-812.
(39) Fuller, K. A.; Malm, W. C.; Kreidenweis, S. M., Effects of mixing on extinction by carbonaceous particles. *J Geophys Res-Atmos* **1999,** *104* (D13), 15941-15954.
(40) S. Levine, G. O. O., Scattering of electromagnetic waves by two equal spherical particles. *J. Colloid Interface Sci.* **1968,** *27* (3), 442.
(41) J. Bruning, Y. L., Multiple scattering of EM waves by spheres. I. Multiple expansions and ray optics solutions. *IEEE Trans. Antennas Propag* **1971,** *19* (3), 378.
(42) J. Bruning, Y. L., Multiple scattering of EM waves by spheres, part II—numerical and experimental results. *IEEE Trans. Antennas Propag* **1971,** *19* (3), 391.
(43) Mackowski, D. W., Calculation of Total Cross-Sections of Multiple-Sphere Clusters. *J Opt Soc Am A* **1994,** *11* (11), 2851-2861.
(44) Mackowski, D. W.; Mishchenko, M. I., Calculation of the T matrix and the scattering matrix for ensembles of spheres. *J Opt Soc Am A* **1996,** *13* (11), 2266-2278.
(45) Liu, L., and Mishchenko, M. I., Effects of Aggregation on Scatter- ing and Radiative Properties of Soot Aerosols. *J. Geophys. Res.-Atmos.* **2005,** *110*, D11211.
(46) Liu, L.; Mishchenko, M. I., Scattering and radiative properties of complex soot and soot-containing aggregate particles. *J Quant Spectrosc Ra* **2007,** *106* (1-3), 262-273.
(47) Liu, L.; Mishchenko, M. I.; Arnott, W. P., A study of radiative properties of fractal soot aggregates using the superposition T-matrix method. *J Quant Spectrosc Ra* **2008,** *109* (15), 2656-2663.
(48) Flagan, R. C., Differential Mobility Analysis of Aerosols: A Tutorial. *Kona Powder Part J* **2008,** *26*, 254-268.

(49) Knutson, E. O. W., K. T., Aerosol Classification by Electric Mobility: Apparatus, Theory, and Application. *Aerosol Science* **1975,** *6*, 9.
(50) Cunningham, E., On the velocity of steady fall of spherical particles through fluid medium. *P R Soc Lond a-Conta* **1910,** *83* (563), 357-365.
(51) Allen, M. D.; Raabe, O. G., Slip Correction Measurements of Spherical Solid Aerosol-Particles in an Improved Millikan Apparatus. *Aerosol Sci Tech* **1985,** *4* (3), 269-286.
(52) Stolzenburg, M. R. An Ultrafine Aerosol Size Distibution Measuring System. University of Minnesota, Twin Cities, Minneapolis, 1988.
(53) Rosencwaig, A., *Photoacoustics and photoacoustic spectroscopy*. Wiley: NewYork,NY, 1980.
(54) Tam, A. C., Applications of Photoacoustic Sensing Techniques. *Rev Mod Phys* **1986,** *58* (2), 381-431.
(55) Patel, C. K. N.; Lambert, C. A.; Burkhard.Eg, Spectroscopic Measurements of Stratospheric Nitric-Oxide and Water-Vapor. *Science* **1974,** *184* (4142), 1173-1176.
(56) Arnott, W. P.; Walker, J. W.; Moosmuller, H.; Elleman, R. A.; Jonsson, H. H.; Buzorius, G.; Conant, W. C.; Flagan, R. C.; Seinfeld, J. H., Photoacoustic insight for aerosol light absorption aloft from meteorological aircraft and comparison with particle soot absorption photometer measurements: DOE Southern Great Plains climate research facility and the coastal stratocumulus imposed perturbation experiments. *J Geophys Res-Atmos* **2006,** *111* (D5).
(57) R. W. Terhune, J. E. A., Spectrophone measurements of the absorption of visible light by aerosols in the atmosphere. *Optial Letter* **1977,** *1*, 70-72.
(58) Radney, J. G., Zangmeister, C. D., Measurement of Gas and Aerosol Phase Absorption Spectra across the Visible and Near-IR Using Supercontinuum Photoacoustic Spectroscopy. *Analytical chemistry* **2015,** *87*, 7356.
(59) Petzold, A.; Niessner, R., Novel Design of a Resonant Photoacoustic Spectrophone for Elemental Carbon Mass Monitoring. *Appl Phys Lett* **1995,** *66* (10), 1285-1287.
(60) Bijnen, F. G. C.; Reuss, J.; Harren, F. J. M., Geometrical optimization of a longitudinal resonant photoacoustic cell for sensitive and fast trace gas detection. *Review of Scientific Instruments* **1996,** *67* (8), 2914-2923.
(61) Bernegger, S.; Sigrist, M. W., Co-Laser Photoacoustic-Spectroscopy of Gases and Vapors for Trace Gas-Analysis. *Infrared Phys* **1990,** *30* (5), 375-429.
(62) Gillis, K. A.; Havey, D. K.; Hodges, J. T., Standard photoacoustic spectrometer: Model and validation using O-2 A-band spectra. *Review of Scientific Instruments* **2010,** *81* (6).
(63) Havey, D. K.; Bueno, P. A.; Gillis, K. A.; Hodges, J. T.; Mulholland, G. W.; van Zee, R. D.; Zachariah, M. R., Photoacoustic Spectrometer with a Calculable Cell Constant for Measurements of Gases and Aerosols. *Analytical Chemistry* **2010,** *82* (19), 7935-7942.
(64) Ehara, K., Hagwood, C., and Coakley, K. J. , Novel Method to Classify Aerosol Particles Accoding to Their Mass-to-Charge Ratio– Aerosol Particle Mass Analyzer. *J. Aerosol Sci. 27*, 217-234.

(65) Park, K.; Cao, F.; Kittelson, D. B.; McMurry, P. H., Relationship between particle mass and mobility for diesel exhaust particles. *Environ Sci Technol* **2003,** *37* (3), 577-583.
(66) Lall, A. A.; Ma, X. F.; Guha, S.; Mulholland, G. W.; Zachariah, M. R., Online Nanoparticle Mass Measurement by Combined Aerosol Particle Mass Analyzer and Differential Mobility Analyzer: Comparison of Theory and Measurements. *Aerosol Sci Tech* **2009,** *43* (11), 1075-1083.
(67) Park, K.; Kittelson, D. B.; Zachariah, M. R.; McMurry, P. H., Measurement of inherent material density of nanoparticle agglomerates. *J Nanopart Res* **2004,** *6* (2-3), 267-272.
(68) Geller, M.; Biswas, S.; Sioutas, C., Determination of particle effective density in urban environments with a differential mobility analyzer and aerosol particle mass analyzer. *Aerosol Sci Tech* **2006,** *40* (9), 709-723.
(69) McMurry, P. H.; Wang, X.; Park, K.; Ehara, K., The relationship between mass and mobility for atmospheric particles: A new technique for measuring particle density. *Aerosol Sci Tech* **2002,** *36* (2), 227-238.
(70) Kim, S. C., Wang, J., Emery, M. S., Shin, W. G., Mulholland, G. W., and Pui, D. Y. H., Structural Property Effect of Nanoparticle Agglomerates on Particle Penetration through Fibrous Filter. *Aerosol Sci. Technol 43*, 344-355.
(71) Guha, S.; Ma, X.; Tarlov, M. J.; Zachariah, M. R., Quantifying Ligand Adsorption to Nanoparticles Using Tandem Differential Mobility Mass Analysis. *Analytical Chemistry* **2012,** *84* (15), 6308-6311.
(72) Ma, X. F.; Zachariah, M. R., Oxidation Anisotropy and Size-Dependent Reaction Kinetics of Zinc Nanocrystals. *J Phys Chem C* **2009,** *113* (33), 14644-14650.
(73) Lall, A. A., Rong, W., Madler, L., and Friedlander, S. K., Nanoparticle Aggregate Volume Determination by Electrical Mobility Analysis: Test of Idealized Aggregate Theory Using Aerosol Particle Mass Analyzer Measurements. *J. Aerosol Sci.* **2008,** *39*, 403–417.
(74) Lee, S. Y.; Chang, H.; Ogi, T.; Iskandar, F.; Okuyama, K., Measuring the effective density, porosity, and refractive index of carbonaceous particles by tandem aerosol techniques. *Carbon* **2011,** *49* (7), 2163-2172.
(75) Pui, B. Y. H. L. a. D. Y. H., A Submicron Aerosol Standard and the Primary, Absolute Calibration of the Condensation Nuclei Counter. *J Colloid Interf Sci* **1974,** *47*, 155-171.
(76) Pollak, P. J. N. a. L. W., The calibration of a photo-electric nucleus counter. *Proceedings of the Royal Irish Academy. Section A: Mathematical and Physical Sciences* **1945,** *51*, 9-31.
(77) Skala, G., A New Instrument for the Continuous Measurement of Condensation Nuclei. *Analytical Chemistry* **1963,** *35*, 702-706.
(78) Stolzenburg, M. R.; Mcmurry, P. H., An Ultrafine Aerosol Condensation Nucleus Counter. *Aerosol Sci Tech* **1991,** *14* (1), 48-65.
(79) Hering, S. V.; Stolzenburg, M. R.; Quant, F. R.; Oberreit, D. R.; Keady, P. B., A laminar-flow, water-based condensation particle counter (WCPC). *Aerosol Sci Tech* **2005,** *39* (7), 659-672.

(80) Iida, K.; Stolzenburg, M. R.; McMurry, P. H.; Smith, J. N.; Quant, F. R.; Oberreit, D. R.; Keady, P. B.; Eiguren-Fernandez, A.; Lewis, G. S.; Kreisberg, N. M.; Hering, S. V., An ultrafine, water-based condensation particle counter and its evaluation under field conditions. *Aerosol Sci Tech* **2008,** *42* (10), 862-871.
(81) Guha, S.; Li, M.; Tarlov, M. J.; Zachariah, M. R., Electrospray-differential mobility analysis of bionanoparticles. *Trends Biotechnol* **2012,** *30* (5), 291-300.
(82) Stefaniak, A. B.; Hackley, V. A.; Roebben, G.; Ehara, K.; Hankin, S.; Postek, M. T.; Lynch, I.; Fu, W. E.; Linsinger, T. P. J.; Thunemann, A. F., Nanoscale reference materials for environmental, health and safety measurements: needs, gaps and opportunities. *Nanotoxicology* **2013,** *7* (8), 1325-1337.
(83) Guha, S.; Li, M. D.; Tarlov, M. J.; Zechariah, M. R., Electrospray-differential mobility analysis of bionanoparticles. *Trends Biotechnol* **2012,** *30* (5), 291-300.
(84) Linsinger, T. P. J.; Roebben, G.; Solans, C.; Ramsch, R., Reference materials for measuring the size of nanoparticles. *Trac-Trend Anal Chem* **2011,** *30* (1), 18-27.
(85) Maisser, A.; Premnath, V.; Ghosh, A.; Nguyen, T. A.; Attoui, M.; Hogan, C. J., Determination of gas phase protein ion densities via ion mobility analysis with charge reduction. *Phys Chem Chem Phys* **2011,** *13* (48), 21630-21641.
(86) Ude, S.; de la Mora, J. F., Molecular monodisperse mobility and mass standards from electrosprays of tetra-alkyl ammonium halides. *J Aerosol Sci* **2005,** *36* (10), 1224-1237.
(87) Kaufman, S. L.; Skogen, J. W.; Dorman, F. D.; Zarrin, F.; Lewis, K. C., Macromolecule analysis based on electrophoretic mobility in air: Globular proteins (vol 68, pg 1895, 1996). *Analytical Chemistry* **1996,** *68* (20), 3703-3703.
(88) Bacher, G.; Szymanski, W. W.; Kaufman, S. L.; Zollner, P.; Blaas, D.; Allmaier, G., Charge-reduced nano electrospray ionization combined with differential mobility analysis of peptides, proteins, glycoproteins, noncovalent protein complexes and viruses. *J Mass Spectrom* **2001,** *36* (9), 1038-1052.
(89) Ku, B. K.; de la Mora, J. F.; Saucy, D. A.; Alexander, J. N., Mass distribution measurement of water-insoluble polymers by charge-reduced electrospray mobility analysis. *Analytical Chemistry* **2004,** *76* (3), 814-822.
(90) Eninger, R. M.; Hogan, C. J.; Biswas, P.; Adhikari, A.; Reponen, T.; Grinshpun, S. A., Electrospray versus Nebulization for Aerosolization and Filter Testing with Bacteriophage Particles. *Aerosol Sci Tech* **2009,** *43* (4), 298-304.
(91) Pease, L. F.; Tsai, D. H.; Brorson, K. A.; Guha, S.; Zachariah, M. R.; Tarlov, M. J., Physical Characterization of Icosahedral Virus Ultra Structure, Stability, and Integrity Using Electrospray Differential Mobility Analysis. *Analytical Chemistry* **2011,** *83* (5), 1753-1759.
(92) Laschober, C.; Kaddis, C. S.; Reischl, G. P.; Loo, J. A.; Allmaier, G.; Szymanski, W. W., Comparison of various nano-differential mobility analysers (nDMAs) applying globular proteins. *J Exp Nanosci* **2007,** *2* (4), 291-301.
(93) Tsai, D. H.; Zangmeister, R. A.; Pease, L. F.; Tarlov, M. J.; Zachariah, M. R., Gas-phase ion-mobility characterization of SAM-functionalized Au nanoparticles. *Langmuir* **2008,** *24* (16), 8483-8490.
(94) Hinterwirth, H.; Wiedmer, S. K.; Moilanen, M.; Lehner, A.; Allmaier, G.; Waitz, T.; Lindner, W.; Lammerhofer, M., Comparative method evaluation for size

and size-distribution analysis of gold nanoparticles. *J Sep Sci* **2013,** *36* (17), 2952-2961.
(95) Guha, S.; Pease, L. F.; Brorson, K. A.; Tarlov, M. J.; Zachariah, M. R., Evaluation of electrospray differential mobility analysis for virus particle analysis: Potential applications for biomanufacturing. *J Virol Methods* **2011,** *178* (1-2), 201-208.
(96) Allmaier, G.; Laschober, C.; Szymanski, W. W., Nano ES GEMMA and PDMA, new tools for the analysis of nanobioparticles - Protein complexes, lipoparticles, and viruses. *J Am Soc Mass Spectr* **2008,** *19* (8), 1062-1068.
(97) E.O. Knutson, K. T. W., Aerosol classification by electric mobility: apparatus, theory, and applications. *J Aerosol Sci* **1975,** *6* (6), 443-451.
(98) Hagwood, C.; Sivathanu, Y.; Mulholland, G., The DMA transfer function with Brownian motion a trajectory/Monte-Carlo approach. *Aerosol Sci Tech* **1999,** *30* (1), 40-61.
(99) Attoui, M.; Paragano, M.; Cuevas, J.; de la Mora, J. F., Tandem DMA Generation of Strictly Monomobile 1-3.5 nm Particle Standards. *Aerosol Sci Tech* **2013,** *47* (5), 499-511.
(100) Hogan, C. J.; Ruotolo, B. T.; Robinson, C. V.; de la Mora, J. F., Tandem Differential Mobility Analysis-Mass Spectrometry Reveals Partial Gas-Phase Collapse of the GroEL Complex. *J Phys Chem B* **2011,** *115* (13), 3614-3621.
(101) Hogan, C. J.; Kettleson, E. M.; Ramaswami, B.; Chen, D. R.; Biswas, P., Charge reduced electrospray size spectrometry of mega- and gigaDalton complexes: Whole viruses and virus fragments. *Abstr Pap Am Chem S* **2006,** *231*.
(102) Banerjee, S.; Mazumdar, S., Electrospray Ionization Mass Spectrometry: A Technique to Access the Information beyond the Molecular Weight of the Analyte. *Int J Anal Chem* **2012**.
(103) Harshbar.Wr; Robin, M. B., Opto-Acoustic Effect - Revival of an Old Technique for Molecular Spectroscopy. *Accounts Chem Res* **1973,** *6* (10), 329-334.
(104) Fiegel, R. P.; Hays, P. B.; Wright, W. M., Photoacoustic Technique for the Measurement of Absorption-Line Profiles. *Appl Optics* **1989,** *28* (7), 1401-1408.
(105) Roessler, D. M., Photoacoustic Insights on Diesel Exhaust Particles. *Appl Optics* **1984,** *23* (8), 1148-1155.
(106) K.M. Adams, L. I. D. J., S.M. Japar, W.R. Pierson, Real-time, in situ measurements of atmospheric optical absorption in the visible via photoacoustic spectroscopy—II. Validation for atmospheric elemental carbon aerosol. *Atmos Environ* **1967,** *23*, 693-700.
(107) Arnott, W. P.; Moosmuller, H.; Walker, J. W., Nitrogen dioxide and kerosene-flame soot calibration of photoacoustic instruments for measurement of light absorption by aerosols. *Review of Scientific Instruments* **2000,** *71* (12), 4545-4552.
(108) Lack, D. A.; Lovejoy, E. R.; Baynard, T.; Pettersson, A.; Ravishankara, A. R., Aerosol absorption measurement using photoacoustic spectroscopy: Sensitivity, calibration, and uncertainty developments. *Aerosol Sci Tech* **2006,** *40* (9), 697-708.
(109) Faraday, M., The Bakerian lecture: experimental relations of gold (and other metals) to light. *Philosophical Transactions of the Royal Society London* **1857,** *147*, 145-181.

(110) Palik, E. D., *Handbook of Optical Constants of Solids*. Academic Press: Burlington, 1997.
(111) McPeak, K. M.; Jayanti, S. V.; Kress, S. J. P.; Meyer, S.; Iotti, S.; Rossinelli, A.; Norris, D. J., Plasmonic Films Can Easily Be Better: Rules and Recipes. *Acs Photonics* **2015,** *2* (3), 326-333.
(112) Zhou, L.; You, R.; Tan, J. J.; Zachariah, M. R., Wavelength-Resolved UV Photoelectric Charging Dynamics of Nanoparticles: Comparison of Spheres and Aggregates. *Aerosol Sci Tech* **2013,** *47* (6), 672-680.
(113) Kim, J. H.; Babushok, V. I.; Germer, T. A.; Mulholland, G. W.; Ehrman, S. H., Cosolvent-assisted spray pyrolysis for the generation of metal particles. *J Mater Res* **2003,** *18* (7), 1614-1622.
(114) Joutsensaari, J.; Ahonen, P.; Tapper, U.; Kauppinen, E. I.; Laurila, J.; Kuokkala, V. T., Generation of nanophase fullerene particles via aerosol routes. *Synthetic Met* **1996,** *77* (1-3), 85-88.
(115) Joutsensaari, J.; Kauppinen, E. I.; Bernaerts, D.; Van Tendeloo, G., Crystal growth studies during aerosol synthesis of nanostructured fullerene particles. *Nanostructured Powders and Their Industrial Applications* **1998,** *520*, 63-68.
(116) Joutsensaari, J.; Ahonen, P. P.; Kauppinen, E. I.; Brown, D. P.; Lehtinen, K. E. J.; Jokiniemi, J. K.; Powels, B.; Van Tendeloo, G., Aerosol synthesis of fullerene nanocrystals in controlled flow reactor conditions. *J Nanopart Res* **2000,** *2* (1), 53-74.
(117) Gurav, A. S.; Kodas, T. T.; Wang, L. M., Gas-Phase Particle-Size Distributions during Vapor Condensation of Fullerenes. *Nanostruct Mater* **1994,** *4* (5), 491-496.
(118) NIST Technical Disclaimer: Certain commercial equipment, i., or materials (or suppliers, or software, ...) are identified in this paper to foster understanding. Such identification does not imply recommendation or endorsement by the National Institute of Standards and Technology, nor does it imply that the materials or equipment identified are necessarily the best available for the purpose.
(119) James G. Radney, C. D. Z., Practical limitations of aerosol separation by a tandem differential mobility analyzer-aerosol particle mass analyzer. *Aerosol Sci Tech* **2016,** *50*, 160-172.
(120) Bueno, P. A.; Havey, D. K.; Mulholland, G. W.; Hodges, J. T.; Gillis, K. A.; Dickerson, R. R.; Zachariah, M. R., Photoacoustic Measurements of Amplification of the Absorption Cross Section for Coated Soot Aerosols. *Aerosol Sci Tech* **2011,** *45* (10), 1217-1230.
(121) Kratschmer, W.; Lamb, L. D.; Fostiropoulos, K.; Huffman, D. R., Solid C-60 - a New Form of Carbon. *Nature* **1990,** *347* (6291), 354-358.
(122) Scheckman, J. H.; McMurry, P. H.; Pratsinis, S. E., Rapid Characterization of Agglomerate Aerosols by In Situ Mass-Mobility Measurements. *Langmuir* **2009,** *25* (14), 8248-8254.
(123) *CRC Handbook of Chemistry and Physics, 96th Edition* CRC Press: 2015.
(124) Dresselhaus M.S., G. D. P. C. E., *Science of Fullerenes and Carbon Nanotubes*. Academic Press: San Diego, 1996.
(125) Dresselhaus, M. S.; Dresselhaus, G.; Rao, A. M.; Eklund, P. C., Optical properties of C-60 and related materials. *Synthetic Met* **1996,** *78* (3), 313-325.

(126) Gasyna, Z.; Schatz, P. N.; Hare, J. P.; Dennis, T. J.; Kroto, H. W.; Taylor, R.; Walton, D. R. M., The Magnetic Circular-Dichroism and Absorption-Spectra of C60 Isolated in Ar Matrices. *Chem Phys Lett* **1991,** *183* (3-4), 283-291.
(127) Chan, G. H.; Zhao, J.; Hicks, E. M.; Schatz, G. C.; Van Duyne, R. P., Plasmonic properties of copper nanoparticles fabricated by nanosphere lithography. *Nano Lett* **2007,** *7* (7), 1947-1952.
(128) Willets, K. A.; Van Duyne, R. P., Localized surface plasmon resonance spectroscopy and sensing. *Annu Rev Phys Chem* **2007,** *58*, 267-297.
(129) Rakic, A. D., Algorithm for the Determination of Intrinsic Optical-Constants of Metal-Films - Application to Aluminum. *Appl Optics* **1995,** *34* (22), 4755-4767.
(130) Martinsson, E.; Otte, M. A.; Shahjamali, M. M.; Sepulveda, B.; Aili, D., Substrate Effect on the Refractive Index Sensitivity of Silver Nanoparticles. *J Phys Chem C* **2014,** *118* (42), 24680-24687.
(131) Lu, X. M.; Rycenga, M.; Skrabalak, S. E.; Wiley, B.; Xia, Y. N., Chemical Synthesis of Novel Plasmonic Nanoparticles. *Annu Rev Phys Chem* **2009,** *60*, 167-192.
(132) Buseck, P. R.; Adachi, K.; Andras, G.; Tompa, E.; Mihaly, P., Ns-Soot: A Material-Based Term for Strongly Light-Absorbing Carbonaceous Particles. *Aerosol Sci Tech* **2014,** *48* (7), 777-788.
(133) Bond, T. C.; Doherty, S. J.; Fahey, D. W.; Forster, P. M.; Berntsen, T.; DeAngelo, B. J.; Flanner, M. G.; Ghan, S.; Karcher, B.; Koch, D.; Kinne, S.; Kondo, Y.; Quinn, P. K.; Sarofim, M. C.; Schultz, M. G.; Schulz, M.; Venkataraman, C.; Zhang, H.; Zhang, S.; Bellouin, N.; Guttikunda, S. K.; Hopke, P. K.; Jacobson, M. Z.; Kaiser, J. W.; Klimont, Z.; Lohmann, U.; Schwarz, J. P.; Shindell, D.; Storelvmo, T.; Warren, S. G.; Zender, C. S., Bounding the role of black carbon in the climate system: A scientific assessment. *J. Geophys. Res.: Atmos.* **2013,** *118* (11), 5380-5552.
(134) Baynard, T.; Lovejoy, E. R.; Pettersson, A.; Brown, S. S.; Lack, D.; Osthoff, H.; Massoli, P.; Ciciora, S.; Dube, W. P.; Ravishankara, A. R., Design and Application of a Pulsed Cavity Ring-Down Aerosol Extinction Spectrometer for Field Measurements. *Aerosol Sci. Technol.* **2007,** *41* (4), 447-462.
(135) Olfert, J. S.; Symonds, J. P. R.; Collings, N., The effective density and fractal dimension of particles emitted from a light-duty diesel vehicle with a diesel oxidation catalyst. *J Aerosol Sci* **2007,** *38* (1), 69-82.
(136) Steiner, D. H. B. a. H. G., Structure and disposition of particles from a spark ignition engine. *Atmos Environ* **1992,** *26*, 997-1003.
(137) Reid, J. S., P. V. Hobbs, R. J. Ferek, D. R. Blake, J. V. Martins, M. R. Dunlap, and C. Liousse, Physical, chemical, and optical properties of reginal hazes dominated by smoke in Brazil. *Journal of Geophysical Research* **1998,** *103*, 32059-32080.
(138) Fang, M., M. Zheng, F. Wang, K. L. To, A. B. Jaafar, and S. L. Tong, The solvent-extractable organic compounds in the Indoesia biomass burning aerosols -- characterzation studies. *Atmos Environ* **1999,** *33*, 783-795.
(139) China, S.; Mazzoleni, C.; Gorkowski, K.; Aiken, A. C.; Dubey, M. K., Morphology and mixing state of individual freshly emitted wildfire carbonaceous particles. *Nat. Commun.* **2013,** *4*.

(140) Khalizov, A. F.; Xue, H.; Wang, L.; Zheng, J.; Zhang, R., Enhanced Light Absorption and Scattering by Carbon Soot Aerosol Internally Mixed with Sulfuric Acid. *J. Phys. Chem. A* **2009,** *113* (6), 1066-1074.
(141) Li, J.; Anderson, J. R.; Buseck, P. R., TEM study of aerosol particles from clean and polluted marine boundary layers over the North Atlantic. *J. Geophys. Res.: Atmos.* **2003,** *108* (D6).
(142) Shiraiwa, M.; Kondo, Y.; Moteki, N.; Takegawa, N.; Miyazaki, Y.; Blake, D. R., Evolution of mixing state of black carbon in polluted air from Tokyo. *Geophys Res Lett* **2007,** *34* (16).
(143) Moffet, R. C.; Prather, K. A., In-situ measurements of the mixing state and optical properties of soot with implications for radiative forcing estimates. *P Natl Acad Sci USA* **2009,** *106* (29), 11872-11877.
(144) Adachi, K.; Buseck, P. R., Internally mixed soot, sulfates, and organic matter in aerosol particles from Mexico City. *Atmos Chem Phys* **2008,** *8* (21), 6469-6481.
(145) Bond, T. C.; Habib, G.; Bergstrom, R. W., Limitations in the enhancement of visible light absorption due to mixing state. *J. Geophys. Res.: Atmos.* **2006,** *111* (D20).
(146) Jacobson, M. Z., Strong radiative heating due to the mixing state of black carbon in atmospheric aerosols. *Nature* **2001,** *409* (6821), 695-697.
(147) Zhang, R. Y.; Khalizov, A. F.; Pagels, J.; Zhang, D.; Xue, H. X.; McMurry, P. H., Variability in morphology, hygroscopicity, and optical properties of soot aerosols during atmospheric processing. *P Natl Acad Sci USA* **2008,** *105* (30), 10291-10296.
(148) Yablonovitch, E., Statistical ray optics. *J. Opt. Soc. Am.* **1982,** *72* (7), 899-907.
(149) Bond, T. C.; Bergstrom, R. W., Light absorption by carbonaceous particles: An investigative review. *Aerosol Sci Tech* **2006,** *40* (1), 27-67.
(150) Lack, D. A.; Cappa, C. D.; Cross, E. S.; Massoli, P.; Ahern, A. T.; Davidovits, P.; Onasch, T. B., Absorption Enhancement of Coated Absorbing Aerosols: Validation of the Photo-Acoustic Technique for Measuring the Enhancement. *Aerosol Sci. Technol.* **2009,** *43* (10), 1006-1012.
(151) Schwarz, J. P.; Spackman, J. R.; Fahey, D. W.; Gao, R. S.; Lohmann, U.; Stier, P.; Watts, L. A.; Thomson, D. S.; Lack, D. A.; Pfister, L.; Mahoney, M. J.; Baumgardner, D.; Wilson, J. C.; Reeves, J. M., Coatings and their enhancement of black carbon light absorption in the tropical atmosphere. *J. Geophys. Res.: Atmos.* **2008,** *113* (D3).
(152) Lan, Z. J.; Huang, X. F.; Yu, K. Y.; Sun, T. L.; Zeng, L. W.; Hu, M., Light absorption of black carbon aerosol and its enhancement by mixing state in an urban atmosphere in South China. *Atmos Environ* **2013,** *69*, 118-123.
(153) Nakayama, T.; Ikeda, Y.; Sawada, Y.; Setoguchi, Y.; Ogawa, S.; Kawana, K.; Mochida, M.; Ikemori, F.; Matsumoto, K.; Matsumi, Y., Properties of light-absorbing aerosols in the Nagoya urban area, Japan, in August 2011 and January 2012: Contributions of brown carbon and lensing effect. *J. Geophys. Res.: Atmos.* **2014,** *119* (22), 12721-12739.
(154) Liu, S.; Aiken, A. C.; Gorkowski, K.; Dubey, M. K.; Cappa, C. D.; Williams, L. R.; Herndon, S. C.; Massoli, P.; Fortner, E. C.; Chhabra, P. S.; Brooks, W. A.; Onasch, T. B.; Jayne, J. T.; Worsnop, D. R.; China, S.; Sharma, N.; Mazzoleni, C.; Xu, L.; Ng, N. L.; Liu, D.; Allan, J. D.; Lee, J. D.; Fleming, Z. L.; Mohr, C.; Zotter,

P.; Szidat, S.; Prevot, A. S. H., Enhanced light absorption by mixed source black and brown carbon particles in UK winter. *Nat. Commun.* **2015,** *6*.
(155) Peng, J.; Hu, M.; Guo, S.; Du, Z.; Zheng, J.; Shang, D.; Levy Zamora, M.; Zeng, L.; Shao, M.; Wu, Y.-S.; Zheng, J.; Wang, Y.; Glen, C. R.; Collins, D. R.; Molina, M. J.; Zhang, R., Markedly enhanced absorption and direct radiative forcing of black carbon under polluted urban environments. *Proc. Natl. Acad. Sci. U.S.A.* **2016,** *113* (16), 4266-4271.
(156) Fuller, K. A.; Malm, W. C.; Kreidenweis, S. M., Effects of mixing on extinction by carbonaceous particles. *J. Geophys. Res.: Atmos.* **1999,** *104* (D13), 15941-15954.
(157) Adachi, K.; Chung, S. H.; Buseck, P. R., Shapes of soot aerosol particles and implications for their effects on climate. *J. Geophys. Res.: Atmos.* **2010,** *115*.
(158) Mackowski, D. W., A simplified model to predict the effects of aggregation on the absorption properties of soot particles. *J. Quant. Spectrosc. Radiat. Transfer* **2006,** *100* (1-3), 237-249.
(159) Scarnato, B. V.; Vahidinia, S.; Richard, D. T.; Kirchstetter, T. W., Effects of internal mixing and aggregate morphology on optical properties of black carbon using a discrete dipole approximation model. *Atmos Chem Phys* **2013,** *13* (10), 5089-5101.
(160) Schnaiter, M.; Linke, C.; Mohler, O.; Naumann, K. H.; Saathoff, H.; Wagner, R.; Schurath, U.; Wehner, B., Absorption amplification of black carbon internally mixed with secondary organic aerosol. *J. Geophys. Res.: Atmos.* **2005,** *110* (D19).
(161) Shiraiwa, M.; Kondo, Y.; Iwamoto, T.; Kita, K., Amplification of Light Absorption of Black Carbon by Organic Coating. *Aerosol Sci Tech* **2010,** *44* (1), 46-54.
(162) Cross, E. S.; Onasch, T. B.; Ahern, A.; Wrobel, W.; Slowik, J. G.; Olfert, J.; Lack, D. A.; Massoli, P.; Cappa, C. D.; Schwarz, J. P.; Spackman, J. R.; Fahey, D. W.; Sedlacek, A.; Trimborn, A.; Jayne, J. T.; Freedman, A.; Williams, L. R.; Ng, N. L.; Mazzoleni, C.; Dubey, M.; Brem, B.; Kok, G.; Subramanian, R.; Freitag, S.; Clarke, A.; Thornhill, D.; Marr, L. C.; Kolb, C. E.; Worsnop, D. R.; Davidovits, P., Soot Particle Studies—Instrument Inter-Comparison—Project Overview. *Aerosol Sci. Technol.* **2010,** *44* (8), 592-611.
(163) Schnaiter, M.; Horvath, H.; Mohler, O.; Naumann, K. H.; Saathoff, H.; Schock, O. W., UV-VIS-NIR spectral optical properties of soot and soot-containing aerosols. *J Aerosol Sci* **2003,** *34* (10), 1421-1444.
(164) Thompson, J. E.; Hayes, P. L.; Jimenez, J. L.; Adachi, K.; Zhang, X. L.; Liu, J. M.; Weber, R. J.; Buseck, P. R., Aerosol optical properties at Pasadena, CA during CalNex 2010. *Atmos Environ* **2012,** *55*, 190-200.
(165) Jacobson, M. Z., Comment on "Radiative Absorption Enhancements Due to the Mixing State of Atmospheric Black Carbon". *Science* **2013,** *339* (6118).
(166) Moosmüller, H.; Chakrabarty, R. K.; Arnott, W. P., Aerosol light absorption and its measurement: A review. *J. Quant. Spectrosc. Radiat. Transfer* **2009,** *110* (11), 844-878.
(167) Russell, P. B.; Bergstrom, R. W.; Shinozuka, Y.; Clarke, A. D.; DeCarlo, P. F.; Jimenez, J. L.; Livingston, J. M.; Redemann, J.; Dubovik, O.; Strawa, A., Absorption Angstrom Exponent in AERONET and related data as an indicator of aerosol composition. *Atmos Chem Phys* **2010,** *10* (3), 1155-1169.

(168) Bahadur, R.; Praveen, P. S.; Xu, Y. Y.; Ramanathan, V., Solar absorption by elemental and brown carbon determined from spectral observations. *P Natl Acad Sci USA* **2012,** *109* (43), 17366-17371.
(169) Kirchstetter, T. W.; Novakov, T.; Hobbs, P. V., Evidence that the spectral dependence of light absorption by aerosols is affected by organic carbon. *J. Geophys. Res.: Atmos.* **2004,** *109* (D21).
(170) Yang, M.; Howell, S. G.; Zhuang, J.; Huebert, B. J., Attribution of aerosol light absorption to black carbon, brown carbon, and dust in China - interpretations of atmospheric measurements during EAST-AIRE. *Atmos Chem Phys* **2009,** *9* (6), 2035-2050.
(171) Bergstrom, R. W.; Pilewskie, P.; Russell, P. B.; Redemann, J.; Bond, T. C.; Quinn, P. K.; Sierau, B., Spectral absorption properties of atmospheric aerosols. *Atmos Chem Phys* **2007,** *7* (23), 5937-5943.
(172) Sandradewi, J.; Prevot, A. S. H.; Szidat, S.; Perron, N.; Alfarra, M. R.; Lanz, V. A.; Weingartner, E.; Baltensperger, U., Using aerosol light absorption measurements for the quantitative determination of wood burning and traffic emission contributions to particulate matter. *Environ. Sci. Technol.* **2008,** *42* (9), 3316-3323.
(173) Levin, E. J. T.; McMeeking, G. R.; Carrico, C. M.; Mack, L. E.; Kreidenweis, S. M.; Wold, C. E.; Moosmuller, H.; Arnott, W. P.; Hao, W. M.; Collett, J. L.; Malm, W. C., Biomass burning smoke aerosol properties measured during Fire Laboratory at Missoula Experiments (FLAME). *J. Geophys. Res.: Atmos.* **2010,** *115*.
(174) Clarke, A.; McNaughton, C.; Kapustin, V.; Shinozuka, Y.; Howell, S.; Dibb, J.; Zhou, J.; Anderson, B.; Brekhovskikh, V.; Turner, H.; Pinkerton, M., Biomass burning and pollution aerosol over North America: Organic components and their influence on spectral optical properties and humidification response. *J. Geophys. Res.: Atmos.* **2007,** *112* (D12).
(175) Haisch, C.; Menzenbach, P.; Bladt, H.; Niessner, R., A Wide Spectral Range Photoacoustic Aerosol Absorption Spectrometer. *Anal. Chem.* **2012,** *84* (21), 8941-8945.
(176) Wiegand, J. R.; Mathews, L. D.; Smith, G. D., A UV–Vis Photoacoustic Spectrophotometer. *Anal. Chem.* **2014,** *86* (12), 6049 - 6056.
(177) Sharma, N.; Arnold, I. J.; Moosmüller, H.; Arnott, W. P.; Mazzoleni, C., Photoacoustic and nephelometric spectroscopy of aerosol optical properties with a supercontinuum light source. *Atmos. Meas. Tech.* **2013,** *6* (12), 3501-3513.
(178) Moosmüller, H.; Chakrabarty, R. K.; Ehlers, K. M.; Arnott, W. P., Absorption Ångström coefficient, brown carbon, and aerosols: basic concepts, bulk matter, and spherical particles. *Atmos. Chem. Phys.* **2011,** *11* (3), 1217-1225.
(179) Moosmüller, H.; Engelbrecht, J. P.; Skiba, M.; Frey, G.; Chakrabarty, R. K.; Arnott, W. P., Single scattering albedo of fine mineral dust aerosols controlled by iron concentration. *J. Geophys. Res.: Atmos.* **2012,** *117* (D11), D11210.
(180) Lewis, K.; Arnott, W. P.; Moosmüller, H.; Wold, C. E., Strong spectral variation of biomass smoke light absorption and single scattering albedo observed with a novel dual-wavelength photoacoustic instrument. *J. Geophys. Res.: Atmos.* **2008,** *113* (D16), D16203.
(181) Gyawali, M.; Arnott, W. P.; Lewis, K.; Moosmüller, H., In situ aerosol optics in Reno, NV, USA during and after the summer 2008 California wildfires and the

influence of absorbing and non-absorbing organic coatings on spectral light absorption. *Atmos. Chem. Phys.* **2009,** *9* (20), 8007-8015.
(182) Radney, J. G.; Zangmeister, C. D., Practical limitations of aerosol separation by a tandem differential mobility analyzer–aerosol particle mass analyzer. *Aerosol Sci. Technol.* **2016,** *50* (2), 160-172.
(183) Hunt, G. R., Infrared spectral behavior of fine particulate solids. *J. Phys. Chem.* **1976,** *80* (11), 1195-1198.
(184) Khalizov, A. F.; Lin, Y.; Qiu, C.; Guo, S.; Collins, D.; Zhang, R., Role of OH-Initiated Oxidation of Isoprene in Aging of Combustion Soot. *Environ. Sci. Technol.* **2013,** *47* (5), 2254-2263.
(185) China, S.; Scarnato, B.; Owen, R. C.; Zhang, B.; Ampadu, M. T.; Kumar, S.; Dzepina, K.; Dziobak, M. P.; Fialho, P.; Perlinger, J. A.; Hueber, J.; Helmig, D.; Mazzoleni, L. R.; Mazzoleni, C., Morphology and mixing state of aged soot particles at a remote marine free troposphere site: Implications for optical properties. *Geophys. Res. Lett.* **2015,** *42* (4), 1243-1250.
(186) Kozlov, V. S.; Panchenko, M. V.; Tikhomirov, A. B.; Tikhomirov, B. A.; Shmargunov, V. P., Effect of relative air humidity on photoacoustic aerosol absorption measurements in the near-ground atmospheric layer. *Atmos. Oceanic Opt.* **2011,** *24* (5), 487-491.
(187) Langridge, J. M.; Richardson, M. S.; Lack, D. A.; Brock, C. A.; Murphy, D. M., Limitations of the Photoacoustic Technique for Aerosol Absorption Measurement at High Relative Humidity. *Aerosol Sci. Technol.* **2013,** *47* (11), 1163-1173.
(188) Lewis, K. A.; Arnott, W. P.; Moosmuller, H.; Chakrabarty, R. K.; Carrico, C. M.; Kreidenweis, S. M.; Day, D. E.; Malm, W. C.; Laskin, A.; Jimenez, J. L.; Ulbrich, I. M.; Huffman, J. A.; Onasch, T. B.; Trimborn, A.; Liu, L.; Mishchenko, M. I., Reduction in biomass burning aerosol light absorption upon humidification: roles of inorganically-induced hygroscopicity, particle collapse, and photoacoustic heat and mass transfer. *Atmos Chem Phys* **2009,** *9* (22), 8949-8966.
(189) Murphy, D. M., The Effect of Water Evaporation on Photoacoustic Signals in Transition and Molecular Flow. *Aerosol Sci. Technol.* **2009,** *43* (4), 356-363.
(190) Mackowski, D. W., *MSTM: A Multiple Sphere T-Matrix FORTRAN Code for Use on Parallel Computer Clusters, version 3.0*. National Aeronautics and Space Administration: New York: Goddard Institute for Space Studies, 2013.
(191) Witten, T. A.; Sander, L. M., Diffusion-Limited Aggregation, a Kinetic Critical Phenomenon. *Phys Rev Lett* **1981,** *47* (19), 1400-1403.
(192) Radney, J. G.; You, R.; Ma, X.; Conny, J. M.; Zachariah, M. R.; Hodges, J. T.; Zangmeister, C. D., Dependence of soot optical properties on particle morphology: measurements and model comparisons. *Environ. Sci. Technol.* **2014,** *48* (6), 3169-76.
(193) Clarke, A. D.; Shinozuka, Y.; Kapustin, V. N.; Howell, S.; Huebert, B.; Doherty, S.; Anderson, T.; Covert, D.; Anderson, J.; Hua, X.; Moore, K. G.; McNaughton, C.; Carmichael, G.; Weber, R., Size distributions and mixtures of dust and black carbon aerosol in Asian outflow: Physiochemistry and optical properties. *J. Geophys. Res.: Atmos.* **2004,** *109* (D15).
(194) Janzen, J., The Refractive Index of Carbon Black. *J. Colloid Interface Sci.* **1979,** *69*, 436-447.

(195) Chang, H., and Charalampopoulos, T. T., Determination of the Wave-length Dependence of Refractive Indices of Flame Soot. *Proc. R. Soc. Lond. A* **1990,** *430*, 577-591.
(196) Marley, N. A., Gaffney, J. S., Baird, J. C., Blazer, C. A., Drayton, P. J., and Frederick, J. E., An Empirical Method for the Determination of the Complex Refractive Index of Size-Fractionated Atmospheric Aerosols for Radiative Transfer Calculations. *Aerosol Sci. Technol.* **2001,** *34*, 535-549.
(197) Knox, A.; Evans, G. J.; Brook, J. R.; Yao, X.; Jeong, C. H.; Godri, K. J.; Sabaliauskas, K.; Slowik, J. G., Mass Absorption Cross-Section of Ambient Black Carbon Aerosol in Relation to Chemical Age. *Aerosol Sci Tech* **2009,** *43* (6), 522-532.
(198) Feng, Y.; Ramanathan, V.; Kotamarthi, V. R., Brown carbon: a significant atmospheric absorber of solar radiation? *Atmos Chem Phys* **2013,** *13* (17), 8607-8621.
(199) Forster, P., Ramaswamy, V., Artaxo, P., Berntsen, T., Betts, R., Fahey, D. W., Haywood, J., Lean, J., Lowe, D. C., Myhre, G., Nganga, J., Prinn, R., Raga, G., Schulz, M., and Van Dorland, R. *Changes in Atmospheric Constituents and in Radiative Forcing, in: Climate Change 2007: The Physical Science Basis.*; New York, NY, 2007; pp 129–234.
(200) Hobbs, P. V.; Reid, J. S.; Kotchenruther, R. A.; Ferek, R. J.; Weiss, R., Direct radiative forcing by smoke from biomass burning. *Science* **1997,** *275* (5307), 1776-1778.
(201) Jacobson, M. Z., Effects of biomass burning on climate, accounting for heat and moisture fluxes, black and brown carbon, and cloud absorption effects. *J Geophys Res-Atmos* **2014,** *119* (14), 8980-9002.
(202) Chakrabarty, R. K.; Moosmuller, H.; Chen, L. W. A.; Lewis, K.; Arnott, W. P.; Mazzoleni, C.; Dubey, M. K.; Wold, C. E.; Hao, W. M.; Kreidenweis, S. M., Brown carbon in tar balls from smoldering biomass combustion. *Atmos Chem Phys* **2010,** *10* (13), 6363-6370.
(203) Hoffer, A.; Gelencser, A.; Guyon, P.; Kiss, G.; Schmid, O.; Frank, G. P.; Artaxo, P.; Andreae, M. O., Optical properties of humic-like substances (HULIS) in biomass-burning aerosols. *Atmos Chem Phys* **2006,** *6*, 3563-3570.
(204) O'Neill, N. T.; Eck, T. F.; Holben, B. N.; Smirnov, A.; Royer, A.; Li, Z., Optical properties of boreal forest fire smoke derived from Sun photometry. *J Geophys Res-Atmos* **2002,** *107* (D11).
(205) Lee, S.; Baumann, K.; Schauer, J. J.; Sheesley, R. J.; Naeher, L. P.; Meinardi, S.; Blake, D. R.; Edgerton, E. S.; Russell, A. G.; Clements, M., Gaseous and particulate emissions from prescribed burning in Georgia. *Environ Sci Technol* **2005,** *39* (23), 9049-9056.
(206) Amara L. Holder, G. S. W. H., Johanna Aurell, Michael D. Hays, and Brian K. Gullett, Particulate matter and black carbon optical properties and emission factors from prescribed fires in the southeastern United States. *Journal of Geophysical Research: Atmospheres* **2016,** *121*, 3465-3483.
(207) Chand, D.; Schmid, O.; Gwaze, P.; Parmar, R. S.; Helas, G.; Zeromskiene, K.; Wiedensohler, A.; Massling, A.; Andreae, M. O., Laboratory measurements of smoke optical properties from the burning of Indonesian peat and other types of biomass. *Geophys Res Lett* **2005,** *32* (12).

(208) Chen, L.-W. A., Moosmuller, H., Arnott,W. P., Chow, J. C.,Watson, J. G., Susott, R. A., Babbitt, R. E., Wold, C. E., Lincoln, E. N., and Hao, W. M., Particle emissions from laboratory combustion of wildland fuels: In situ optical and mass meausurements. *Geophys. Res. Lett.* **2006,** *33*, L04803.
(209) Roden, C. A.; Bond, T. C.; Conway, S.; Benjamin, A.; Pinel, O., Emission factors and real-time optical properties of particles emitted from traditional wood burning cookstoves. *Environ Sci Technol* **2006,** *40* (21), 6750-6757.
(210) Liu, S.; Aiken, A. C.; Arata, C.; Dubey, M. K.; Stockwell, C. E.; Yokelson, R. J.; Stone, E. A.; Jayarathne, T.; Robinson, A. L.; DeMott, P. J.; Kreidenweis, S. M., Aerosol single scattering albedo dependence on biomass combustion efficiency: Laboratory and field studies. *Geophys Res Lett* **2014,** *41* (2), 742-748.
(211) McMeeking, G. R.; Kreidenweis, S. M.; Baker, S.; Carrico, C. M.; Chow, J. C.; Collett, J. L.; Hao, W. M.; Holden, A. S.; Kirchstetter, T. W.; Malm, W. C.; Moosmuller, H.; Sullivan, A. P.; Wold, C. E., Emissions of trace gases and aerosols during the open combustion of biomass in the laboratory. *J Geophys Res-Atmos* **2009,** *114*.
(212) Chen, Y.; Bond, T. C., Light absorption by organic carbon from wood combustion. *Atmos Chem Phys* **2010,** *10* (4), 1773-1787.
(213) May, A. A.; McMeeking, G. R.; Lee, T.; Taylor, J. W.; Craven, J. S.; Burling, I.; Sullivan, A. P.; Akagi, S.; Collett, J. L.; Flynn, M.; Coe, H.; Urbanski, S. P.; Seinfeld, J. H.; Yokelson, R. J.; Kreidenweis, S. M., Aerosol emissions from prescribed fires in the United States: A synthesis of laboratory and aircraft measurements. *J Geophys Res-Atmos* **2014,** *119* (20), 11826-11849.
(214) Kondo, Y.; Sahu, L.; Kuwata, M.; Miyazaki, Y.; Takegawa, N.; Moteki, N.; Imaru, J.; Han, S.; Nakayama, T.; Oanh, N. T. K.; Hu, M.; Kim, Y. J.; Kita, K., Stabilization of the Mass Absorption Cross Section of Black Carbon for Filter-Based Absorption Photometry by the use of a Heated Inlet. *Aerosol Sci Tech* **2009,** *43* (8), 741-756.
(215) Yuan Cheng, G. E., Hans Moosmüller, W. Patrick Arnott, L.-W. Antony Chen, Cyle E. Wold, Wei Min Hao, Ke-bin He, Light absorption by biomass burning source emissions. *Atmos Environ* **2016,** *127*, 347-354.
(216) Hille, M. G.; Stephens, S. L., Mixed conifer forest duff consumption during prescribed fires: Tree crown impacts. *Forest Sci* **2005,** *51* (5), 417-424.
(217) Zangmeister, J. G. R. C. D., Practical limitations of aerosol separation by a tandem differential mobility analyzer–aerosol particle mass analyzer. *Aerosol Sci. Technol* **2016,** *50*, 160-172.
(218) R You, J. R., MR Zachariah, CD Zangmeister, Measured Wavelength-Dependent Absorption Enhancement of Internally Mixed Black Carbon with Absorbing and Non-absorbing Materials. *Environ Sci Tech Let* **2016**.
(219) Reid, J. S.; Koppmann, R.; Eck, T. F.; Eleuterio, D. P., A review of biomass burning emissions part II: intensive physical properties of biomass burning particles. *Atmos Chem Phys* **2005,** *5*, 799-825.
(220) Subramanian, R.; Roden, C. A.; Boparai, P.; Bond, T. C., Yellow beads and missing particles: Trouble ahead for filter-based absorption measurements. *Aerosol Sci Tech* **2007,** *41* (6), 630-637.

(221) Nakayama, T.; Ikeda, Y.; Sawada, Y.; Setoguchi, Y.; Ogawa, S.; Kawana, K.; Mochida, M.; Ikemori, F.; Matsumoto, K.; Matsumi, Y., Properties of light-absorbing aerosols in the Nagoya urban area, Japan, in August 2011 and January 2012: Contributions of brown carbon and lensing effect. *J Geophys Res-Atmos* **2014,** *119* (22), 12721-12739.
(222) Draine, B. T.; Flatau, P. J., Discrete-Dipole Approximation for Scattering Calculations. *J Opt Soc Am A* **1994,** *11* (4), 1491-1499.
(223) Hodges, J. T.; Layer, H. P.; Miller, W. W.; Scace, G. E., Frequency-stabilized single-mode cavity ring-down apparatus for high-resolution absorption spectroscopy. *Rev. Sci. Instrum.* **2004,** *75* (4), 849-863.
(224) Radney, J. G.; Ma, X.; Gillis, K. A.; Zachariah, M. R.; Hodges, J. T.; Zangmeister, C. D., Direct measurements of mass-specific optical cross sections of single component aerosol mixtures. *Anal. Chem.* **2013,** *85* (17), 8319-8325.
(225) Deb, K., *Multi-objective optimization using evolutionary algorithms*. 1st ed. ed.; John Wiley & Sons: Chichester, 2001.
(226) Zarzana, K. J.; Cappa, C. D.; Tolbert, M. A., Sensitivity of Aerosol Refractive Index Retrievals Using Optical Spectroscopy. *Aerosol Sci. Technol.* **2014,** *48* (11), 1133-1144.
(227) Bohren, C. F.; Huffman, D. R., *Absorption and scattering of light by small particles*. Wiley: New York, 1983.
(228) Zangmeister, C. D.; Radney, J. G.; Dockery, L. T.; Young, J. T.; Ma, X. F.; You, R. A.; Zachariah, M. R., Packing density of rigid aggregates is independent of scale. *P Natl Acad Sci USA* **2014,** *111* (25), 9037-9041.
(229) Park, K.; Cao, F.; Kittelson, D. B.; McMurry, P. H., Relationship between Particle Mass and Mobility for Diesel Exhaust Particles. *Environ. Sci. Technol.* **2003,** *37* (3), 577-583.
(230) Scheckman, J. H.; McMurry, P. H.; Pratsinis, S. E., Rapid Characterization of Agglomerate Aerosols by In Situ Mass−Mobility Measurements. *Langmuir* **2009,** *25* (14), 8248-8254.
(231) Sorensen, C. M., The Mobility of Fractal Aggregates: A Review. *Aerosol Sci Tech* **2011,** *45* (7), 765-779.
(232) Eggersdorfer, M. L.; Kadau, D.; Herrmann, H. J.; Pratsinis, S. E., Aggregate morphology evolution by sintering: Number and diameter of primary particles. *J. Aerosol Sci.* **2012,** *46* (0), 7-19.
(233) Brasil, A. M.; Farias, T. L.; Carvalho, M. G., A recipe for image characterization of fractal-like aggregates. *J Aerosol Sci* **1999,** *30* (10), 1379-1389.
(234) Park, K.; Kittelson, D. B.; McMurry, P. H., Structural properties of diesel exhaust particles measured by transmission electron microscopy (TEM): Relationships to particle mass and mobility. *Aerosol Sci. Technol.* **2004,** *38* (9), 881-889.
(235) Chakrabarty, R. K.; Garro, M. A.; Garro, B. A.; Chancellor, S.; Moosmuller, H.; Herald, C. M., Simulation of Aggregates with Point-Contacting Monomers in the Cluster-Dilute Regime. Part 2: Comparison of Two- and Three-Dimensional Structural Properties as a Function of Fractal Dimension. *Aerosol Sci. Technol.* **2011,** *45* (8), 903-908.

(236) Toon, O. B.; Pollack, J. B.; Khare, B. N., The Optical Constants of Several Atmospheric Aerosol Species: Ammonium Sulfate, Aluminum Oxide, and Sodium Chloride. *J. Geophys. Res.* **1976,** *81* (33), 5733-5748.
(237) Li, H. H., Refractive index of alkali halides and its wavelength and temperature derivatives. *J. Phys. Chem. Ref. Data* **1976,** *5*, 329.